

ABSTRACT

Experimental Probe-induced Complex RF Plasma Phenomena

Brandon Joseph Harris, Ph.D.

Mentor: Truell W. Hyde II, Ph.D.

Plasma has long been studied in its own right as a state of matter, but the addition of particles large compared to its basic constituents yields a host of complicated behavior that was not predicted theoretically. Levitated micrometer-sized particles in the sheath of a RF plasma have previously been shown to form basic symmetry structure, but in this study, formerly undiscovered vertical oscillations, horizontal circular cavities, and waves in chains (longitudinal and transverse) were produced. Though a cylindrical vertical powered probe is used here to arrange and drive the particles in the laboratory, perturbations also exist in plasma formations in space that contain macroparticles. Probe theory is well established as a method to extract plasma parameters, but here the interaction of the probe affects particles directly through the probe's electric field when nearby, and indirectly affects the particles by changing the local plasma conditions when far away. These effects are first examined independently, and then merged with a mid-range exploration by observing the particle structure formations and their motion. Since the probe extends into the non-uniform plasma sheath, the ubiquitous bulk plasma

calculations are not valid, though they can be used as a starting point to facilitate understanding of the plasma and explain its interactions with dust and the probe.

Experimental Probe-induced Complex RF Plasma Phenomena

by

Brandon Joseph Harris, B.S.

A Dissertation

Approved by the Department of Physics

Gregory A. Benesh, Ph.D., Chairperson

Submitted to the Graduate Faculty of
Baylor University in Partial Fulfillment of the
Requirements for the Degree
of
Doctor of Philosophy

Approved by the Dissertation Committee

Truell W. Hyde, Ph.D., Chairperson

Lorin S. Matthews, Ph.D.

Kenneth T. Park, Ph.D.

Jon Harrison, Ph.D.

Gregory A. Benesh, Ph.D.

Accepted by the Graduate School
August 2014

J. Larry Lyon, Ph.D., Dean

Copyright © 2014 by Brandon Joseph Harris

All rights reserved

TABLE OF CONTENTS

LIST OF FIGURES	vii
ACKNOWLEDGMENTS	xii
DEDICATION	xiii
CHAPTER ONE	1
Introduction.....	1
1.1 Plasma as a State of Matter.....	1
1.2 Industrial Plasma Processing	2
1.3 Complex Plasma	3
CHAPTER TWO	12
Equipment.....	12
2.1 GEC Cell.....	12
2.2 Zyvex S100 Nanomanipulator	15
2.3 Other Equipment.....	16
CHAPTER THREE	18
Complex Plasma Fundamentals.....	18
3.1 Basic Plasma.....	18
3.2 Complex Plasma Basics.....	31
3.3 Challenges.....	41
CHAPTER FOUR.....	44
Experiment.....	44
4.1 Introduction.....	44
4.2 Vertical Oscillation.....	44
4.3 Dust Cavities.....	59
4.4 Dust Chain Waves	67
CHAPTER FIVE	72
Results.....	72
5.1 Introduction.....	72
5.2 Vertical Oscillation.....	73
5.3 Dust Cavities.....	90
5.4 Dust Chain Waves	121
CHAPTER SIX.....	131
Conclusions.....	131

APPENDICES	134
APPENDIX A.....	135
Extended Data.....	135
APPENDIX B.....	145
Core Programming Code	145
BIBLIOGRAPHY.....	149

LIST OF FIGURES

Figure 1 – Example circuit board with electronic components, which have greatly decreased in size over the last generation.	4
Figure 2 – The components of Saturn’s rings have been found to exhibit macroscopic features based on the physics behind complex plasma.	6
Figure 3 – A schematic of ITER cut through the center, which is designed to be the largest tokomak in the world.	7
Figure 4 – A plasma inside of a Q-machine, with a Langmuir probe inserted.	8
Figure 5 – Typical single layer complex plasma dust crystal formed at 10 W system power and 650 mTorr neutral gas pressure with 8.9 micrometer diameter Melamine Formaldehyde particles.	9
Figure 6 – A schematic of the GEC cell used in this experiment.	12
Figure 7 – CASPER plasma cell 2, ignited with background Argon gas, illumination provided by HeNe lasers, data acquired by cameras, dust dropped by shakers, and high vacuum pressure measured by an ion gauge.	14
Figure 8 - The Zyvex S100 Nanomanipulator head is located inside the plasma cell, mounted upside down above the upper ring electrode.	15
Figure 9 – Glass box placed on the lower electrode to facilitate greater horizontal and vertical confinement.	17
Figure 10 - Electron temperature and emission intensity as a function of height, with added horizontal lines.	27
Figure 11 – Required distance for ions to accelerate to the Bohm velocity in the presheath as a function of the electron energy.	31
Figure 12 – Cartoon of dust grain charging mechanism, where the larger spheres are Argon ions (generally attracted at this stage), the smaller are electrons (generally repelled), and the background atoms are omitted.	33
Figure 13 – Mach number predicted at the dust position as a function of the pressure, using OML to find the charge and Lieberman cross-section to find the ion mean free path.	42

Figure 14 – Side view of the vertical oscillation experiment.	46
Figure 15 – Normalized optical emission intensity profile of the plasma (Figure 14) averaged over the horizontal coordinate as a function of the distance above the lower electrode (where the upper electrode is located at $z=19$ mm).	48
Figure 16 – Distance from the lower electrode versus time for: the particle height, the sheath edge, the maximum of the derivative of the emission intensity, and the maximum of the emission intensity, for the following conditions: a) 0.75 W system power, b) base configuration (1.00 W), c) 1.50 W, d) 70 mTorr, e) 90 mTorr, f) 45 V probe peak to peak (VPP), g) 65 VPP, h) 10 V probe bias, i) 30 V probe bias, j) 1 Hz oscillation k) 5 Hz oscillation, l) 9 mm probe height, m) 11 mm probe height, n) -1 V DC bias, and o) -10 V DC bias.	49
Figure 17 – Particle oscillation amplitude versus probe oscillation frequency.	52
Figure 18 – A fit to the standard phase difference of the damped, forced harmonic oscillator (Eqn. 4.2) yields parameters that do not match the experimentally measured phase difference.	54
Figure 19 – Expanded view of the base configuration (Fig. 5b).	54
Figure 20 – Intensity space-time contour plot for the base configuration and for the probe at 65 V_{pp}	57
Figure 21 - Maximum intensity percentage change over time for the base configuration and the 65 V_{pp} case, superimposed with tracked particle data and probe potential, which is scaled to the maximum particle position.	57
Figure 22 – Oscillation amplitudes for the sheath edge and the particle with quadratic or linear fits shown for variation in the individual parameters given in Table I.	58
Figure 23 – Natural dust voids occur in the plasma bulk when a majority of the gravitational force pushing the dust into the sheath is absent.	60
Figure 24 – Plots from ISS voids showing a linear ion density increase and void size asymptote with RF voltage increase.	60
Figure 25 – Data collected on the ISS showing dust density as a function of distance from the center of the void.	61
Figure 26 – Cavities induced by negative probe potentials ranging from 0 to -55 V with respect to ground (the potential of the upper electrode and walls).	62
Figure 27 – Inner negative probe potential induced cavity radii over all parameters tested, at pressures of 50 mTorr, 100 mTorr, and 300 mTorr.	62

Figure 28 – Plot of natural cavity radius versus pressure for 10 W system power.	63
Figure 29 – Natural cavity radius versus system power for various fixed pressures.	64
Figure 30 – Cavity radius as a function of probe bias with respect to system ground at 10 W system power and 100 mTorr chamber pressure.....	65
Figure 31 – Radial waves generated by oscillating the potential on a probe (spot at cavity center) held at a positive bias.	66
Figure 32 – Under conditions sensitive to small changes, a radial resonance effect can be generated.....	67
Figure 33 – The experimental setup required to produce longitudinal waves in a dust chain, where the image has been rotated so that the vertical upwards direction is to the left.	69
Figure 34 – Longitudinal dust chain waves with the central particle out of phase (antisymmetric mode), the central particle stationary (standing wave mode), and all particles moving together (symmetric mode).	70
Figure 35 – Position of the probe utilized to generate transverse waves through dust particle chains.	71
Figure 36 – The electric potential from Eqn. 5.2 and electric field from Eqn. 5.3 from the lower electrode ($z = 0$) to the sheath edge for the base configuration.	76
Figure 37 – Mach number of the ions and ion density as a function of the distance from the lower electrode.	77
Figure 38 – Forces involved in the levitation of the dust within the plasma sheath for $E_0 = -2,800$ V/m (solid) and $E_0 = 0$ V/m (dashed).....	78
Figure 39 – Ion drag and plasma densities as a function of position from the lower electrode.....	80
Figure 40 – Changes as a result of modifying the value of $ E_0 $, at the experimentally determined dust positions for the base configuration.	81
Figure 41 – As the sheath edge ion Mach number is increased, the change to the ion Mach number at the dust height and the ion drag at the dust are shown.	82
Figure 42 - Predictions of multiple perturbations to the simple electric field model for the base configuration with $E_0 = -2,800$ V/m.	85

Figure 43 - Particle levitation height and location of the sheath edge as a function of time for probe potential oscillation frequency of a) 5 Hz and b) base configuration.	88
Figure 44 - Method to find the sheath edge electric field value.	89
Figure 45 - Cavity radii over the probe bias with respect to ground with linear fits.	93
Figure 46 – Average dust force on the inner ring.	94
Figure 47 – A detailed plot of the cavity radii, electron density and screening length at various probe potentials.	96
Figure 48 – Quantities which affect the size of cavities produced by the negative probe potential.	98
Figure 49 – Boundary electric field value (E_0) as a function of the probe potential.	99
Figure 50 – Ion and electron plasma density as well as the ion drag is shown in the vertical direction for 10 W plasma power and 100 mTorr system pressure (compare to Figure 39).	99
Figure 51 – Electric potential (relative to the plasma potential) and electric field as a distance from the probe as calculated from the negative derivative of the potential solved from Eqn. 5.11.	100
Figure 52 – The sheath electric fields found in the vertical oscillation experiment are superimposed with results from ambipolar diffusion.	102
Figure 53 – Ionization rate and number of particles flowing in the sheath as a function of distance from the lower electrode.	104
Figure 54 – Simulation result with added lines perpendicular to the first contour line denoting the direction of the ion flow.	107
Figure 55 – Characteristic heights as a function of pressures at which natural cavities form, including the equilibrium levitation height of the dust, the sheath width defined by Sheridan et al. (1991), the sheath edge found from the equilibrium levitation height of 0.46 micrometer diameter particles, and the average areal density of the dust.	108
Figure 56 – Plasma intensity profiles for 200 mTorr and 700 mTorr with vertical lines showing the cutout edge and the cutout center.	109
Figure 57 – The average areal dust density as a function of the radial position, where radial distance of dust particles is binned and the interparticle distance averaged.	112

Figure 58 – Ion mean free path as a function of neutral gas pressure, and the potential energy of the average particle in a dust crystal having a naturally formed cavity for various pressures.	113
Figure 59 – Initial ion speed as a function of positive probe potential normalized to the equilibrium ion thermal speed at the dust levitation height.	115
Figure 60 - Potential energy plot for positive-probe-potential induced cavities.	116
Figure 61 – Space-time diagram of the radial distance of dust particles from the probe during potential oscillation.	117
Figure 62 – Radial dust grain motion in a single layer crystal driven by a central probe with oscillating potential.	118
Figure 63 – Radial dust position versus time for the annular dust wave discussed in Figure 62 and for radial resonance.	119
Figure 64 – Dispersion relations found experimentally (points) and theoretically (lines) for the antisymmetric (blue circles), symmetric (black triangles), and standing (red squares) longitudinal waves.	123
Figure 65 – Dispersion relation for the standing wave for various values of charge and screening length.	123
Figure 66 – Lower particle ion streaming forces (Δp is the change in momentum) through two mechanisms.	125
Figure 67 - A Transverse chain wave dispersion results, data points are from experiment while the fit line is from Eqn 5.19.	125
Figure 68 – Fourier transforms of the central particle’s position as a function of time in an oscillated chain for the antisymmetric mode, showing the relative size between the fundamental frequency and the first harmonic.	127
Figure 69 – Heights of individual dust grains above the lower electrode located in a vertical chain versus time (in seconds) that is being oscillated longitudinally by the varying potential of a probe, superimposed with the results of Eqn. 5.16, for the antisymmetric mode is shown, and the standing wave mode.	129

ACKNOWLEDGMENTS

A sincere appreciation must be recorded for both my research advisor, Dr. Truell W. Hyde, and Dr. Lorin S. Matthews. Their comments in meetings, reflections on work, and steadfast determination have been critical in the production of this dissertation. Their professionalism produces the highest possible honors for Baylor University. Like two laser beams radiating unabated through the vastness of space, piercing the unexplored, their minds project a pure strength that help power all with whom they interact.

Peers along my epic journey must also be illuminated. First, during my undergraduate degree at the University of Wisconsin - Madison: Quentin Schiller, Erin Conrad, and Erik Sczygelski, whose bright minds and collaboration greatly aided a process of unlocking the known laws of physics. Second, during my doctorate: Dr. Jared Greenwald, Dr. Angela Douglass, Dr. Zhaunzhao Zhang, Jay Murphree, and Dr. Tim Renner, with whom discussion brought order. Special notes must be made of James Creel, whose indefatigable spirit contributed to my trek to Baylor, and Dr. Victor Land, whose infectious curiosity led me to discover new vistas in France and the Netherlands.

Last but not least, thanks are in order for the agencies of funding: CASPER, GearUP, NASA Texas Space Grant Consortium, NSF, DOE, Victor & Mary D. Nelson Foundation, Burlington Northern Railroad, Wisconsin Academic Excellence Program, and Baylor University. I must also thank the UW–Madison Plasma Physics department for offering me a job as an undergraduate, out of which a true joy of programming blossomed. These organizations provided the means to pursue this work without economic struggle, allowing me to hone my mind to be the most potent tool I possess.

DEDICATION

To all great minds

Including my favorite authors:

L. Tolstoy, F. Dostoyevsky, A. Rand, D. Adams, I. Asimov, A. Huxley, G. Orwell, M. Proust, R. Bradbury, R. Jordan, G. Martin, N. Chomsky, H. Zinn, J. Foer, P. Maass

And those who provided unfaltering support:

- My parents -
John Duke Harris
Kathleen Renée Gondek

- My uncle -
David Michael Gondek

Finally, the first of my family to study calculus:

- My uncle -
William Emerson Harris

CHAPTER ONE

Introduction

1.1 Plasma as a State of Matter

What do stellar interiors (Potekhin 2013), ionospheres (Bosinger 2013), gaseous nebulae (Garcia 2013), interstellar media (Gurnett 2013), Van Allen radiation belts (Reeves 2013), solar wind (Osman 2013), lightning (Fülöp 2013), aurora (Forsyth 2013), fluorescent lighting (Jusoh 2013), rocket exhaust (Engblom 2013), magnetic confinement fusion (Chen 2006), and quark-gluon mixtures (Bonitz 2010) have in common? They all contain plasma, consisting of particle densities ranging over a staggering 36 orders of magnitude from 10^3 to 10^{39} cm^{-3} , with the temperature spanning 14 orders of magnitude from 10^{-2} to 10^{12} K. Considering this parameter space is far larger than for any other state of matter, plasma must be recognized as the most ubiquitous form of matter in the universe. Though the physics of plasma is typically assigned to the classical regime, quantum studies have continued to increase. For example, planetary and white dwarf interiors, as well as magnetars (neutron stars with magnetic fields) behave as quantum plasma (Shukla 2010).

As required in all mathematical proofs, axioms must also be set to define plasma. Qualitatively, these are the following. First, plasma must have a particle density large enough that collective effects, where a large number of plasma particles collaborate to create long-range phenomena, can occur. Second, the atoms or molecules must be ionized to such a degree that shielding of electric potentials (a reduction in the apparent strength of the added charge as one moves away from it) by particle rearrangement

occurs. Third, physical collisions must not occur so rapidly as to extinguish the shielding or reduce the particle motion to that of hydrodynamics (which accurately describes neutral gases). These conditions will be further elucidated in Section 3.1.

1.2 Industrial Plasma Processing

Despite the great prevalence of electronic devices in modern society, it may come as a surprise that over one-third of the tens to hundreds of steps required to make every microchip depends on a plasma physics process (Lieberman 2005). These processes include deposition, doping, growth, etching, and removal of material to/on/from surfaces. The primary mechanisms of etching, described in Section 3.1.2, are employed to isolate devices or insert capacitors. Etching can be achieved on silicon using plasma comprised of a gas of tetrafluorocarbon (CF_4). Being non-toxic, this process holds an advantage over wet corrosive chemicals applied for the same purpose. Etching has been used to produce 0.2 micrometer wide trenches, which is about 200 times smaller than the inner diameter of the proboscis (blood-sucking nozzle) of a female mosquito (Ramasubramanian 2008). Etch depths are dependent on the time interval over which the process is allowed to occur. There has been significant effort expended in learning to control the etching anisotropy – i.e., to what degree the depression is desired to go straight down versus removal from the sidewalls. Given that semiconductors constitute a 300 billion dollar per year industry (Semiconductor Industry Association 2012 <http://www.sia-online.org>), trade secrets are guaranteed to exist, so the true state of the art remains unpublished in the open literature.

Other plasma processes are available through the utilization of different gases. Argon and oxygen plasmas are used for sputter deposition of aluminum, tungsten, and high T_c

(the temperature where superconductors transition to superconduction) superconducting films. Growing glass (SiO_2) on silicon is possible using oxygen plasma, which helps prevent microloading (Michigan University 2007 <https://www.mems-exchange.org>), which is a problematic local depletion of the ions used for etching (Hedlund 1994). The well-known industrial process referred to as Plasma Enhanced Chemical Vapor Deposition (PECVD) is also used for creating glass films. One advantage of PECVD is the coating of Si_3N_4 over an aluminum film, whereas using basic Chemical Vapor Deposition (CVD) melts the aluminum (an undesired result) because CVD requires higher temperatures. Trifluoroboride (BF_3) is used to dope boron atoms into silicon. It is fascinating to note that the purity required for silicon before doping in general is one impurity in ten billion, which is roughly equivalent to one grain of salt in a boxcar of sugar (All About Circuits 2012 <http://www.allaboutcircuits.com/>). This is important to note because the vacuum environment of plasma machines can provide this level of impurity prevention.

The above processes also play important roles in the aerospace, automotive, steel, biomedical, and toxic waste industries. In addition, high power plasma cutters, developed out of plasma arc welding in the early 1980's, can produce temperatures of 25,000 Kelvin (Sacks 2005), and are routinely used to cut steel up to an incredible 15 cm in thickness.

1.3 Complex Plasma

An ongoing goal within the semiconductor industry is to reduce power consumption and increase speed of operation. As such, the semiconductor feature size (Figure 1) continues to decrease since shorter wires reduce resistance and decrease electron transit

time. A single atom transistor has now been created (Fuechsle 2012) and the current record for the number of transistors on a single computer's central processing unit (CPU), held by Intel's Xeon Phi, is five billion, with an individual length of 22 nm.

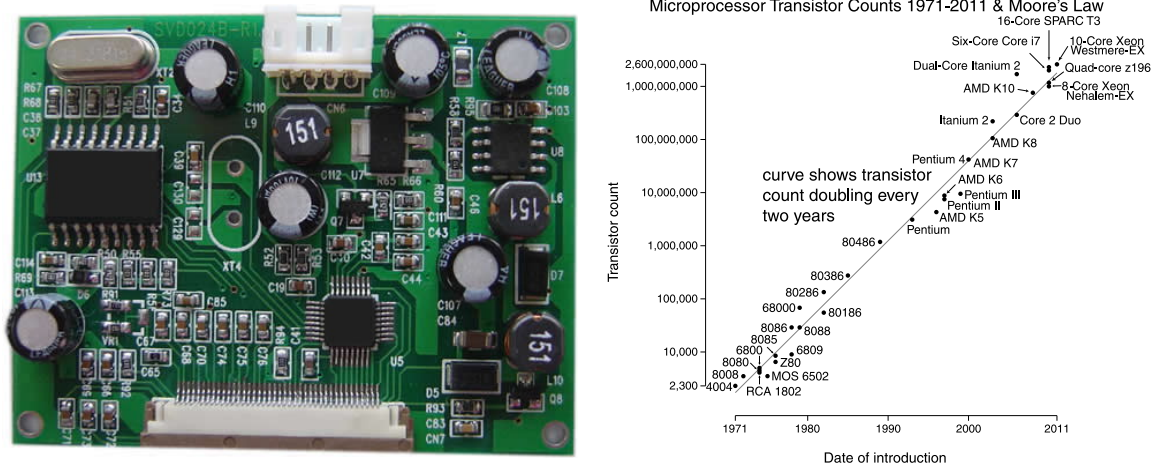


Figure 1 – Example circuit board (left) with electronic components, which have greatly decreased in size over the last generation. A characteristic measurement used to quantify this progress has been the number of transistors found in a CPU (right), which has been found to increase exponentially. The so-called Moore's law, the prediction that the number of CPU transistors doubles every three years, plotted as a line on the logarithmic plot, fits the data surprisingly well. (Images courtesy of <http://info.zentech.com> and <http://commons.wikimedia.org>.)

As the feature size in circuits continued to drop, the problem of particle contamination within the plasma process grew. As substrates are subjected to the etching process, the material removed from the surface can collide with the product rather than being quickly removed from the plasma, with damage to the chip often occurring. Large particles removed from the substrate may also levitate during the process (as explained in Chapter Three), which can then fall onto the wafers once the plasma is extinguished. This was first documented by IBM (Selwyn 1994), and fueled the drive to research plasma with intentionally inserted macroparticles. Due to the level of detail added to the

physical laws discovered for basic plasma, this field is referred to as complex (or dusty) plasma.

Although dusty plasmas began to be examined in the laboratory in 1992, it has been a fascination since humanity first observed a comet (Shukla 2002). At a critical distance from a star (5 AU for our sun), the frozen nucleus of a comet begins to boil and a coma is born. The tail is typically plasma, and analysis of it provided the earliest indication of an interaction of the solar radiation with dust (Mendis 2013). Horányi showed that micrometer dust particles interacting with the magnetic field of the solar wind could reside upon one side of the cometary orbital plane, proving that the dust had become charged (Glanz 1994). Other astrophysical examples of dusty plasmas include the zodiacal light where sunlight scatters from space dust, and nebulas such as the Orion and Lagoon. Plasma is also found in the atmosphere, such as the ionosphere where ionized particles provide reflection of radio waves for global transmission or noctilucent clouds in which dust grains can stimulate the formation of ice crystals which form the Earth's highest altitude clouds. The first theory of dusty plasmas may have been put forward by Spitzer in 1941, who investigated the basics of interstellar dust charging. In 1954, Hannes Alfvén postulated that the planets in our solar system formed from the coagulation of dust (Merlino 2004). The first experimental data collected in space relating to dusty plasmas may be from the 1980 Voyager I images of Saturn's rings (Goertz 1989). Radial lines found in the B ring from 1.52 to 1.95 times the radius of Saturn, referred to as "spokes," (Figure 2) were found to be levitating micrometer and sub-micrometer-sized particles (Morfill 2005). The final major astrophysical connection

to dusty plasmas comes from protoplanetary science, and induced particle coagulation within plasma now has a footing in laboratory experiments (Du 2010).

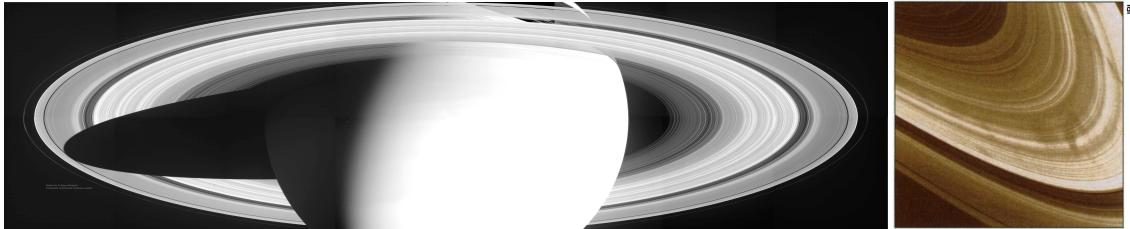


Figure 2 – The components of Saturn’s rings (left) have been found to exhibit macroscopic features based on the physics behind complex plasma (courtesy of NASA 2004 <http://www.air-and-space.com>). The presence of spokes (right) provides one example (Glanz 1994).

The largest magnetic confinement fusion device (tokamak) in the world, ITER, (schematic shown in Figure 3) is currently being built in southern France. As an international collaboration, it is scheduled to come online in November 2020 and has a total funding of 15 billion Euros (BBC 2012 <http://www.bbc.co.uk/>).

Dust in fusion machines can cause disruptions and radiation loss, both of which stimulate turbulent behavior such as edge-localized modes (ELM). Experiments involving dust driven impurities have been conducted in fusion devices including DIII-D, Alcator C-Mod, JET, and TEXTOR (Liu 2012). The source is chiefly the plasma wall interaction, where container material can react with and enter the chamber. Processes found to generate the contamination in fusion machines include desorption, arcing, sputtering, evaporation, and sublimation. Specifically, in deuterium-tritium (DT) fusion reactions tritium decays into ^3He , and neutrons created in the reaction can cause spallation reactions. It is estimated that the divertor located at the bottom of ITER and designed to collect the alpha particles (^4He), which are products of the reaction, will have

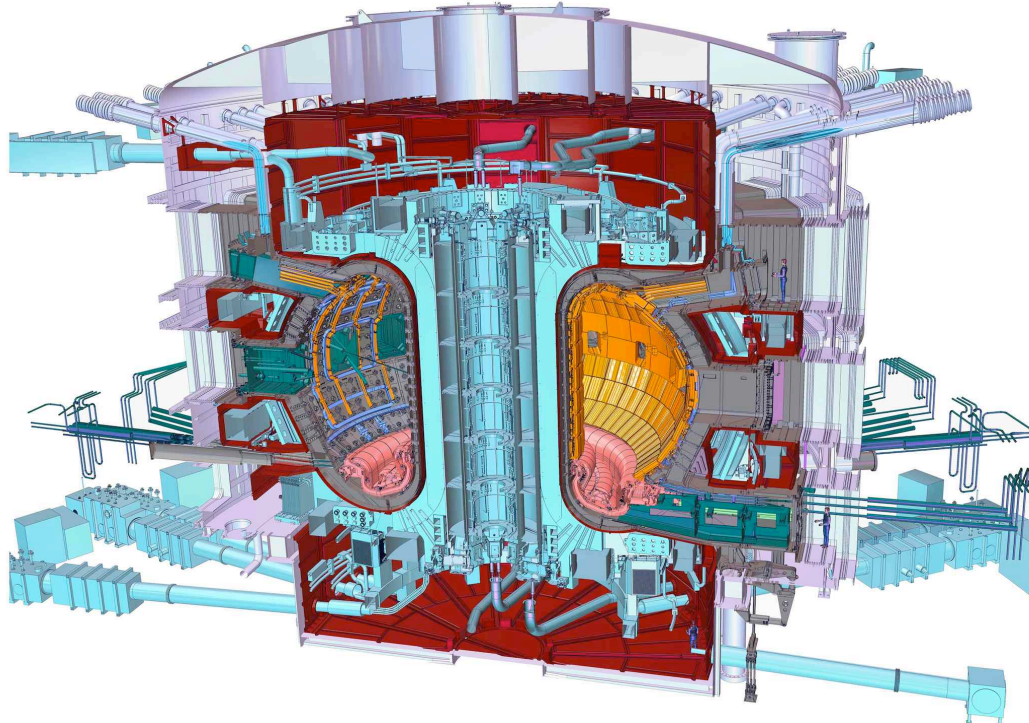


Figure 3 – A schematic of ITER cut through the center, which is designed to be the largest tokamak in the world. The inner chamber is in the shape of a torus to provide the greatest ability to connect magnetic field lines. This provides the best confinement since charged particles spiral around magnetic field lines. Wall erosion is a significant and serious issue; the cross-section of the inner chamber is in a D shape so that the poloidal magnetic field lines end at the divertor located at the bottom of the reactor, providing a particular region to direct waste. In a working fusion reactor, some alpha particles (Helium nuclei) are necessary to maintain the high temperatures necessary to keep the reaction going, but others must be removed to prevent damage to the walls.

to withstand energy absorption at a rate of 40 MW/m^2 (Pitts 2010). This will no doubt fuel particulate contamination, as divertor material will be unlikely to perfectly withstand such a bombardment. Pyrolysis, chemical reactions without oxygen at high temperatures, can also occur.

Experimentally, complex plasmas have a variety of forms. Q-machines (Rynn 1960), where a hot plate generates plasma in a low-pressure environment, were originally used to study basic plasma (shown in Figure 4). The first complex plasma machine may have been a transformed Q-machine, which ionized added potassium atoms on the surface of a

2,500 Kelvin tantalum plate. Direct current (DC) setups exist with a large potential difference between electrodes to ionize the neutral gas. In 1988, the Gaseous Electronics Conference (GEC) agreed upon a design for a radio frequency (RF) reference plasma cell with a showerhead electrode acting as an antenna, broadcasting at a frequency of 13.56 MHz (Hargis 1994). This allowed for a unification of research across different groups, which continues to present day experiments, as further explained in the next chapter. Both DC and RF experiments have also been carried out on the International Space Station (ISS), including the “Plasma Kristall Experiment” (PKE)-Nefedov (2001–2005) and PK-3 Plus (since 2006) (Kretschmer 2011). In orbit, microgravity provides the opportunity for much higher symmetry resulting in three dimensional structures, such as voids, not observed on Earth.

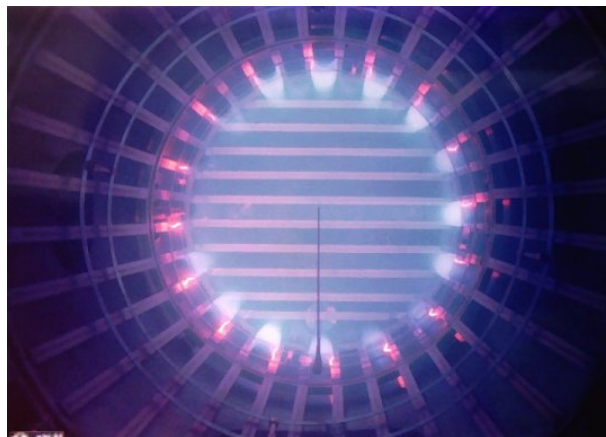


Figure 4 – A plasma inside of a Q-machine, with a Langmuir probe inserted (courtesy of <http://www.plasma.inpe.br>).

Large particle (relative to the plasma species) lattice formations in plasma were first predicted theoretically by Hiroyuki Ikezi (1986), though strong coupling (see Section 3.2.3) Coulomb structures were discussed much earlier. Ikezi noted that polystyrene

particles become charged in water and form these lattices, but added the screening effect to predict the analogous effect with micrometer-sized particles in plasma. The discovery of the levitation of micron-sized particles in a GEC RF reference cell led to the experimental realization of dust “crystals” in 1994 (Figure 5), which can form as both single and multiple layer hexagonal lattices. Much larger than molecular crystals, the principal component of a dust crystal can be observed using visible light. It was quickly determined that the interdisciplinary nature of the field provides a great opportunity for analogy to solid-state physics. From this, dust phase states (solid, liquid, gas) have been defined by the speed of the particles and analogous (to crystal) waves propagated either through the particles or the plasma. Methods to quantify the level of crystallization have been developed.

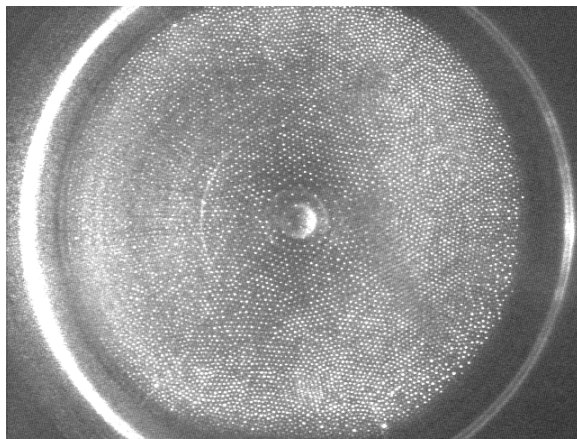


Figure 5 – Typical single layer complex plasma dust crystal formed at 10 W system power and 650 mTorr neutral gas pressure with 8.89 micrometer diameter Melamine Formaldehyde particles. The particles organize into hexagonal symmetry.

Magnetism in plasma experiments has uncovered a host of new and interesting phenomena. In fusion machines, where magnetism is critical for confinement, several plasma drifts were found that have to be countered to maintain confinement. Plasma

waves were found to be generated and dependent on magnetic field. Magnetic dusty plasma experiments with fields up to 4 Tesla have been conducted extensively in Garching, Germany at the Max Planck Institute for Plasma Physics (MPE), and plans are underway for a more customizable 4 Tesla field at Auburn University (Thomas 2012). Rotation of the crystal, plasma filaments, fountain formation, potential modification, and waves, all involving dust, were found. Although no studies primarily involving magnetic fields are contained in this work, it should be noted that because electric currents form magnetic fields, minor magnetic effects may be nevertheless present.

Manipulation of dust in a complex plasma crystal has been accomplished by modifying the electrode bias, applying radiation pressure with lasers, initiating waves through the crystal by insertion of a powered horizontal wire into the system, instituting a temperature gradient to establish a force, altering the particle charge or sheath electric field by changing basic plasma parameters such as the power or neutral gas pressure, and beaming a pulsed stream of ions. As dust delivery processes have improved, single particle perturbations have been shown to occur. Under proper confinement, dust clusters in the horizontal and vertical directions have been produced, resulting in dusty plasma “magic numbers,” and Coulomb balls, respectively (Annaratone 2004). Upon the addition of vertical insulating walls for added confinement, it was found that larger clusters could be produced by increasing the RF electrode peak to peak voltage (because electric potential shielding increases). Single and multiple chains have also been produced, and even helical structures under appropriate sets of conditions (Hyde 2013). Kinematics of particles exhibited such phenomena as thermal creep and waves. Both

dust acoustic waves, where the dust follows the plasma, and dust lattice waves, where particles interact with each other, have been observed.

In this series of dusty RF plasma experiments, a powered vertical probe was inserted into a GEC cell and found to produce three distinct dust interactions. First, a vertical oscillation experiment was carried out that resulted in asymmetric motion of a single dust grain, differing from all previous vertical oscillation studies. Second, the probe was used to perturb a dust crystal lattice, opening an empty cavity, similar to the voids seen in DC driven experiments (Thomas 2004) and on the ISS. Third, system confinement was employed to align a vertical chain of dust particles and the probe was then used to perturb this chain to generate both longitudinal and transverse waves.

Organization of the dissertation is as follows. In the next chapter, the main experimental apparatus and all supporting hardware will be explained. In Chapter Three, the background necessary for a proper understanding of the dusty plasma research at hand will be discussed, and the experimental procedure described. In Chapter Four, the basic results from the three experiments will be shown. Then in Chapter Five, analysis of the experiments will be carried out. Finally, the conclusions will be reported in Chapter Six. Appendices will include supporting data, as well as all relevant computer codes written for Mathworks MatLab, Wolfram Mathematica, and the National Institute of Health's ImageJ software.

CHAPTER TWO

Equipment

2.1 GEC Cell

In 1993, a report verified the feasibility of similarity in production of the original GEC reference cell by comparing six equivalent experiments performed at different institutions (Hargis). A modified GEC plasma RF reference cell (Land 2009) is employed at the Hypervelocity Impacts and Dusty Plasma Laboratory (HIDPL), part of the Center for Astrophysics, Space Physics, and Engineering Research (CASPER), for this research (Figure 6). Two electrodes, each 8 cm in diameter and separated by 1.9 cm, power the plasma inside the cell. The lower electrode acts as an antenna broadcasting at 13.56 MHz while the upper electrode is ring-shaped with an annular width of $\frac{1}{4}$ " and acts (as do the chamber walls) as a ground. Since the upper electrode is open in the center it allows visual and physical access to the plasma. Other experiments (for example, the PKE-Nefedov) have employed similar designs but operated the electrodes in a push-pull manner (Lipaev 2007), to enhance symmetry.

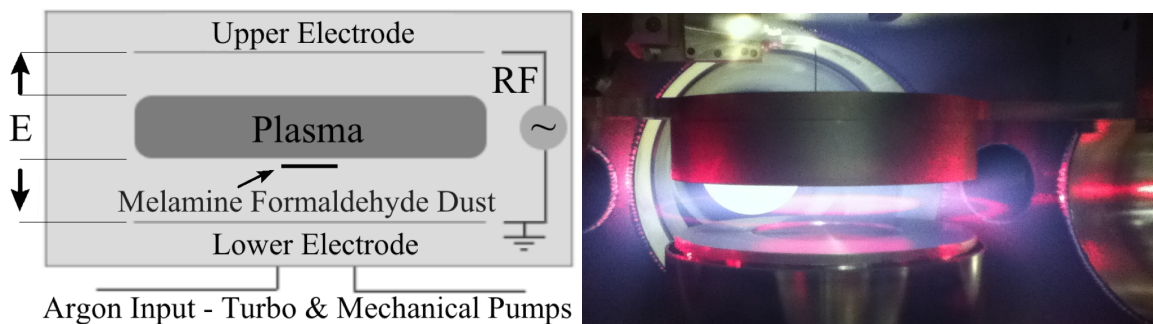


Figure 6 – A schematic (left) of the GEC cell (right) used in this experiment. Small, spherical particles levitate in the lower sheath of the plasma, for reasons explained in Chapter Three.

In the experiments discussed here, micrometer-sized melamine formaldehyde (MF) dust particles were introduced into the plasma by physically agitating a dust container fixed above the upper electrode. Other experiments have used different types of dust, for example, aluminum oxide (Al_2O_3), kaolin, and silicon dioxide (glass) (Shukla 2002). As the dust particles fall through the plasma, they charge as discussed in Section 3.2.1, which allows them to levitate above the lower electrode as explained in Section 3.2.2. Horizontal confinement of the dust particles is provided by plates having a central milled circular cutout between 1-3 mm deep and 0.25-2” diameter placed on the lower electrode. Images of the dust particles are captured at 60, 125, and 250 frames per second using top and side-mounted CCD cameras. The actual power delivered to the plasma was calculated by measuring the phase difference between the current and the voltage. The DC bias of the lower electrode was held fixed using an external power supply (Harris 2013). Langmuir probe measurements of the bulk plasma were also collected using a SmartProbe (Scientific Systems Ltd) (Land 2009). Tables 1 and 2 list the available system parameters.

Table 1 – CASPER GEC Cell available plasma parameters.

System Power	Pressure	DC Bias	Dust Sizes	Cutout Sizes
1 to 15 W	50 to 700 mTorr	0 to -100 V	0.46 to 12 μm dia.	0.25” to 2” dia.

The chamber is operated at ‘low’ pressures to allow plasma to be produced at ‘low’ power. Two roughing pumps (a roots RUVAC WS 151 and a rotary vane TRIVAC D 25 BCS) were used to reach low vacuum, which is used during operation. A turbo pump (Alcatel 5401CP) was used to reach high vacuum (10^{-6} Torr), and is employed at all times

Table 2 – Selected Langmuir probe parameter results for the plasma bulk in the cell used for these experiments (Creel 2010).

Power	Pressure	Electron Temperature	Electron Density	Plasma Potential
1 W	100 mTorr	9.09 eV	4.99e8 cm ³	39.5 V
1 W	300 mTorr	7.99 eV	3.16e8 cm ³	31.7 V
5 W	100 mTorr	7.40 eV	1.75e9 cm ³	37.6 V
5 W	300 mTorr	8.94 eV	1.82e9 cm ³	41.2 V
10 W	100 mTorr	5.43 eV	2.68e9 cm ³	33.9 V
10 W	300 mTorr	8.66 eV	3.02e9 cm ³	41.7 V

when the cell is not in use. This aids in removal of any contamination that may have adhered to the walls such as water vapor, particle growth facilitated by the plasma, or anything introduced during an opening procedure.

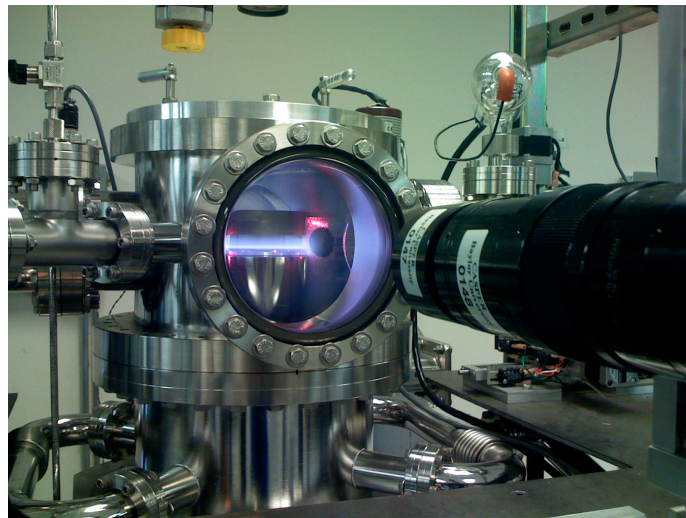


Figure 7 – CASPER plasma cell 2, ignited with background Argon gas (purple glow), illumination provided by HeNe lasers (red glow), data acquired by cameras (right and top), dust dropped by shakers (two handles shown at top), and high vacuum pressure measured by an ion gauge (top right).

2.2 Zyvox S100 Nanomanipulator

A Zyvox S100 (Zyvox 2010) head, which was originally designed for sample manipulation in microscopy applications, was attached within the plasma chamber to act as a perturbation tool (see Section 4.2). It has four connections capable of programmable remote controlled independent movement by up to 10 mm in all three dimensions. This saves time by not having to break the “chamber vacuum” every time the position of a device in the cell needs to be adjusted, as required for all previous similar experiments.

A hollow cylindrical tungsten probe 48 mm in length, with an outer diameter of 450 micrometers, was connected to one of the connections in the S100 head such that it was aligned vertically. A tip, with an adjustable length of up to 14 mm and a diameter tapering from 250 to 50 microns over the last 100 micrometers, protruded from the probe. The probe potential was controlled with respect to the ground using an external power supply (KEPCO BOP 500M), and shaped using a signal generator (Hewlett-Packard 8657A). Current at the probe tip was measured by placing an ammeter in series between the power supply and the probe.

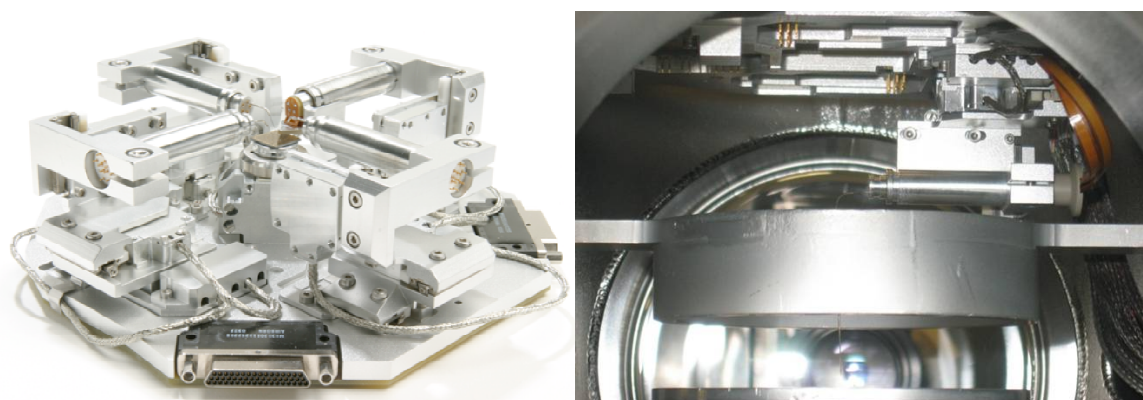


Figure 8 - The Zyvox S100 Nanomanipulator head (left, courtesy of <http://www.zyvox.com>) is located inside the plasma cell, mounted upside down above the upper ring electrode (right). One of the four manipulators shown is used in this experiment to position the probe as described in the text.

2.3 Other Equipment

To illuminate the dust particles, two Helium-Neon class IIIb laser beams are shaped into vertical and horizontal planes and introduced into the cell. They produce 632 nm (red) light using 50 mW of power. This allows a side view and a top view, respectively, for the two mounted cameras. A class IV Verdi laser can also be employed which produces 532 nm (green) light at up to 5 W. This is strong enough to perturb the dust particles, and has the advantage that it interacts very little with the plasma. However, the power cannot be adjusted in a sinusoidal fashion, and so it is currently limited to a pulsed nature, using a rotating filter. For added dust confinement in the horizontal and vertical directions, an open glass box can be placed upon the lower electrode.

As explained further in Chapter Three, all surfaces charge up negatively if there is no path for the charge to escape. Since a blocking capacitor is placed between the power supply and the lower electrode, current at a high oscillation frequency passes through but low frequency current does not. Therefore, a DC bias on the lower electrode is allowed to form, making the setup a capacitively coupled discharge. Both CASPER GEC cells employ a power supply connected to the lower electrode, providing the option to establish a constant DC bias. A signal generator can also be added to modify the DC bias on the lower electrode in a systematic manner.

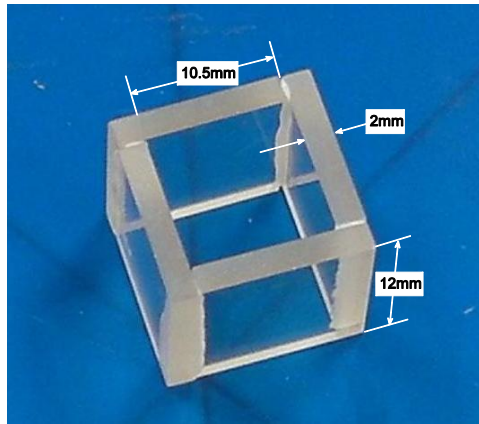


Figure 9 – Glass box placed on the lower electrode to facilitate greater horizontal and vertical confinement.

CHAPTER THREE

Complex Plasma Fundamentals

3.1 Basic Plasma

3.1.1 Criteria

Plasma has been defined to be a “quasineutral gas of charged and neutral particles, which exhibits collective behavior” (Chen 2006). Plasma can be generated by heating any matter to the temperature at which ionization occurs, usually a few thousand Kelvin. It can also be formed by beaming electromagnetic waves of sufficiently high energy, at or above the particular matter’s work function, to eject electrons from the constituent atoms. The ionization source must be strong enough and/or the plasma density low enough to sustain a high enough degree of ionization to exhibit the collective effects (Gurnett 2005).

To determine exactly how much ionization is required to classify a volume of matter as plasma, the Debye length must be introduced. First, it must be understood that because the mass of an electron is 1,836 times the mass of a proton, the inertia of a plasma ion is 3-4 orders of magnitude larger than that of a plasma electron (for example, 72,821 times larger for the mass of an Argon ion). This means upon the addition of a charge, due to the direct Coulomb interaction force and Newton’s second law, the plasma electrons quickly respond to an electric field. This works for both positive and negative test charges – electrons surround the former, and flee from the latter. The potential at a particular distance from the charged particle can be found using the Poisson equation of electrodynamics,

$$\nabla^2 \phi = -\frac{\rho}{\epsilon_0} = -\frac{e(n_i - n_e)}{\epsilon_0}, \quad (3.1)$$

where ϕ is the electric potential, ρ is the net charge density, ϵ_0 is the permittivity of free space, e is the elementary charge, $n_{i(e)}$ is the ion (electron) density (which equals the equilibrium density n_0 when examined sufficiently far away from the charged particle), and the electrons in thermal equilibrium are assumed to have the density ($\phi < 0$),

$$n_e = n_0 e^{e\phi/\kappa T_e}, \quad (3.2)$$

where κ is the Boltzmann constant, and T_e is the electron temperature. The exponential can be expanded and the series truncated at the linear term under the assumption that the argument is less than one. This expansion is valid for small charges or at a sufficient distance from the charge (for example, 10,000 electron charges, for a system power of 10 W and a neutral gas pressure of 100 mTorr, requires a distance of greater than 13 microns). This leads to differential equations that have simple solutions in both one and three dimensions. The three-dimensional solution is

$$\phi = \frac{Q}{4\pi\epsilon_0 r} e^{-r/\lambda_D}, \quad (3.3)$$

where Q is the amount of charge generating the disturbance, r is the distance from the charge, and λ_D is defined from the result of Eqn. 3.3 to be the Debye length, with the form

$$\lambda_D^2 = \frac{\epsilon_0 \kappa T_e}{n_0 e^2}. \quad (3.4)$$

The one-dimensional solution has the same exponential factor but the coefficient is simply the initial potential. The two dimensional solution involves Bessel functions (Bendetti 2006). In each case, the coefficient is assigned by taking the limit as r goes to 0. Though the three dimensional solution goes to infinity as r goes to 0, it matches the Coulomb potential at small r . If the ions are mobile, this expression can be extended in the following manner

$$\frac{1}{\lambda_D^2} = \frac{1}{\lambda_{D_e}^2} + \frac{1}{\lambda_{D_i}^2}. \quad (3.5)$$

For a pure argon RF plasma, generated at 10 W of system power and 100 mTorr of pressure, corresponding to a density shown in Table 2, the electron Debye length in our machine is 3.3×10^{-4} m.

By taking the negative derivative of the potential given in Eqn. 3.3, to find the electric field, one discovers it is a simple reduction from the Coulomb field where the Debye length specifies the distance at which the collective effect of plasma has a significant effect. In other words, the Debye length must be less than the length of the machine for the plasma definition to hold. As the value derived above for our operating conditions is much less than the chamber size, our machine passes this test. In order to work effectively, there must also be a sufficient number of electrons available in the working volume. To this end, a Debye cube is defined as the Debye length cubed. $\lambda_D^3 n_e$ yields the expected number of electrons in that volume. For shielding to occur, this number must be much greater than one. Using the Debye length found above and the same plasma density as before yields a value of 1.0×10^5 electrons per Debye cube, and so our machine satisfies this requirement as well.

The final condition deals with the difference between molecular collisions versus plasma oscillations. If thermal collisions dominate the gas, then it will not behave as plasma. Again due to the high electron mobility compared to the ions, any electric disturbance to the plasma causes the electrons to move. Since electrons have mass, inertia causes them to overshoot their equilibrium position; the frequency at which they do this is called the plasma frequency. This value can be determined by considering a

small sheet of plasma. If electrons are displaced to the left, the ions will remain behind on the right. By Gauss's law, the electric field in the center neutral region will be

$$E = \frac{\sigma}{\epsilon_0} = \frac{n_0 e x}{\epsilon_0}, \quad (3.6)$$

where σ is the surface charge density, and x is the displaced distance. Using Newton's second law, $F = ma$, where the electric force is $F = QE$ assuming no magnetic field, generates the harmonic oscillator differential equation. The characteristic restoring frequency is the coefficient of the displacement term when the equation is rearranged such that the acceleration has a coefficient of 1,

$$\omega_p^2 = \frac{n_0 e^2}{\epsilon_0 m_e}, \quad (3.7)$$

where m_e is the mass of an electron. Note that if the ions were instead considered, the mass of an ion would be substituted. Using the same conditions as for calculating the Debye length, the electron plasma frequency is 4.6×10^8 Hz, whereas the ion plasma frequency is 1.8×10^6 Hz. The driving frequency, 13.56 MHz, is 7.7 times larger than the ion plasma frequency, which is too large for the ions to be stimulated. Since the driving frequency is much less than the electron plasma frequency, the electrons respond but the resulting plasma is only slightly ionized (Samsonov 1999). Employing the ideal gas law allows estimation of the amount of ionization. The background density should be $P/(\kappa_B T)$, where P is the pressure in Pascals, κ_B is the Boltzmann constant, and T is the temperature in Kelvin (assuming room temperature of 294 K); at 100 mTorr this results in $n_n = 3.3 \times 10^{21} \text{ m}^{-3}$, a ratio of electron ($2.7 \times 10^{15} \text{ m}^{-3}$) to neutral density of 8.2×10^{-7} . Near the electron plasma frequency one would expect a resonance effect to increase the amount of ionization.

Analysis of thermal collisions involves a series of quantities, which can be measured through experiments. The mean free path is the average distance a neutral gas particle travels before physically colliding with another neutral gas particle,

$$\lambda_m = \frac{1}{n_n \sigma}, \quad (3.8)$$

where n_n is the neutral gas density, and σ is the total cross-section. If the mean free path of a particular species is desired, the cross-section can be adjusted accordingly in Eqn. 3.8. Both the scattering cross-section and the charge-exchange cross-section, with the latter being defined as when an ion collides with a neutral atom and steals an electron, have been measured for Argon (Lieberman 2005). To determine whether the plasma may be considered to be collisional, it is sufficient to focus on the ions since the electron cross-section will be smaller, increasing their mean free path above that for the ions. The time between collisions may be found by λ_m/v , where v is the average velocity of the particles. The inverse of the average collision time yields the collision frequency. Again using the density listed above and the electron temperature found for the same case shown in Table 2 to find the cross-section from the plots reported by Lieberman (2005), the ion mean free path can be shown to be 429 micrometers.

A useful result of statistical mechanics is the Maxwell-Boltzmann distribution function,

$$f(v) = n \left(\frac{m}{2\pi kT} \right)^{3/2} e^{-v^2/v_T^2}, \quad (3.9)$$

where v_T is the thermal velocity of the species (defined here as $(2kT/m)^{1/2}$), which determines the distribution of velocities of the single species particles that constitute an ideal gas. It has been verified experimentally by the Stern-Zartman experiment (Zartman

1931). This distribution is valid in plasma and was used to derive the electron density above (Eqn. 3.2), by calculating

$$n = \int_{-\infty}^{\infty} f(u)du. \quad (3.10)$$

If the ions are mobile Eqn. 3.10 can also be used to derive a similar ion density function. The thermal velocity is found by setting the energy (in multiples of $0.5\kappa T_e$) equal to the kinetic energy and solving for the velocity. Doing this for the conditions already mentioned yields an electron thermal velocity of 1.38×10^6 m/s, and an ion thermal velocity of 347 m/s, reiterating the massive difference in electron mobility. Other notable velocities can be found from the distribution function, for example the root mean squared and the average velocities. To find the average kinetic energy, one may use

$$E_k = \frac{\int_{-\infty}^{\infty} \frac{1}{2}mu^2 f(u)du}{\int_{-\infty}^{\infty} f(u)du}. \quad (3.11)$$

This results in $0.5\kappa T_e$ of average energy per degree of freedom. The averages of other gas characteristics are often found with this basic form. Finally, the components have been established to consider the third requirement: $\omega_p \lambda_m / \nu > 1$. Using the values found above, this relation yields a value of 573, so thermal collisions do not dominate.

Because it is conceivable that the ion-electron collisions could also complicate the situation, a formula to include this effect exploiting the connection between plasma conductivity and the collision frequency, with the assumption of fully ionized plasma, has been derived,

$$\nu_{ei} = \frac{n_0 e^4}{32\pi^{1/2} \epsilon_0^2 m_e^{1/2} (2\kappa T_e)^{3/2}} (12\pi n_0 \lambda_D^3), \quad (3.12)$$

which yields a result of 0.3 ms per collision (Gurnett 2005). Despite the enormous number of electrons available (2.6×10^{11}) in the plasma volume (9.6×10^5 m³), and the high

speed at which they move, both of which enhance the probability of collisions, ion electron collisions are negligible.

Summarizing, it has been shown that the three quantitative requirements have now been met for the GEC RF reference cell used in this project. The (1) Debye length is much less than the size of the machine, (2) the number of ionized particles in the Debye cube is much less than one and (3) the plasma frequency times the average collision time is greater than one.

3.1.2 Sheath

Once again due to the high mobility of electrons compared to ions, electrons are the first to arrive at the walls of a machine. If the walls are insulated, a negative electric potential develops which grows to the point where other electrons are repelled. If the walls are grounded, electrons are lost from the plasma, creating a net positive plasma potential. As mentioned above, the lower electrode in the machine employed for the present experiments is allowed to collect charges, engendering a greater potential difference where in either case, ions are naturally attracted to these relatively negative surfaces. In the steady state, this establishes an electric field that increases in magnitude as the distance to the walls is reduced.

If the plasma is in a collisionless state, there is a limitation on the speed of ions that exit the plasma (Bohm 1949). As seen above, although plasma under our conditions will exhibit some ion collisions, it can still be approximated as a collisionless plasma. Under this assumption, conservation of energy is maintained as the ions move through the electric field of the sheath toward the surface of the lower electrode. Given the potential, the velocity of the ions is

$$u = \left(u_0^2 - \frac{2e\phi}{m} \right)^{1/2}, \quad (3.13)$$

where u_0 is the initial velocity when $\phi = 0$ V; this results in acceleration of the ions as they move toward the walls. In our machine an electrode cutout can also be used, at least in the center, to assume that a planar continuity equation will hold. Using Eqn. 3.13 in the continuity equation yields the ion density in the sheath,

$$n_i = n_0 \left(1 - \frac{2e\phi}{mu_0^2} \right)^{1/2}. \quad (3.14)$$

This has the effect that the density of ions decreases as they are accelerated toward the lower electrode. When Eqn. 3.14 is substituted into the Poisson equation (Eqn. 3.1), this leads to a solvable differential equation only if the speed is greater than or equal to the Bohm velocity,

$$v_B = \sqrt{\frac{\kappa T_e}{m_i}}. \quad (3.15)$$

This is also known as the ion sound speed or Mach number. It is these streaming ions that facilitate industrial plasma surface etching and deposition. Under the conditions used for estimation in the previous section, the Bohm velocity is 3,620 m/s, 10.4 times larger than the ion thermal velocity.

Many attempts have been made to locate a singular position that separates the plasma from the sheath, defining the sheath edge. Initially, the location of the sheath edge was approximated by marking a position based in the change in optical emission from the plasma (Melzer 1994, Tomme 2000). One standard definition is the position where the ions reach the Bohm velocity (Chen 2006). Subsequent discussion led to a reworking of this definition to find instead an electron edge, defined to be the point where the electron charge below a point equals the net positive charge above that point up to the center of the plasma (Brinkmann 2007). A more recent method for higher pressures employs dust

particles as probes in the sheath, determining the sheath edge by increasing the RF voltage amplitude (increasing the plasma power) until the dust reaches a stable vertical position, which approximates the sheath edge because the upward electric force increases (because the dust charge increases) with plasma power (Douglass 2012). Beckers et al. proposed the sheath edge definition used in the first experiment, which is where the plasma emission is reduced by a factor of $1/e$ (2011). An alternative experimental method to determine the sheath edge as defined theoretically is predicated on measurement of the equilibrium height of nanoparticles (Samaritan 2001), which is used later in the present work. Applying the Beckers definition of the sheath edge to Figure 4 in (Samaritan 2001) (Figure 10) results in agreement within 0.7% in vertical position, justifying this choice. This is excellent agreement considering uncertainty in emission intensity due to plasma fluctuations, nonuniform background light contamination, and image resolution. The relevant system parameters for Samaritan's experiment are a pressure 90 mTorr and a power of 80 W. Though at much higher power, the pressure is the main parameter that determines the sheath thickness (see Section 5.3.3).

All methods provide challenges in determination of the sheath edge. Utilizing the increasing power method described yields a sheath edge located farther above the lower electrode than does the $1/e$ point. However, pressures below 150 mTorr prevent application of their numerical model for plasma densities (due to known fluid model restrictions), leaving results for V_{rf} below 15 V where some of the present experiments are conducted not established. Also, for low pressures (50-100 mTorr) Samaritan found that the particles continue to fall from 35 W to 100 W, which are much higher powers

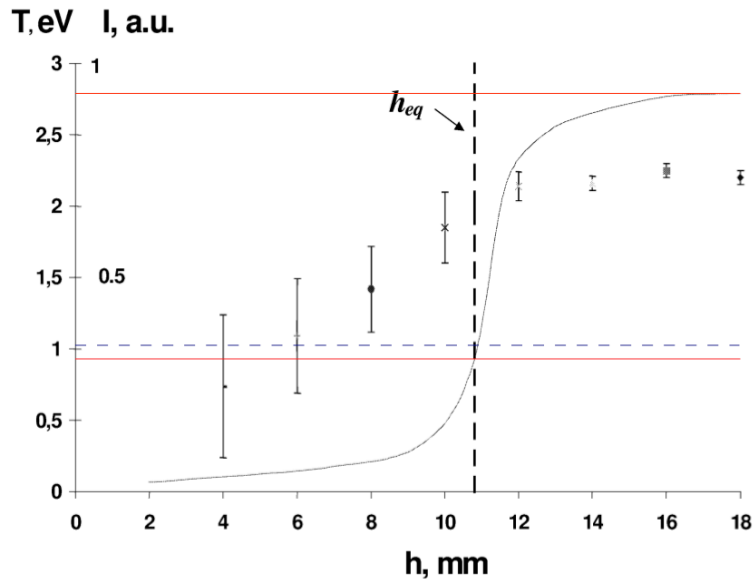


Figure 10 - Electron temperature and emission intensity as a function of height from Samarian et al. (2001), with added horizontal lines. The bottom (red) line is where the optical emission (solid curved line) crosses the equilibrium height of small particles and therefore defines the sheath edge. The dashed (blue) line above is where the maximum optical emission intensity decreases to $1/e \times$ bulk intensity. Finally, the top (red) line is the location of the maximum emission intensity, drawn to note that it is not normalized to 1. The original points are probe measurements of the electron temperature as a function of the height. The height at which the temperature change levels off is another indicator of the sheath edge and represents a confirming measurement.

than possible with the current hardware, making this method infeasible. Therefore the Samarian method will be used to provide a process to supplement overall model limitations. Additionally, although the levitation of nanoparticles provides a useful experimental method for determining the sheath edge (for the second and third experiments), it cannot be used over our range of dust sizes simultaneously with larger dust particles (required for the first experiment) for multiple reasons. First, smaller spherical particles scatter more light and can only be distinguished by their levitation height. Rayleigh scattering works for particles much smaller than the wavelength, but when the particle diameter is above 10% of the incident wavelength Mie scattering takes over. As a representative example, when lit by a red laser (with wavelength λ of 632

nm), 8.89 micrometer particles have diameters 14 times greater than λ , and laboratory available nanoparticles with a 460 nm diameter are 73% of the illumination wavelength. The importance of this scattering is seen in the first experiment (introduced in Section 4.2) where the diameter of the 8.89 micron grains appeared to be 6 pixels in width, corresponding to a 138 micron diameter. If the larger experimental dust is present at the same time as the nanoparticles used to find the sheath edge, a second problem occurs because the nanoparticle height could change by interaction forces from the other particles. The alternative is to only drop the nanoparticles, and then extinguish the plasma to evacuate them before adding dust of the size necessary to conduct the experiment. Unfortunately, this technique is completely infeasible for experiments requiring modification of parameters that change the height of the sheath during the data acquisition. Therefore, determining the sheath edge concurrently through analysis of the optical emission intensity provides the best solution for experiments requiring for low powers/pressures and incorporating the loss of electrons to the macroparticles. For higher pressures and powers, where reproducibility is not a problem, and simultaneity is not required, the levitation of nanoparticles provides a better solution. Once a model has been sufficiently experimentally verified, such as a more rigorous emission intensity investigation over a larger parameter space, it may supersede this method's applicability.

3.1.3 Sheath Electric Field

Simple electric field models of the sheath potential have been vigorously explored in the steady-state. One recent paper summarized nine separate methods from theoretical and experimental papers that either use or could be approximated to use parabolic sheath potentials with good agreement, especially below the sheath edge (Tomme 2000).

Hence, there is justification for assumption of a linear electric field in the sheath. This is achieved by first supposing a generic parabolic potential,

$$V(z) = Az^2 + Bz + C, \quad (3.16)$$

and assuming the potential spans the fixed DC potential on the lower electrode ($C = V_0$) where $z = 0$ to the plasma potential (V_p) at the sheath edge ($z = d$). This leads to a solution of the constants as

$$A = \frac{V_0 - V_p}{d^2} \quad B = \frac{2(V_p - V_0)}{d}. \quad (3.17)$$

It is known that ions stream from the plasma and are accelerated within the sheath (Chen 2006). A valid question is how much distance is required to accelerate the ions to the Bohm velocity in the presheath. This can be determined by making the approximation that ions start with zero velocity (though really they have a small thermal speed) at a height d from the lower electrode and are then accelerated by a linear electric field within the sheath (assuming this field extends slightly into the bulk). Integrating over the electric force,

$$\frac{1}{2}m_i v_b^2 = \int_d^{z_1} QEdz, \quad (3.18)$$

where m_i is the ion mass, v_b is the Bohm velocity, Q is the ion charge and E is the electric field, yields the work done to an ion, and solving for the upper limit yields the desired result,

$$z_1 = d \left[1 - \left(\frac{kT_e}{2Q(V_p - V_0)} \right)^{1/2} \right]. \quad (3.19)$$

Figure 11 shows a plot of Eqn. 3.19 as a function of the electron temperature. Given the bulk electron energy of the first experiment, 9.2 eV, and assuming singly ionized Argon ions at rest before acceleration, $z_1 = 1.4$ mm. Assuming the ions are at room temperature, starting instead at a realistic ion thermal velocity results in an indistinguishable

acceleration distance at this electron temperature, since the Bohm velocity is 19 times larger than the thermal velocity.

From Eqn. 3.19, an interesting prediction can be made that the acceleration distance to the Bohm velocity does not depend on the mass of the ion. To calculate the position of an ion as a function of time, ignoring collisions and gravity, the appropriate differential equation can be solved to yield

$$z = d - k_0 \left(\frac{kT_e}{m_i} \right)^{1/2} \frac{\sinh(k_0 t)}{\cosh(k_0 t_b)} \quad k_0 = d \left(\frac{m_i}{2Q(V_p - V_0)} \right)^{1/2}, \quad (3.20)$$

where t_b is the time required to reach the Bohm velocity. The time of flight required to reach the Bohm velocity can now be determined by taking Eqn. 3.20 and setting it equal to Eqn. 3.19,

$$t_b = k_0 (\tanh^{-1}(k_0^2)). \quad (3.21)$$

This leads to a value of $t_b = 6.77 \times 10^{-6}$ seconds for an ion; for comparison, the same process yields $t_b = 6.56 \times 10^{-12}$ seconds for an electron. In the present experiments it is assumed that ions cross the sheath edge at the Bohm velocity in order to adjust the density and to follow the premise that ions exiting into the sheath must do so at velocities greater than or equal to the Bohm velocity (Chen 2006).

Employing an ion-neutral cross-section independently reported, the ion-neutral mean free path in our machine at 80 mTorr neutral gas pressure (used in the first experiment) is 470 microns (Beckers 2011), which is larger than for Beckers (260 microns at 150 mTorr) but still collisional. Despite this, our assumption that the ions leave the sheath at the Bohm velocity was also made by Beckers. Though this likely overestimates the ion drag on a dust particle (collisionality reduces ion speed), it is still quite small relative to the other forces (details are discussed later).

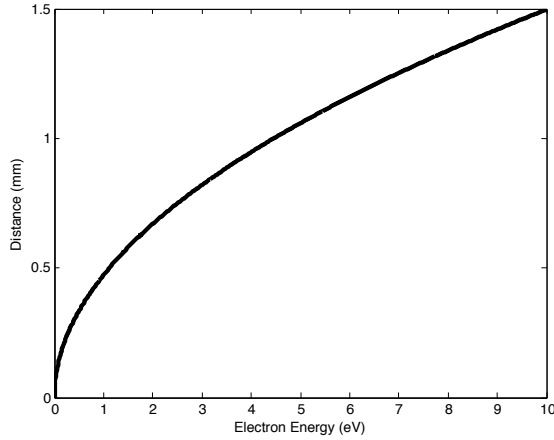


Figure 11 – Required distance for ions to accelerate to the Bohm velocity in the presheath as a function of the electron energy.

3.2 Complex Plasma Basics

3.2.1 Charging

Like the walls inside a plasma machine, any object inserted into plasma will become charged. Electrons will initially bombard the object at a faster rate than ions, and even in the steady-state, a net negative charge will remain. One option for calculating this charge is Orbital Motion Limited (OML) theory where it is assumed the object collects all charges that collide with it. The OML process begins by calculating the maximum impact parameter required for a charged particle to be collected. For a negatively charged object, naturally the electron cross-section will be smaller than the object since electrons are repelled, and the ion cross-section will be larger since ions are attracted. To solve this, conservation of kinetic energy is assumed,

$$\frac{1}{2}mv^2 = \frac{1}{2}mv_p^2 - e\phi, \quad (3.22)$$

where v_p is the velocity at the edge of object, $e > 0$ is the electron charge, and $\phi > 0$ is the potential on the object. Eqn. 3.22 represents oppositely charged colliders; to calculate for

like charges the sign of e should be flipped. It is assumed as usual in scattering problems that angular momentum is also conserved from far away to the surface of the object,

$$mvh_p = mr_p v_p \quad (3.23)$$

where h_p is the impact parameter, and r_p is the radius of the cylindrical object. This applies as well for a spherical object since the cross-section is circular. The impact parameter is solved using Eqn. 3.23 with Eqn. 3.22 and the cross-section is πh_p^2 . The total flux, the number of particles impacting the surface per second, is $n_i \pi h_p^2 v$. In order to cover all velocities, the average flux is

$$\Gamma_i = \int_0^\infty \pi h_p^2 f(u) du, \quad (3.24)$$

as the species density is included in $f(u)$. Negative velocities are not included because the projectiles will not strike the object. This yields the following for the flux of electrons,

$$\Gamma_e = \sqrt{8\pi} n_e r_p^2 e^{e\phi/\kappa T} \sqrt{\frac{\kappa T_e}{m_e}}, \quad (3.25)$$

and for ions,

$$\Gamma_i = \sqrt{8\pi} n_i r_p^2 \sqrt{\frac{\kappa T_i}{m_i}} \left(1 - \frac{e\phi}{\kappa T_i}\right). \quad (3.26)$$

Setting these fluxes equal to each other allows a numerical solution for the expected potential on the object. The argon ions are assumed to be singly ionized because electronegativity increases, requiring 15.8 eV to remove the first electron, but 27.6 eV to remove a second (NIST 1999 <http://physics.nist.gov>). The potential (ϕ) found on the dust grain in the steady state is called the floating potential. Using the experimental conditions of the previous section for an 8.89 micrometer diameter MF particle, a floating potential of -11.4 eV is found. To adjust for vertically streaming ions, the ion distribution function may be modified to be

$$f(v) = n \left(\frac{m}{2\pi\kappa T}\right)^{3/2} e^{-(v-u)^2/v_T^2}, \quad (3.27)$$

where u is the ion streaming speed, (Fortov 2004) commonly known as DML (Wörner 2012).

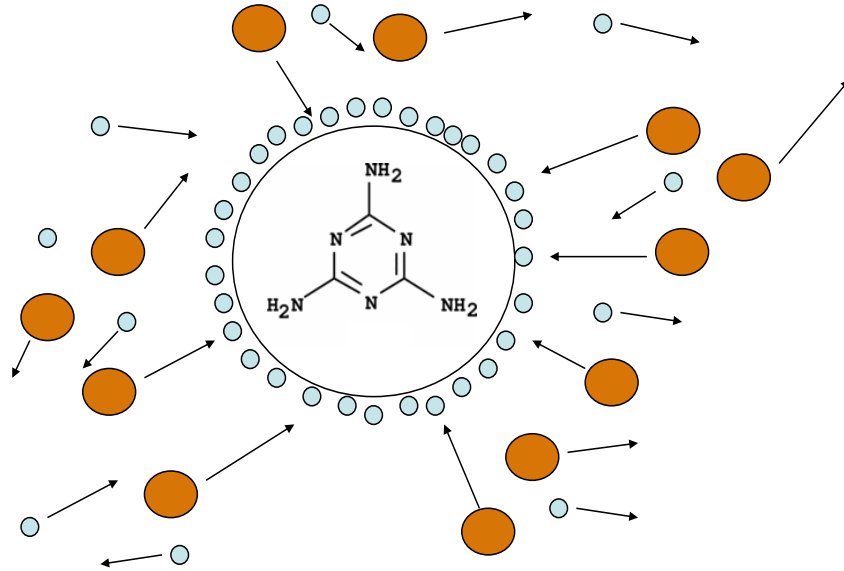


Figure 12 – Cartoon of dust grain charging mechanism, where the larger spheres are Argon ions (generally attracted at this stage), the smaller are electrons (generally repelled), and the background atoms are omitted. The center shows the molecular composition of Melamine Formaldehyde. The arrow magnitudes are a qualitative representation of momentum as the electrons have much greater speed, but the ions have much greater mass.

To determine the charge on the grain, a capacitance model is employed. Since the macroparticles used in the present experiments are spherical, the standard expression for spherical capacitance,

$$C = 4\pi\epsilon_0 r_p, \quad (3.28)$$

is used to calculate charge is collected with $Q = C\phi$. For the OML potential listed previously, the charge collected on a $8.89 \mu\text{m}$ dust grain is 35,400 electron charges, assuming the bulk plasma parameters. Finding the dust equilibrium position and applying the continuity ($n_0 u_0 = nu$, where n_0 and u_0 are the initial density and ion speed and n and u are the density and ion speed at any other position) and energy conservation (Eqn. 3.13) equations, OML yields 27,000 electron charges.

The time required for charging may now be estimated. The total electron collisions using Eqn. 3.25 above is 3.1×10^{10} electrons per second. Dividing the total charge by the number of collisions results in 1.1 microseconds. Using a previous experimental estimate of the speed of a falling dust grain of 1 m/s (Xu 1992), the dust grain needs only to fall 1.1 micrometers through the plasma before it reaches equilibrium charge.

The standard OML derivation assumes collisionless plasma; at the higher pressures achievable in the available machine, this assumption breaks down (see Section 5.3.3). OML has been adapted to account for this by Land et al. (2010) who employed the screening length and the ion mean free path to calculate the currents to the grain. For this case, the resulting electron current is

$$I_e = -4\pi r_p^2 e n_e \sqrt{\frac{k_B T_e}{2\pi m_e}} e^{e\phi/k_B T_e}, \quad (3.29)$$

while the ion current is

$$I_+ = 4\pi r_p^2 e n_+ \sqrt{\frac{e_+}{2m_+}} \left[1 - \frac{e\phi}{E_+} + 0.1 \left(\frac{e\phi}{E_+} \right)^2 \frac{\lambda_D}{l_{mfp}} \right], \quad (3.30)$$

where E_+ is the energy of an ion. The resulting charges produced by this method for all cases tested are larger than those produced using the basic OML model. An improved model, which is more complicated but more consistent since the ion drag calculations employed in this work are by the same authors (basic assumptions are the same), is also applied later (D'yachkov 2007). The expression for the ion current from this model is

$$I_+ = \frac{4\pi n_0 z \tau D_i e^{z\tau a/r_{0,i}}}{\sqrt{2\pi} z \tau a l_{mfp} \left[r_{0,i}^2 - l_{mfp} (a + r_{0,i}) e^{-\frac{z\tau a^2}{r_{0,i}(a+r_{0,i})}} \right]^{-1} + e^{z\tau a/r_{0,i}} - 1}, \quad (3.31)$$

and the electron current is

$$I_e = \frac{4\pi n_0 z a D_e}{\sqrt{2\pi} z e^z l_e / a + \exp(za/r_{0,e} - 1)}, \quad (3.32)$$

where D represents the diffusion coefficient found from the product of the respective thermal velocity with the mean free path, $z = e^2 Z_d / k T_e a$ is the normalized grain potential

(where Z_d is the grain charge in electrons), τ is the electron to ion temperature ratio, $l_{mfp(e)}$ is the mean free path for the ions (electrons), and $r_{0,i(e)}$ is the grain radius (a) added to $l_{mfp(e)}$ of the ions (electrons).

It is generally found in RF plasma machines that the electron temperature is about 100 times greater than the ion temperature (Fortov 2004); this ratio is typically labeled τ . The ion temperature is assumed to be approximately the ambient room temperature, i.e., about 25 meV, since the ions occasionally collide with the neutral gas particles, which are at equilibrium with the chamber walls. The electron temperature is much greater than this because electrons collide less often with the neutral gas (see Section 3.1.1) and the RF radiation introduced into the system primarily interacts with the electrons. Using the above parameters from the CASPER machine yields $\tau = 217$. This is often referred to as a non-equilibrium plasma.

When dust grains in space are examined, photoelectric emission must also be taken into account in the charging process. Ultraviolet light (> 10 eV) from stars causes the ejection of electrons and thus a reduction, if not a complete reversal, in charge magnitude. This is one process that is thought to aid dust coagulation to ultimately form new planets or stars (Ma 2013). Though this would be interesting to study in the laboratory, it would require high frequency (10^{15} Hz) lasers to reproduce.

Since electrons are lost to the walls and surfaces, small (local) plasma volumes may not be quasineutral as initially assumed for basic (global) plasma. The non-equilibrium status also contributes to this effect. This is reflected by significantly positive plasma potential with respect to ground and the walls. If the dust population is large enough, it may be enough to simply account for those lost electrons in the following manner,

$$n_i = n_e + Zn_d, \quad (3.33)$$

where n_d is the dust density, and Z is the dust charge in electrons. This effect is thought to influence ionization rates, which can have significant effects on dust grain structure, at least at significantly higher plasma power (100 W) (Samsonov 1999).

3.2.2 Forces on a Dust Grain

3.2.2.1 Gravity and Sheath Electric Field. Understanding that there is a charge on each dust grain opens the discussion as to quantification of the electric forces, but other forces exist as well. In the discussion below, these will be ordered by decreasing magnitude, and thus, importance for experimental consideration. The first order of business is to explain why dust grains levitate in the lower sheath of a GEC RF plasma cell. All matter experiences a gravitational force on the Earth's surface of approximately mg , where m is the mass and g is the gravitational constant 9.81 m/s^2 . For an 8.89 micrometer diameter solid melamine formaldehyde sphere, the gravitational force is $5.41 \times 10^{-12} \text{ N}$. As explained in the previous two sections, electrons collect on the surface of the dust grain. The electrons collected on the lower electrode also create an induced electric field (E) in the sheath, which is directed downward. The induced field repels charged dust grains with a force QE . Under the most basic approach, the height at which a single particle will levitate is assumed to be determined by $QE = mg$. Many experiments have confirmed the presence of a linear electric field where the dust levitates (Tomme 2000). Note that the particles only levitate in the lower sheath. This is because the electric field in the upper sheath points in the opposite direction, helping gravity to push the particles into the bulk, where they continue to charge as they fall toward the

lower sheath. A more detailed analysis has shown that the force from the electric field should be

$$F_e = ZeE \left[1 + \frac{(r_p/\lambda_D)^2}{3(1 + r_p/\lambda_D)} \right], \quad (3.34)$$

due to the presence of the charged dust grain which produces a polarization in the surrounding plasma, adding to the force. For the experimental conditions used for all previous calculations, the correction term in the brackets proves to be insignificant as it has a value of 6.5×10^{-12} .

3.2.2.2 Ion Drag. The next most important dust force is produced by the streaming ions. Since ions have substantial size and mass, ion drag can become significant under the appropriate conditions. Since the dust grains are charged, there are two basic types of ion drag represented by separate cross-sections. The first of these is the collection cross-section, which occurs when ions actually collide with the dust grain. The second is the Coulomb cross-section, which occurs as the ions flow past a dust grain, electrically attracting the grain. It is this attraction that is believed to create an ion wake-field (Miloch 2012) beneath a dust grain, where flowing ions converge to generate a more positive region. This positive region can provide an attractive force to particles beneath the grain as well as generate vertical alignment. The following is the total ion drag formula used throughout the present work (Khrapak 2005),

$$F_i = \sqrt{2\pi} r_p^2 n_i m_i v_{Ti}^2 \left\{ \frac{\sqrt{\pi}}{2} \operatorname{erf} \left(\frac{u}{\sqrt{2}} \right) (1 + u^2 + (1 - u^{-2})(1 + 2z\tau) + 4z^2\tau^2 u^{-2} \ln(\Lambda)) + u^{-1} (1 + 2z\tau + u^2 - 4z^2\tau^2 \ln(\Lambda)) \exp \left(-\frac{u^2}{2} \right) \right\}, \quad (3.35)$$

where u is the ion drift speed normalized to the Mach number, z is the dimensionless grain charge ($z = Ze^2/r_p \kappa T_e$, where Z is the charge in electrons), Λ is the exponential of the Coulomb logarithm (defined as $(z\tau r_p/\lambda_D u^2 + 1)/(z\tau r_p/\lambda_D u^2 + r_p/\lambda_D)$), and τ is the ratio of

electron to ion temperatures. The expressions in Eqn. 3.35 underlined in red represent the contribution from ion collection, while those underlined in blue represent contribution of ion scattering.

3.2.2.3 Interparticle Repulsion. Because monodisperse particles with high precision (+/- 0.01 micrometer) are used, all grains attempt to levitate at the same height. Since particles in a given layer are assumed to have the same charge, they repel each other through a shielded Coulomb (Yukawa) force,

$$F_y = \frac{Q^2}{4\pi\epsilon_0 x_d} \left(\frac{1}{x_d} + \frac{1}{\lambda_D} \right) e^{-x_d/\lambda_D}, \quad (3.36)$$

where x_d is the distance between two dust particles of equal charge Q , and can be found by taking the derivative of Eqn. 3.3. The horizontal confinement produced by the cutout placed on the lower electrode, initially assumed to provide a linear restoring force resulting from a parabolic confinement potential, keeps the particles from flowing off the lower electrode due to interparticle repulsion. When allowed, the particles levitate at the same height in a single layer. When too many particles are introduced into the system, they generally form multiple layers. Many bi-layer experiments have been conducted (Hartmann 2009). If even more dust is added, the grains may be pushed completely out of confinement.

3.2.2.4 Neutral Gas Drag. Neutral drag from the background Argon gas plays a significant role. There are three regimes that apply based on two parameters: the Knudsen number and the relative particle velocity. The Knudsen number is the ratio of the neutral gas mean free path to the particle radius. If it is much less than one, then the Stokes formula, $F_n = -6\pi\eta r_p u$, where η is the viscosity and u the relative velocity, may be

used. This is referred to as the hydrodynamic regime. In the present experiments, assuming conditions of 10 W system power, 100 mTorr background pressure, and 8.89 micrometer diameter particles, the Knudsen number is 96.2. Since it is much greater than one, the following formula applies,

$$F_n = -\frac{8\sqrt{2\pi}}{3}\gamma r_p^2 n_n T_n \frac{u}{v_T}, \quad (3.37)$$

where γ is a parameter that depends on the surface of the particle. It is applicable under the second condition that the relative velocity is much less than the thermal velocity, referred to as the free molecular regime. Since the neutral thermal velocity is essentially the same as the ion thermal velocity (347 m/s), the dust particles rarely exceed this speed. Therefore this formula applies for all present experiments. Eqn. 3.37 is often condensed to $F_n = -m_d v_{dn} u$, where v_{dn} is the momentum transfer frequency, emphasizing the linear proportionality to the relative velocity. If a particle moves much faster than the thermal velocity, then the neutral drag force is instead proportional to the relative velocity of the grain squared: $F_n = -\pi r_p^2 n_n m u^2$.

3.2.2.5 Thermophoretic. When there is a temperature gradient, a thermally induced force exists that is directed from the hot to the cold, and is known as thermophoresis.

This force has been found to be

$$F_{th} = -\frac{4r_p^2 \sqrt{2\pi}}{15v_{Tn}} \kappa_n \nabla T_n, \quad (3.38)$$

where κ_n is the thermal conductivity of the gas. Thermophoresis has been shown to be able to levitate dust under laboratory conditions (Fortov 2004).

3.2.2.6 Radiation Pressure. The final well-known force acting on the dust grains is delivered from radiation pressure. A large number of experiments have used lasers to

perturb dust particles in a group or individually. This technique is superior to changing the plasma parameters of the system, because plasma parameters affect many other values. The radiation pressure is given by (Liu 2003)

$$F_l = A \frac{n_r \pi r_p^2 I}{c}, \quad (3.39)$$

where A is a coefficient (ranging from 1 for complete absorption up to 2 for complete reflection from a flat disk), n_r is the coefficient of reflection of the medium, I is the intensity of the beam, and c is the speed of light.

3.2.3 Coulomb Crystals

Under appropriate conditions, a layer of dust particles will self-organize into a hexagonal lattice, also known as a Coulomb crystal because it is maintained by shielded Coulomb repulsion. This is primarily due to the fact that this structure minimizes the overall repulsive potential energy. This does not depend on the number of particles present, though once a layer is filled another will form. If the confinement and grain charge was known precisely, this could provide a measurement for the screening length. One of the ways to quantify the level of structure in a dust cloud is called the coupling parameter (Pieper 1996),

$$\Gamma = \frac{Z^2 e^2}{4\pi\epsilon_0 n^{-1/3} \kappa T}. \quad (3.40)$$

Using the same dust charge as above, at a plausible interparticle distance of 500 micrometers, with an average motion of 1 mm/s, yields a coupling parameter of $\Gamma = 2091$. Values much greater than one indicate the strong coupling regime, and this is generally the state in which these experiments exist. Above a critical value $\Gamma \approx 170$, a Coulomb lattice can form (Ikezi 1986). Another ratio (χ) often examined is that of the interparticle spacing to the Debye length. Three dimensional crystals in the form of face

center cubic (fcc) form at high ($\Gamma > 1000$) coupling parameter for $\chi > 2$, and body center cubic form for $\chi < 2$ (Fortov 2004). Level of crystallization has been also quantified with pair correlation functions and analysis of defects in the lattice through Voronoi diagrams. Other methods of study include mean square displacement, static structure factor, and the bond correlation function (Liu 2005). Structure between layers has been observed to form two different crystal structures under appropriate conditions.

3.3 Challenges

There are many challenges that exist when attempting to apply the above plasma basics to low temperature non-neutral, non-equilibrium dusty plasma. First of all, the Debye length is derived under the assumption of bulk conditions, where plasma species may be assumed to have a Maxwellian distribution. This is one reason the shielding effect is more often calculated using a “screening length” that is dependent on the speed of the streaming ions. Even these methods tend to use some combination of the electron and ion Debye lengths, neither of which accounts for an electric field that exists in the sheath. Second, OML theory is based on several assumptions that do not hold true under the circumstances at hand. DML has many of the same issues; for example, it accounts for streaming ions but does not incorporate the sheath electric field. Third, Langmuir probe measurements can only be taken in the bulk, and therefore must be extrapolated by employing models of the plasma at the dust location. Langmuir probe measurements are also more reliable in much higher density plasma.

Another major question involves the value of the Mach number for the streaming ions. Simulations have been run in both sub and supersonic cases; however, the derivation for the Bohm velocity assumes a collisionless plasma, so it may be possible

that ions exit the sheath at subsonic velocities. The continuity equation may also be invalid if ionization or recombination occurs in the sheath. One formula has been derived that yields the Mach number (Wörner 2012),

$$M = \sqrt{\frac{m_d g \lambda_m}{Z \kappa T_e}}, \quad (3.41)$$

resulting in a value of 0.27 (normalized to the Bohm velocity) using the ongoing parameters, plotted in Figure 13 for various charge models. Unfortunately this employs the mobility, which is only valid “when collisions with neutral atoms are dominant” (Chen 2006). At high pressures this should become more useful.

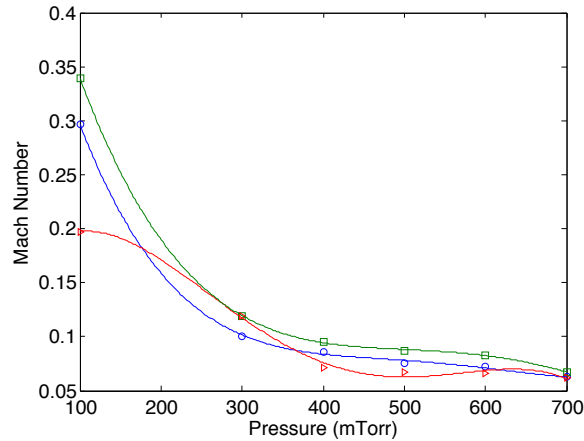


Figure 13 – Mach number predicted at the dust position as a function of the pressure, using OML to find the charge and Lieberman cross-section to find the ion mean free path. The blue circles represent the Mach number using basic OML with the bulk plasma parameters, the green squares using the plasma parameters at the dust (found by using the continuity and energy conservation equations with the experimental equilibrium dust levitation position), and the red triangles using the collisional OML model with the plasma parameter at the dust. However, a valid experimental test to measure the Mach number has not been developed.

The electric field in the sheath is usually estimated using the forces on dust particles. However, since both the dust charge and the electric field may change as a function of height, these two quantities are often inextricably linked. This requires independent experiments, but many researchers find conflicting results (for example a 9 micrometer

diameter grain was reported to have a charge of 3,400e at a background gas pressure of 13 Pa with plasma generation through an RF voltage of 36 V_{pp} (Pieper 1996) compared to a 12 micrometer diameter particle at 20 Pa in a plasma with RF voltage of 50 V_{pp} reported to have 50,000e (Douglass 2011)). So far, none have emerged as the front-runners.

Because these challenges require deep theoretical, numerical, and experimental solutions, this dissertation will not provide their complete solution. However, the work presented should provide a basis for future research.

CHAPTER FOUR

Experiment

4.1 Introduction

In this chapter, data for three experiments which all manipulate dust grains using a powered probe are reported. The differences between the experiments involve only the orientation of the probe and dust, but the underlying physics varies in each. In Section 4.2, a single particle is oscillated vertically, but asymmetrically, despite the application of a probe potential that is changed symmetrically over time. In Section 4.3, static probe potentials are used to produce and manipulate an empty circular region in the center of a two-dimensional horizontal dust crystal layer, and oscillated potentials are used to generate radial waves. In Section 4.4, one-dimensional vertical chains of dust grains are formed and then driven with an oscillating probe potential. In the following chapter, a deeper analysis of the underlying physical mechanisms is given.

4.2 Vertical Oscillation

Portions of this section have been previously published as: Harris, B. J., Matthews, L. S., and Hyde, T. W., *Phys. Rev. E* **87** (5), 053109 (2013).

The first experiment involves a far field interaction. Motivation to undergo this work was due to the observation that changing the probe bias and height independently produced and altered the size of a circular open region devoid of dust, henceforth referred to as a “cavity,” in the dust crystal. This will be further discussed in Section 4.3. In a previous experiment using a horizontal wire (Samsonov 2001), the primary force described to repel the dust in such a region was shown to originate due to the direct

electric field. This proves not to be the case here. In this section, the cavity formed is significantly larger than would be expected from calculation assuming a simple interaction between the probe and the dust through a shielded Coulomb potential. In order to examine the root of this behavior, the probe tip was positioned at the transition height, defined as the point of closest approach to the dust cloud before a cavity is opened within the crystal. The particle located immediately beneath the probe is then available for analysis. A side view showing the probe located at the transition height for a crystal at its equilibrium levitation height for the base configuration, as defined in Table 3, is shown in Figure 14. For this case, the operating conditions have been adjusted to allow a single particle to levitate directly beneath the probe. (These conditions also serve as inputs to the numerical model used to calculate the charge on the dust particle, as described later.) Once in place, the probe potential is then oscillated, and the resultant dust particle motion analyzed to determine the neutral drag coefficient of the background gas for an 8.89 micrometer diameter particle and the resonant frequency of the levitated grain.

Data sets consisting of 125 images taken at 125 frames per second were obtained for each of the parameters shown in Table 3. The italicized set of parameters (20 V probe bias, 55 V probe potential peak to peak, 1.0 W system power, 80 mTorr gas pressure, 7.3 mm probe height, 2.3 Hz oscillation frequency, and -5 V fixed DC bias) will henceforth be referred to as the base configuration. The choice of 2.3 Hz was based on results from another experiment, which will be described in Section 4.3. Isolation of effects occurred by modifying one parameter at a time in the experiment, with all others remaining the same as those established for the base configuration.

Table 3 – Experimental parameters used in this experiment. The italicized value for each parameter defines the base configuration, as discussed in the text.

Parameter	Settings
Probe Bias	10, <i>20</i> , 30 V
Probe Peak to Peak	45, <i>55</i> , 65 V
System Power	0.75, <i>1.00</i> , 1.50 W
Pressure	70, <i>80</i> , 90 mTorr
Probe Height	7.3, 9, 11 mm
Frequency	1, <i>2.3</i> , 5 Hz
DC Bias	-10, -5, -1 V

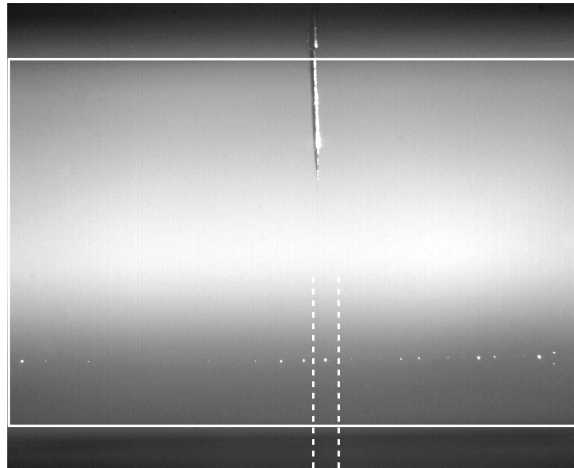


Figure 14 – Side view of the vertical oscillation experiment. For the ‘base configuration’ setup, the tip of the probe is located 7.3 mm above the dust equilibrium levitation height. Only the particle between the (dashed) bars is tracked, with the area in the box, which excludes the electrodes, used for calibration.

Images were analyzed employing both particle tracking (Sbalzarini 2005) and profile analysis (Abramoff 2004). Image calibration to facilitate reproducibility in future experiments was completed by subtracting the minimum intensity of the image set in the

region excluding the electrodes (indicated by the box in Figure 14) from all pixels before determining the position of the maximum intensity and sheath edge. To focus on the features of the plasma, the probe was removed from the image for profile analysis by copying the adjacent region.

The quantities best characterizing the oscillation are indicated in a representative image profile of the base configuration as shown in Figure 15a. Other bare profiles are also included for comparison. They are, in ascending vertical position, the particle levitation height, the sheath edge (defined as the position where the optical emission intensity decreases by a factor of Euler's constant from its maximum) (Beckers 2011), the location of the maximum derivative of the emission intensity in the lower sheath, and the point of emission maximum. Normalization is to the maximum signal acquired by the camera, and all images were taken at the same f-stop to allow comparison. The plasma intensity decreases most noticeably with a decrease in power (Figure 15b), but exhibits similar features over all parameters. Sinusoidal oscillation of the probe potential was found to yield non-sinusoidal changes in these four values, as shown in Figure 16 for all parameter settings differing from the base configuration, over two oscillation cycles.

The fact that the maximum emission intensity moves lower with an increase in power (compare Figure 16a with Figure 16c) is most likely due to cell geometry. The plasma exhibits an asymmetric vertical emission profile (averaged over the horizontal direction) as shown in Figure 15, due in part to the fact that the upper electrode is a hollow ring and grounded, whereas the lower electrode is a circular powered plate. Given the upper electrode has less surface area and is at a higher potential than the lower electrode, there will be less ion flux upon the upper electrode. Because the upper electrode is grounded,

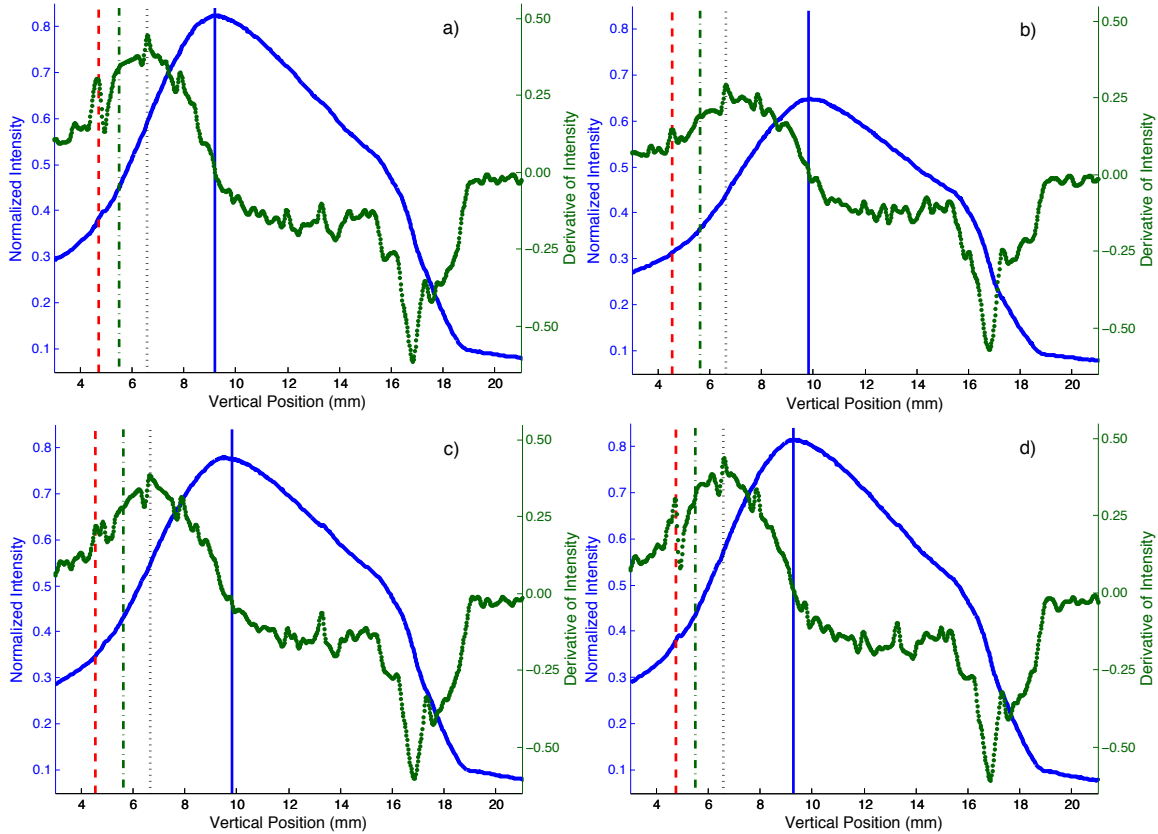


Figure 15 – Normalized optical emission intensity profile (solid blue line) of the plasma (Figure 14) averaged over the horizontal coordinate as a function of the distance above the lower electrode (where the upper electrode is located at $z=19$ mm). The derivative of the intensity (green dots) is superimposed with vertical lines indicating the levitation height of the dust (red dashed), the sheath edge (green dash-dot), the local maximum of the derivative emission intensity (dotted black), and the maximum of the intensity (solid blue). Plots are shown for a) base configuration, b) 0.75 W c) 70 mTorr, and d) 30 V probe bias.

the potential difference between the plasma and the upper electrode is smaller than that between the lower electrode and the plasma, so ions may move towards it more slowly. Raising the power increases the magnitude of the lower electrode dc bias, which accelerates the lower sheath ions to a higher Mach number, the net result being that the plasma ions on average decrease in height, with enough electrons quickly following to maintain quasineutrality. At higher powers, there is greater ionization, which would also contribute to the previously described effects.

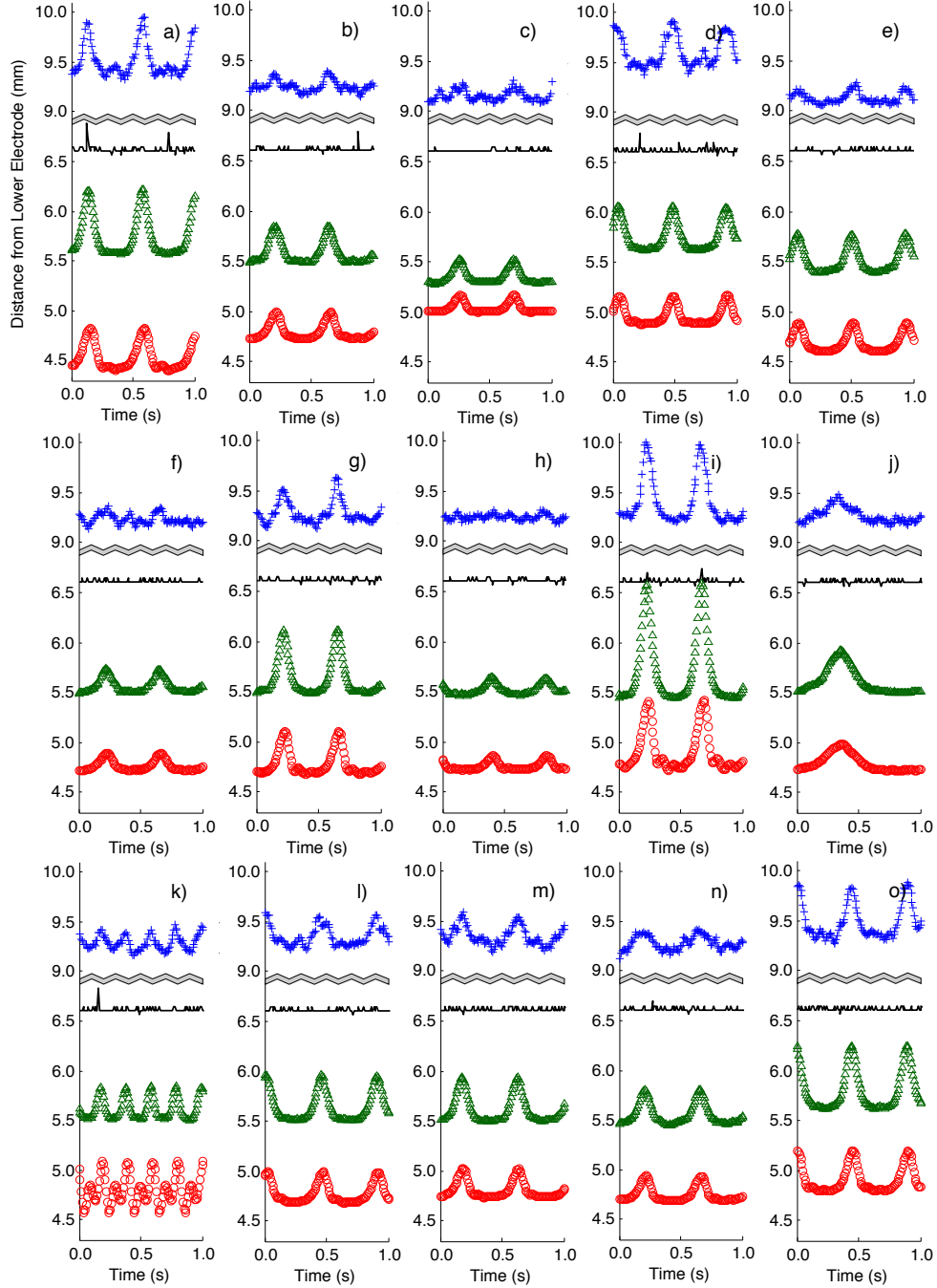


Figure 16 – Distance from the lower electrode versus time for: the particle height (red circles), the sheath edge (green triangles), the maximum of the derivative of the emission intensity (black line), and the maximum of the emission intensity (blue crosses), for the following conditions: a) 0.75 W system power, b) base configuration (1.00 W), c) 1.50 W, d) 70 mTorr, e) 90 mTorr, f) 45 V probe peak to peak (VPP), g) 65 VPP, h) 10 V probe bias, i) 30 V probe bias, j) 1 Hz oscillation k) 5 Hz oscillation, l) 9 mm probe height, m) 11 mm probe height, n) -1 V DC bias, and o) -10 V DC bias.

Several general trends can be seen in Figure 16. The response to all quantities reduces with an increase in power (Figure 16a-c). A noticeable shift in all heights except for the maximum of the derivative intensity occurs when either the probe potential (Figure 16d-e) or DC bias is adjusted (Figure 16n-o). The peak to peak oscillation amplitude (Figure 16f-g) impacts the amplitudes in the expected direction, but changing the probe bias (Figure 16h-i) by the same increment provokes a larger response. An expanded view of the 5 Hz oscillation frequency case (Figure 16k) can be found in Section 5.2.

Oscillation of the probe potential causes changes in the height of the emission intensity maximum. The amplitude of the resulting intensity maximum oscillation becomes significant at lower powers (Figure 16a), lower pressures (Figure 16d), higher probe peak to peak amplitude (Figure 16g), higher probe bias (Figure 16i), and more negative DC bias (Figure 16o). It is also more prone to noise than any other quantity.

Unexpectedly, it was found that the position of the local maximum of the derivative of the emission profile of the lower sheath remains constant over all parameters (Figure 16). As shown in Figure 15a, the local maximum is located at $z = 6.6$ mm, with a similar local minimum at $z = 16.8$ mm in the upper sheath. The peak which can be seen at $z = 4.7$ mm is due to the line of dust. This results in an alternative method for locating the position of the dust.

The location of the $1/e$ point, indicating the sheath edge (see Section 3.1.2), decreases with an increase in power while the particle levitation height increases (Figure 16a-c), both due to an increase in ionization of the plasma. Note that convergence of the sheath edge to the particle position occurs for no parameter adjustment other than increase in

power. Since the sheath edge is too close to significantly distinguish from particle levitation height for powers higher than 1.5 W, the usefulness of this method ends here. In general the motion of the sheath edge responds similarly to the dust motion, except in the 5 Hz oscillation frequency case (Figure 16k) where cycle superposition only occurs in the dust motion. A likely explanation for this is that the plasma reacts much faster than the dust.

The response of the dust to the probe oscillation can be approximated (Trottenberg 1995) by the steady-state response of a damped, forced harmonic oscillator, with amplitude given by

$$A(\omega) = \frac{F}{[(\omega_0^2 - \omega^2)^2 + 4\beta^2\omega^2]^{1/2}}, \quad (4.1)$$

where β is the damping coefficient, ω_0 is the resonant frequency, ω is the driving frequency, and F is the magnitude of the driving force divided by the mass of the dust particle. A plot of the dust particle amplitude versus frequency (Figure 17) shows good agreement with theory. At a pressure of 80 mTorr, the resulting fit parameters are $\beta = 9.7 \text{ s}^{-1}$, $\omega_0 = 65.0 \text{ rad/s}$ (10.3 Hz), and $F = 1.1 \text{ N/kg}$. These are comparable to the results reported in Zhang et al. (2010), where $\beta = 8 \text{ s}^{-1}$, and $\omega_0/2\pi = 13.2 \text{ Hz}$, measured at 66 mTorr. Because the fit in Figure 17 applies so well, the process that creates the non-sinusoidal particle response in time must not be sensitive to changes to frequencies in this range, and thus the only impact to Eqn. 4.1 occurs in F , related to the strength of the driving force.

The phase delay, which can be seen between the maxima of the sheath edge and the particle positions as shown in Figure 18, is well known for damped harmonic oscillation. For all cases here, it is found to be in the correct direction with particle response lagging

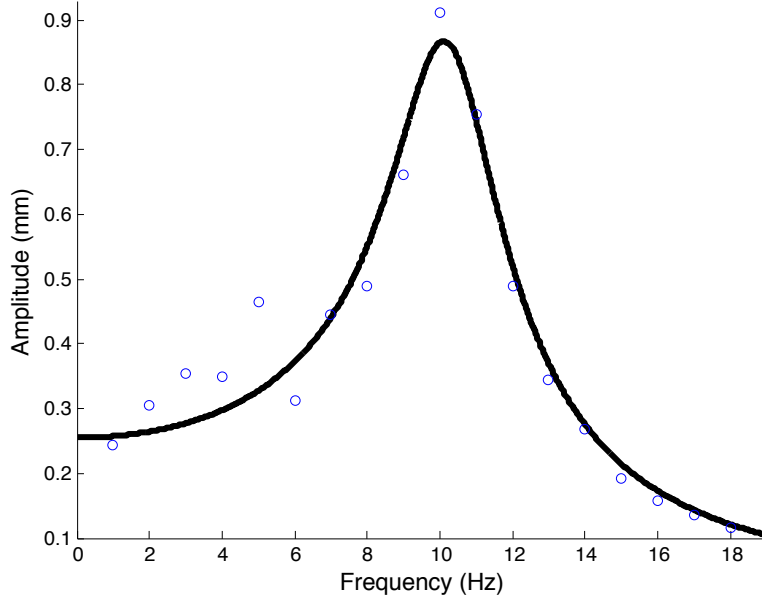


Figure 17 – Particle oscillation amplitude versus probe oscillation frequency. The fit shown is for a damped, forced harmonic oscillator, with amplitude determined as described in the text.

the driving force. While the probe potential oscillates sinusoidally, the location of the sheath edge does not, as seen in Figure 16. This implies that the force on the particle is not sinusoidal. Although a periodic, non-sinusoidal driving force will yield the same resonant frequency as that derived using Eqn. 4.1 (Fortov 2004), calculation of the phase shifts under different driving forces requires a numerical approach. The phase difference determined for this experiment for a sinusoidal force is given by

$$\delta = \tan^{-1} \left(\frac{2\omega\beta}{\omega_0^2 - \omega^2} \right) \quad (4.2)$$

and applied using the experimental phase shifts averaged over all peaks available for the oscillation frequencies processed (1.0, 2.3, and 5.0 Hz). Solving for the two remaining parameters (using the fit in Figure 18a) does not lead to a damping constant (12.7 s^{-1}) or resonant frequency (7.7 Hz) consistent with that found from the frequency sweep (Figure 17). Using Eqn. 4.2 to predict a phase difference for the base configuration yields a time

delay of 4.8 ms, 69% lower than the one found experimentally. Using the damping coefficient (7 s^{-1}) determined by Zhang et al. (2010) for 70 mTorr, the delay decreases to 3.5 ms. In Figure 19b the phase delay is shown to be 7.1 ms, still twice the predicted value. A similar deviation from experimental data as determined from the fit line at half the resonant frequency (shown in Figure 17) has also been seen in two other experiments. Ivlev et al. (2000) employed a powered wire placed below the particle layer and oriented horizontally (i.e., parallel) to the lower electrode to drive vertical dust oscillations. While the amplitude fit deviated from that expected for a damped harmonic oscillator above driving potentials of 50 mV peak to peak, a notable superharmonic response also appeared at driving potentials of 4 V peak to peak. Homann et al. (1999) examined particle response to lower electrode DC bias oscillations using square and sine waves, as shown in Figure 18b. A laser was also employed to perturb the particle without bias changes, which created a square wave force without sheath modification. A superharmonic response was found only when the force delivered to the dust was not sinusoidal. Therefore the discrepancy in the phase shift and the superharmonic peak are two results confirming the force acting on the particle is not sinusoidal and indicating that changes in the plasma are driving the particle's motion, rather than the sinusoidal driving potential of the probe.

Another feature of note that can be seen from Figure 19, which is not predicted by the damped harmonic oscillator model, is the marked decrease in time required for the dust particle to fall (51 ms from its maximum height at 4.99 mm to a height of 4.84 mm) compared to its rise time (74 ms over same distance in reverse). It is interesting to note that the sheath edge line is much more symmetric than that shown by the particle motion.

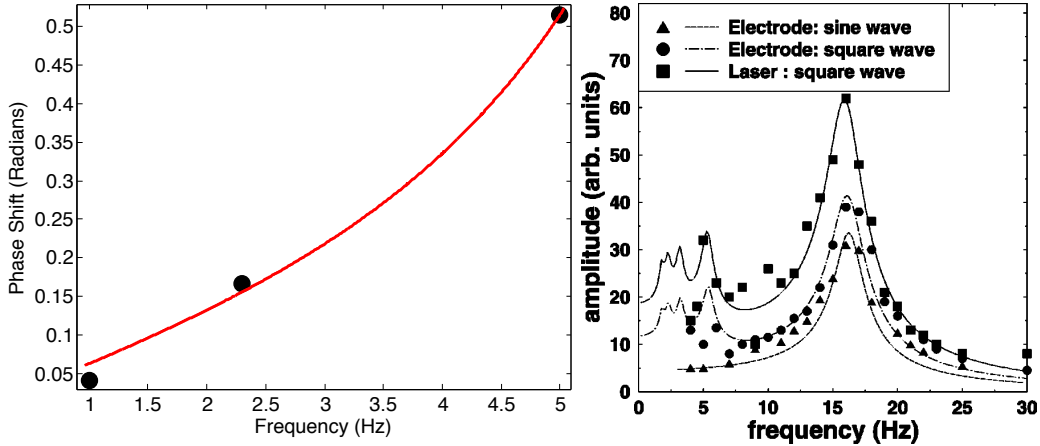


Figure 18 – A fit to the standard phase difference (left) of the damped, forced harmonic oscillator (Eqn. 4.2) yields parameters that do not match the experimentally measured phase difference. Figure 3 from Homann (1999) (right), shows the presence of superharmonic resonance at half the resonant frequency only for non-sinusoidal driving functions, whether or not sheath modification is used to generate the oscillation. Note that the same superharmonic resonance can be seen in Figure 17.

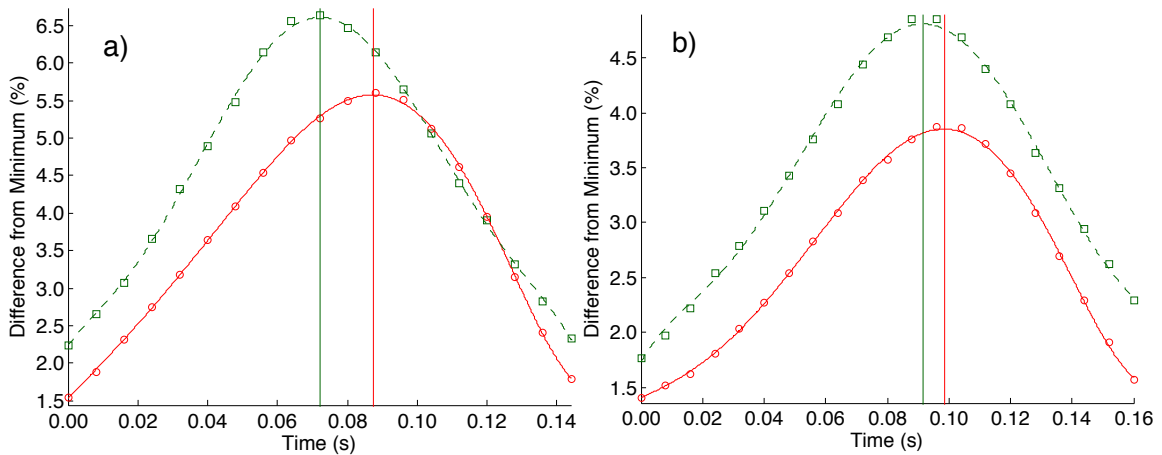


Figure 19 – Expanded view of the base configuration (Fig. 5b). The solid (red) line represents a polynomial fit to particle position (red circles) over time while the dashed line represents the fit to the sheath position (green squares). The vertical lines shown indicate the peaks of these fit lines illustrating the delay between maximum particle response and maximum sheath response. All values are shown as percentage differences from their respective minima for a) the base configuration, and for b) a pressure of 70 mTorr. The delay for a) is 15.0 ms, and b) 7.1 ms; delays of similar magnitude were found for other experimental parameters, but always in the same direction.

This is due to the fact that the dust particle is much more affected by gravity (because of its mass) and streaming ions (because of its size), both of which are directed downward,

than are the plasma species located at the sheath edge. In other words, if the force moving the dust particle is symmetric, both gravity and ion drag will resist its upward motion, supplementing restoration to equilibrium. Given that the ion drag force is much smaller than gravity, the signal to noise ratio in any model employed to separate the two would be very small. If the streaming ions moved in a direction not parallel to gravity, or their drag force was much stronger than gravity, this would provide a new mechanism for measuring the Mach number. However, since gravity is necessary for levitation of the particles, there is no immediate way to confine particles in a sheath where the ions would move in another direction (short of rotating the machine). Though the ion drag force has the advantage in that it depends on the relative velocity between the particle and the ions, the speed of the ions is vastly larger than any velocity a dust particle can achieve, so any experimental changes available are again too small to be of use. With large enough ion drag, particles could theoretically be levitated in the upper sheath, where the ion drag force would counteract gravity and the electric field, though this has not yet been reported.

Changes in the plasma can be characterized through measurement of the plasma intensity as shown in Figure 20, which displays the evolution of the plasma intensity over time. The vertical position where change in intensity is most pronounced is in the plasma bulk. A decrease in plasma glow will result from a reduction in electron density, which in turn results in a reduction of the total number of argon electron transitions. This argument is strengthened by the fact that such a reduction occurs primarily when the potential on the probe is above the plasma potential of 39.5 V. When the probe reaches its maximum positive potential, the bulk plasma intensity decreases by up to 9% for the

base and 14% for the 65 V_{PP} configurations, as shown in Figure 21. The glow responds faster than the particle, providing an indicator for the force on the particle. This presents a link to the particle delay (Figure 19) without having to independently match the probe potential to the oscillation. It also provides an advantage over using a nanoparticle equilibrium levitation position as a determiner of the sheath edge; without the danger of interparticle interaction, the sheath edge can be monitored simultaneously with the particle of interest. Fixed positive probe potentials corresponded to the dust crystal height being visibly raised as a whole, and the height of the maximum optical emission intensity from the plasma shifted upward as well. Note that the sheath adjacent to the lower electrode exhibits a greater intensity over a larger distance than does the sheath adjacent to the upper electrode, due to the asymmetry of the electrodes as discussed previously with the intensity profile analysis. At higher probe peak to peak values (Figure 20b), not only is the decrease in optical emission upon highly positive probe potentials more significant (as expected), but when the probe is negatively biased the plasma bulk is thicker. The latter effect is most likely due to the increased speed of the electrons at higher probe potentials, which stimulates more interactions with the argon ions.

The dust oscillation amplitudes for the parameters tested are shown in Figure 22. The amplitude of the sheath oscillation shown is larger than that observed for the particle oscillation. This implies the particle is not simply entrained in (or locked into) the plasma, but that its reduced amplitude is due to its mass (resisting sudden change through inertia), cross-sectional area (motion impeded by colliding neutral gas atoms and ions),

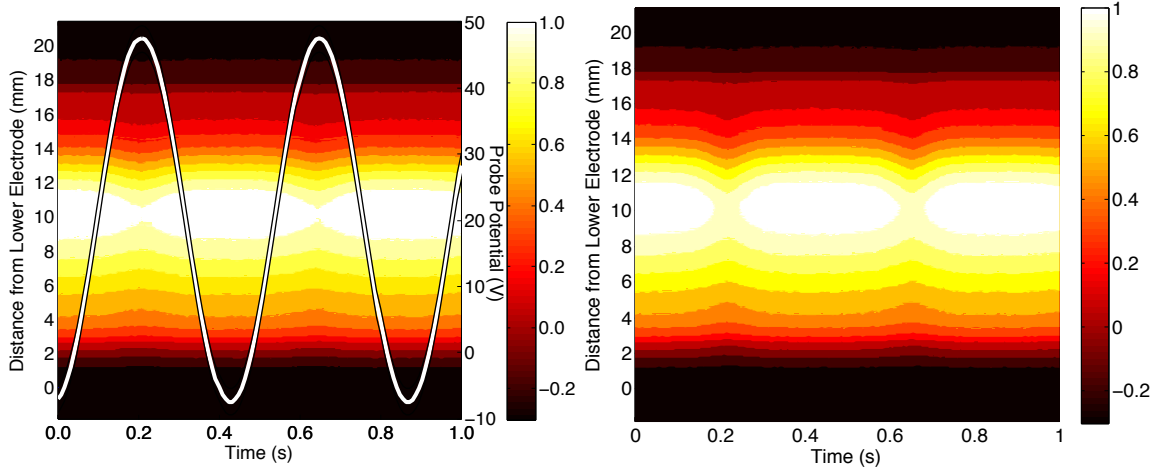


Figure 20 – Intensity space-time contour plot for the base configuration (left) and for the probe at 65 V_{PP} (right). The colorbar gives the intensity relative to the overall minimum, and normalized to the resulting maximum $((I - I_{\min})/I_{\max})$. The sinusoidal probe potential is superimposed in a).

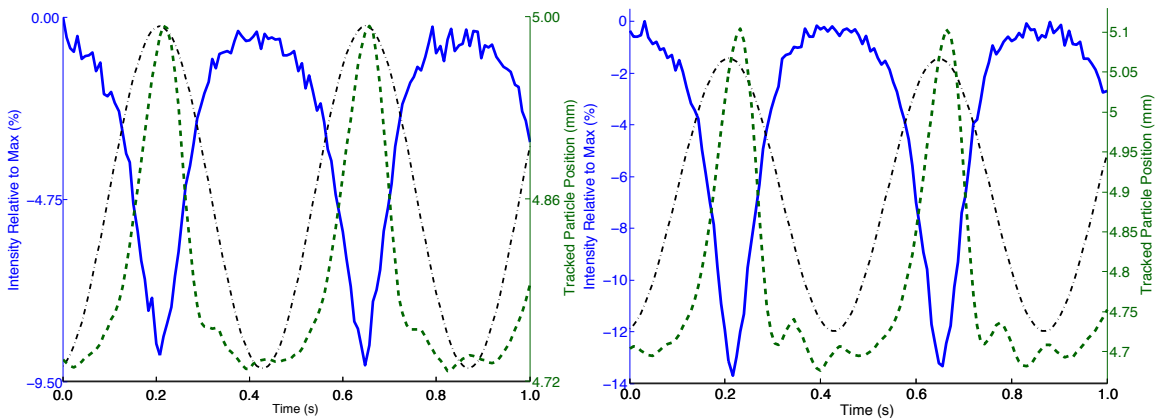


Figure 21 - Maximum intensity percentage change over time for the base configuration (left) and the 65 V_{PP} (right) case (solid blue line), superimposed with tracked particle data (dashed green line) and probe potential (dash-dot black line with the relative amplitude between plots scaled to represent each V_{PP} appropriately), which is scaled to the maximum particle position. Note that the percentage increase in particle amplitude is larger for 65 V_{PP} than the percentage increase in V_{PP}. As will be seen later, this is because the time spent above the plasma potential plays a primary role in generating this oscillation.

charge (Coulomb collisions with the streaming ions), and the structure of the sheath electric field. While any increase in probe bias generates a quadratic increase in oscillation amplitude (Figure 22a), an increase in the peak to peak oscillation voltage

results in a nearly linear increase (Figure 22b). On the other hand, increasing the RF power causes a decrease in oscillation amplitude (Figure 22c) due to ionization increase and electron temperature decrease (as found by Langmuir probe measurements), both of which increase the overall shielding by decreasing the Debye length. Therefore, a reduced perturbation is applied to the plasma, resulting in smaller particle amplitude. At the same time, changing the pressure and probe height do not appreciably affect the oscillation amplitude (Figure 22d and e). As the probe oscillation frequency approaches 5 Hz, the particle no longer has adequate relaxation time between cycles, and the maximum particle amplitude increases due to superposition (Figure 22f). Decreasing the DC bias on the lower electrode (Figure 22g) increases the potential difference between the plasma and the electrode, raising the particle within the sheath region, and resulting in a nonlinear increase in particle amplitude. Taken together, these results indicate once again that the probe locally modifies the plasma, which in turn drives the oscillation of the particle, as supported by the phase delay shown in Figure 19.

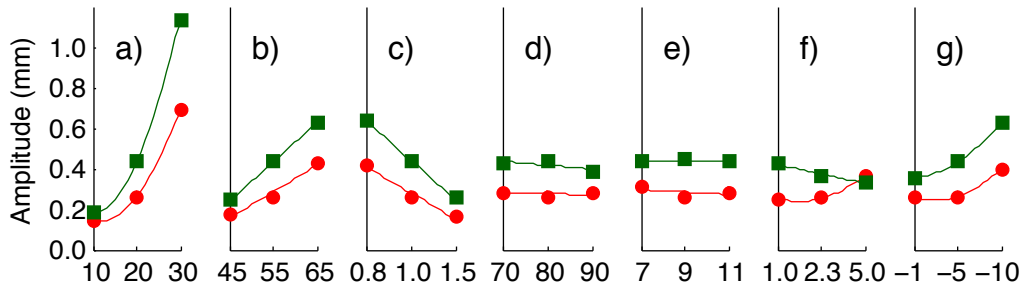


Figure 22 – Oscillation amplitudes for the sheath edge (green squares) and the particle (red circles) with quadratic or linear fits shown for variation in the individual parameters given in Table I. a) Probe bias (V), b) probe V_{pp} , c) system power (W), d) pressure (mTorr), e) probe height (mm), f) frequency (Hz), g) DC bias (V). Error bars are smaller than the marker size.

4.3 Dust Cavities

4.3.1 Introduction

As mentioned in Section 4.2, positioning the probe closer to the dust plane produces and/or increases the size of a cylindrically symmetric region (cavity) devoid of dust. There are three fundamentally different ways of creating a cavity or increasing the cavity size. First, placing a negative potential on the probe so that it repels the negative dust creates a cavity. Second, removing the probe altogether and adjusting the operating plasma parameters can form “natural” cavities. Third, after the probe reaches its floating potential, further increasing the probe potential can also increase the size of the cavity.

The term “cavity” is used here to clearly distinguish this phenomenon from the evacuated dust regions known as voids observed routinely in microgravity complex plasma experiments. Examples include the PKE-Nefedov experiments run on the International Space Station (ISS) and additional experiments conducted on reduced gravity aircraft (Figure 23). Voids have been explained as (and modeled assuming) a balance of an outward ion drag and an inward electric field force. They are naturally three-dimensional and occur in the plasma bulk. As shown in Figure 24, ion densities increase in voids in plasmas with increase in plasma RF amplitude, and the void radius exhibits an asymptote. It has also been shown (Figure 25) that the particle density distribution for voids observed under microgravity conditions reaches a maximum near the inner edge of the void and decreases with increasing radius.

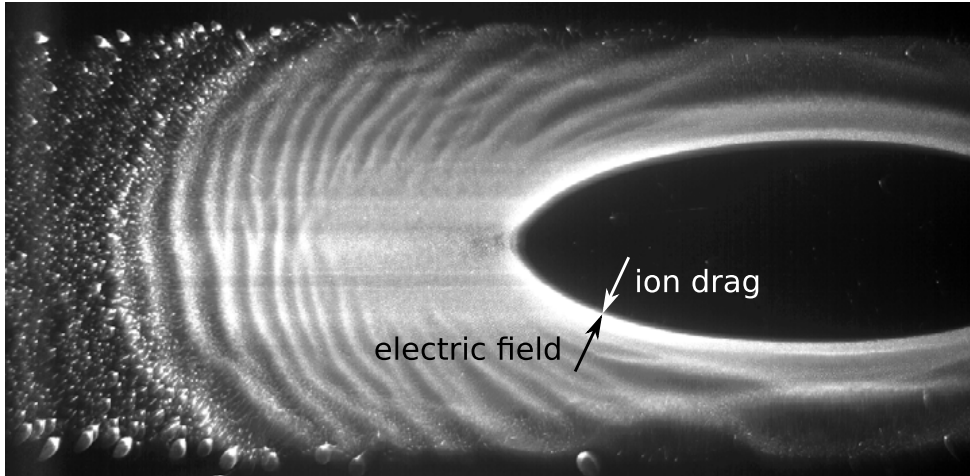


Figure 23 – Natural dust voids occur in the plasma bulk when a majority of the gravitational force pushing the dust into the sheath is absent. Although this void was found using simulated microgravity conditions produced within a descending airplane, similar voids have been created on the ISS (Buttenschön 2011).

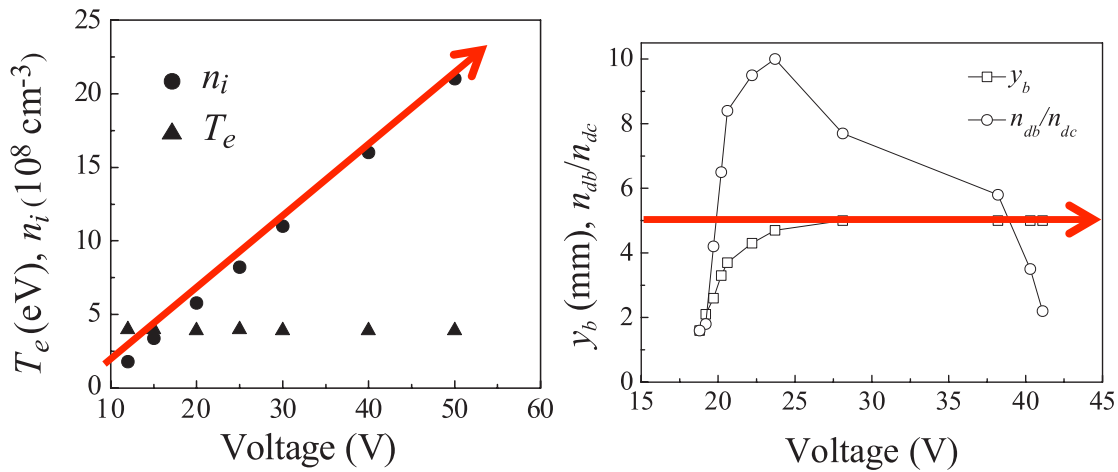


Figure 24 – Plots from ISS voids showing a linear ion density increase (left) and void size asymptote (right) with RF voltage increase (Lipaev 2007). Arrows have been added to note that both the ion density increases and the inner void diameter reaches an asymptote with increasing RF voltage.

4.3.2 Negative-Probe-Potential Induced Cavities

Beginning with a negative-probe-potential induced cavity, the potential on the probe was varied from -55 V to 0 V with respect to ground, at system powers of 1, 5, and 10 W, and gas pressures of 50, 100, and 300 mTorr. Representative cavity images for the 10 W,

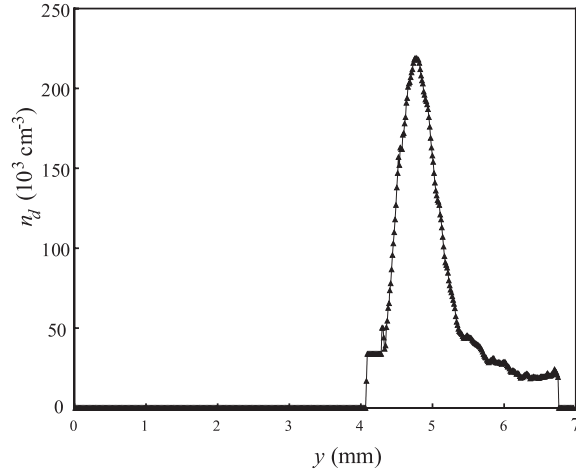


Figure 25 – Data collected on the ISS showing dust density as a function of distance from the center of the void. Note that the density quickly reaches a maximum, then decreases (Lipaev 2007).

100 mTorr case are shown in Figure 26. Surface plots of the inner radius of the cavity for all parameters are shown in Figure 27. As shown, radial progression is essentially linear with respect to probe potential. Lower pressures provide a much greater range of cavity sizes, while higher pressures start with much higher cavity sizes. Higher powers shrink the initial size of a cavity, whereas lower powers significantly reduce the overall range of cavity size.

4.3.2 Natural Cavities

Natural cavities occur when the system pressure is increased at higher system powers, as shown in Figure 28 for 10 W, and when the power is increased at higher system pressures, as shown in Figure 29 for 750 mTorr. This qualitative effect was also seen by Gabriela Paeva (2005), as shown in Figure 28. The greatest change in the slope obtained from the cavity size over pressure in the present experiment occurs around 200-250 mTorr (25-33 Pa), whereas the bend in Paeva's data occurs at a slightly lower pressure of

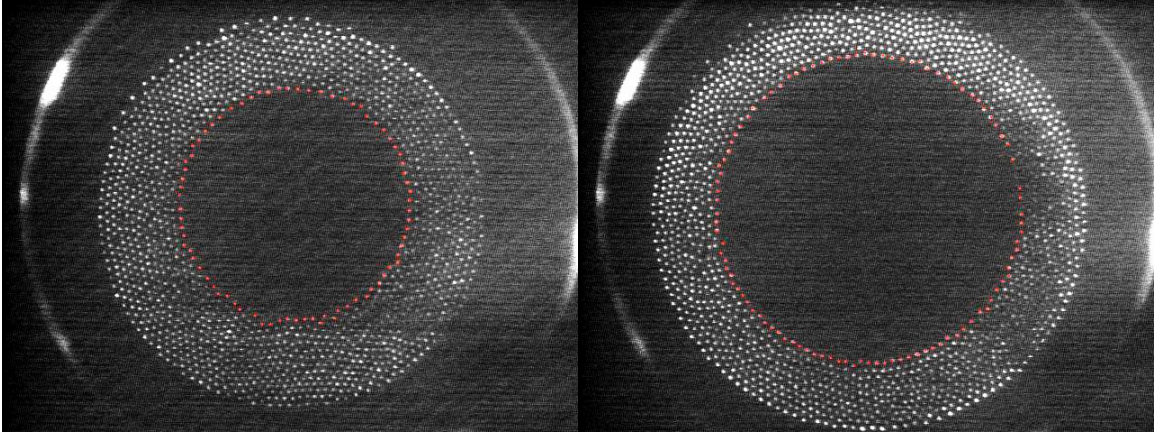


Figure 26 – Cavities induced by negative probe potentials ranging from 0 (left) to -55 V (right) with respect to ground (the potential of the upper electrode and walls), ordered from left to right. The intermediate images in increments of -5 V may be found in Appendix A. These were formed from Coulomb crystals within a plasma at a system power of 10 W and a gas pressure of 100 mTorr. Inner ring particles are colored red, while the outer circle that can be seen is the edge of the lower electrode cutout depression.

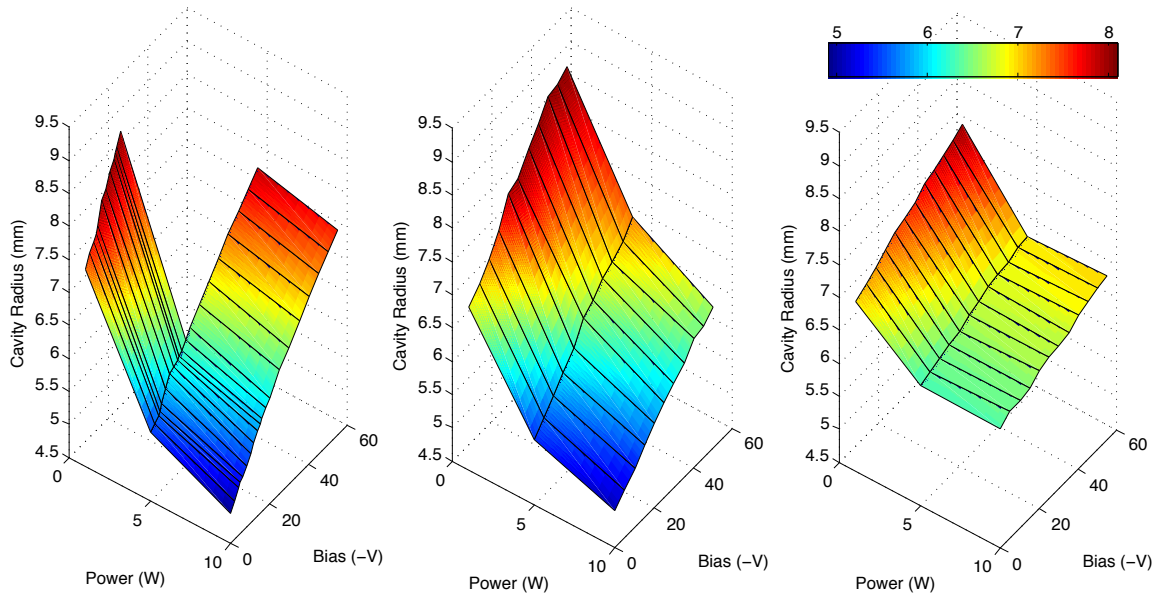


Figure 27 – Inner negative probe potential induced cavity radii over all parameters tested, at pressures of 50 mTorr (left), 100 mTorr (middle), and 300 mTorr (right). The premature end to the data in the 50 mTorr case is due to the fact that the plasma can not be lit in this parameter range. The colors show the cavity size in mm according to the colorbar.

approximately 22 Pa. The fits shown in Figure 28 are for shifted functions of the square root of the pressure, and follow the data well. Note that this is also seen in voids formed

in microgravity (Figure 24), suggesting that a similar formation process is at work. Because Paeva used a circular lower electrode with a 3 mm depression, this was also tested in our machine (red triangles), with the cavity size found to be essentially the same as that for the 1 mm lower electrode depression. As such, the difference between Paeva's data and the data here is likely due to differences in the electrode separation, since Paeva used the upper chamber wall as the grounded electrode. Even so, the similarity of sizes warrants the hypothesis that the same mechanism is at play in both experiments.

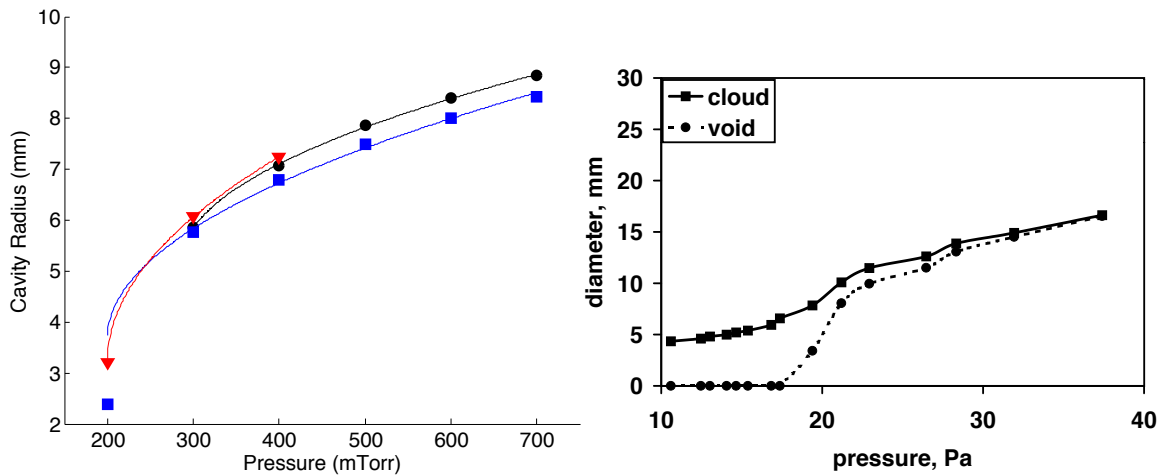


Figure 28 – Plot of natural cavity radius versus pressure for 10 W system power (left). The (blue) squares and (black) circles represent cavities formed using a 1 mm lower electrode cutout, for a natural bias and fixed DC bias of -50 V, respectively. Using the fixed bias prevented plasma ignition at 200 mTorr. The (red) triangles are for cavities formed using a 3 mm lower electrode cutout, as used by Paeva (right).

Natural cavities also occur when the system power is increased at fixed pressure (Figure 29). Here a direct comparison between parameters when using the deeper cutout was not possible, since for pressures greater than 350 mTorr the 3 mm cutout allowed the dust to fall below the surface of the electrode outside the cutout, preventing illumination by the horizontal laser. Nevertheless, an asymptote can be seen as in Figure 24. In Figure 29, lines still show shifted power fits ($r \propto P^\gamma$), but γ is less than $\frac{1}{2}$. As can be

seen, there is less similarity to Paeva's data, as the amplifier used here was limited the plasma power to 15 W, whereas the amplifier used by Paeva could achieve 60 W. Paeva also ran at the significantly lower pressure of 19.5 Pa (146 mTorr). This may account for the smaller cavity sizes seen (plotted by diameter), and the fact that data for the cavities shown here increase with increased pressures. In order to verify this, additional data should be obtained at lower pressures to match the 3-mm depression parameters and provide a more complete comparison.

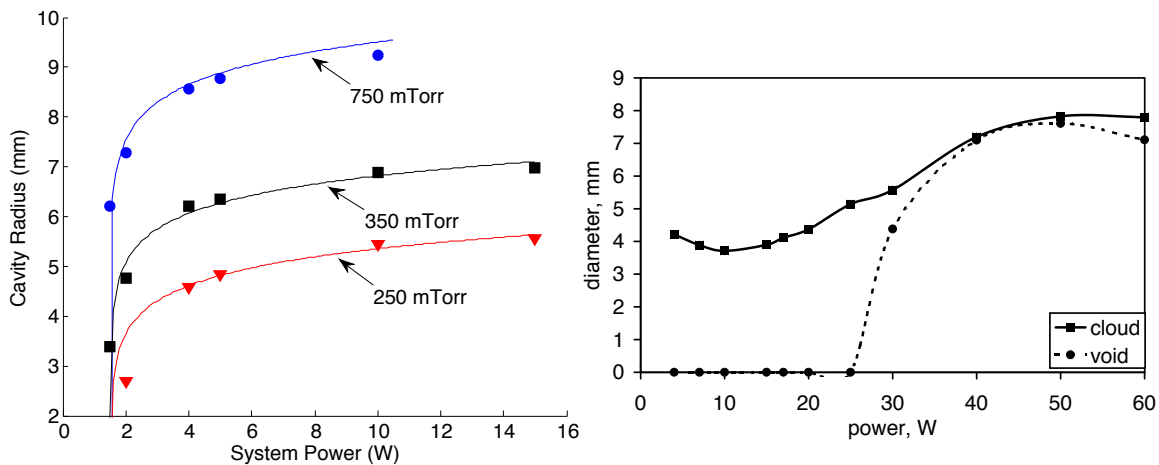


Figure 29 – Natural cavity radius versus system power for various fixed pressures (left). The (blue) circles represent cavities found using the 1 mm lower electrode cutout depression at 750 mTorr, whereas the (black) squares and (red) triangles represent cavities found using the 3 mm electrode cutout depression, at 350 mTorr and 250 mTorr, respectively. The diameter of dust cloud and cavity measured by Paeva with a 3 mm cutout is shown on the right.

4.3.4 Positive Probe Potential Induced Cavities

Over the course of this experiment, an unexpected effect never previously observed was discovered. A positively charged probe (relative to the dust) generated an increase in cavity size as potential increased. A plot of cavity size over the complete range of probe potentials (including data from Section 4.3.2) is shown in Figure 30. The dust cavity continues to shrink for potentials above 0 V, but begins to grow for potentials above the

dust floating potential (10 V). This growth mechanism must be quite different from those found for negative probe-induced cavities, if only due to the fact that the polarity change reverses the effect. The difference in mass between the electrons and ions implies this reversal mechanism must not be symmetric, even though the current varies linearly with the probe bias in both regions. Potentials above 55 V with respect to ground generated arcing, which prevented the measurement of cavity sizes that approach an asymptote with respect to probe bias.

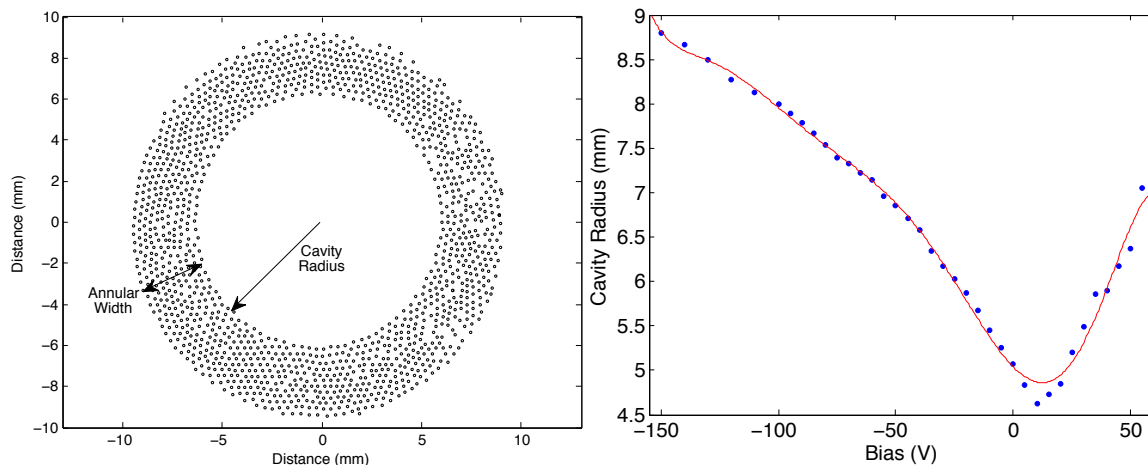


Figure 30 – Cavity radius (left) as a function of probe bias (right) with respect to system ground at 10 W system power and 100 mTorr chamber pressure. The cavity increases in size with decreasing negative probe bias, as discussed previously, but also increases in size with increasing positive probe bias for cavities formed above 10 V. A high order polynomial fit has been added to discern the general trend and local deviation in the data.

4.3.5 Cavity Lattice Waves

Wave motion found throughout physics can be used to gain information about the energy transfer medium, and this includes complex plasma. By oscillating the probe potential in the presence of a dust lattice, dust lattice waves (DLW) can be generated. Adjustments were made to the experimental setup to enhance the ability to observe the

DLWs, including using a lower electrode cutout with a 2-inch diameter, in order to form a larger crystal, and positioning the probe off to one side (see Figure 31).

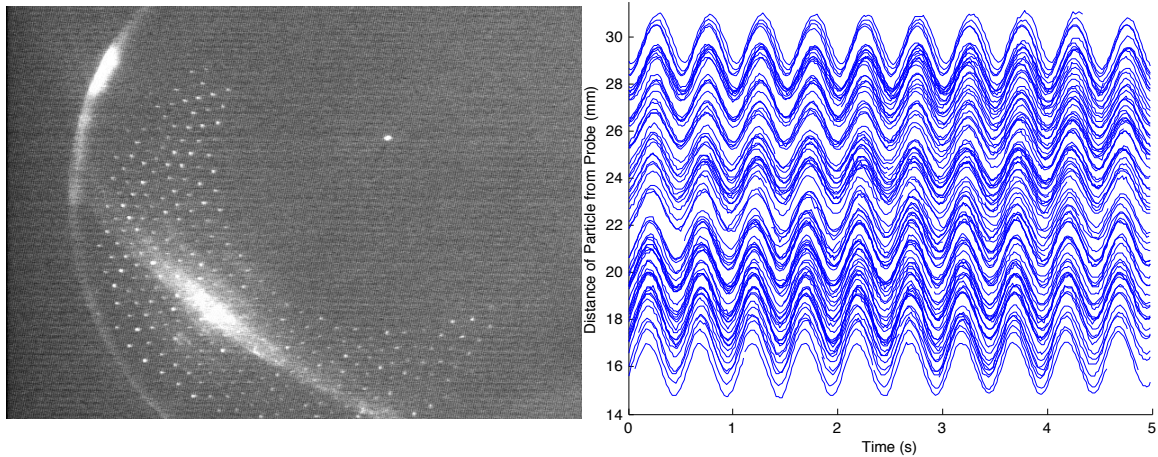


Figure 31 – Radial waves generated by oscillating the potential on a probe (spot at cavity center) held at a positive bias. The dust crystal exhibits a cavity (as found in Section 4.3.4) (left), and the resulting change in cavity radius drives the wave through the particles. Tracked particle positions are shown (right) for trajectories detected in at least 50 consecutive images.

It was found that these waves were able to propagate all the way through the dust lattice to the outer edge only when the probe bias oscillated at positive potentials. (This phenomenon led to the work described in Section 4.2.) The greatest amplitude and longest propagating waves were found at lower pressures, as expected since the neutral damping is decreased. Figure 31 shows the radial crystal and resulting wave motion for a system pressure of 55 mTorr.

Fine-tuning of the wave generation parameters identified conditions for which a minimum in the amplitude of the dust motion occurred at a fixed radial distance from the probe. This occurred at a point inside the crystal where particles on either side moved in opposite directions simultaneously. Because the presence of a node denotes a standing wave, this effect will be referred to as radial resonance. The largest amplitude lattice

waves were produced at a frequency of 2.3 Hz, providing the initial frequency choice in Section 4.2.

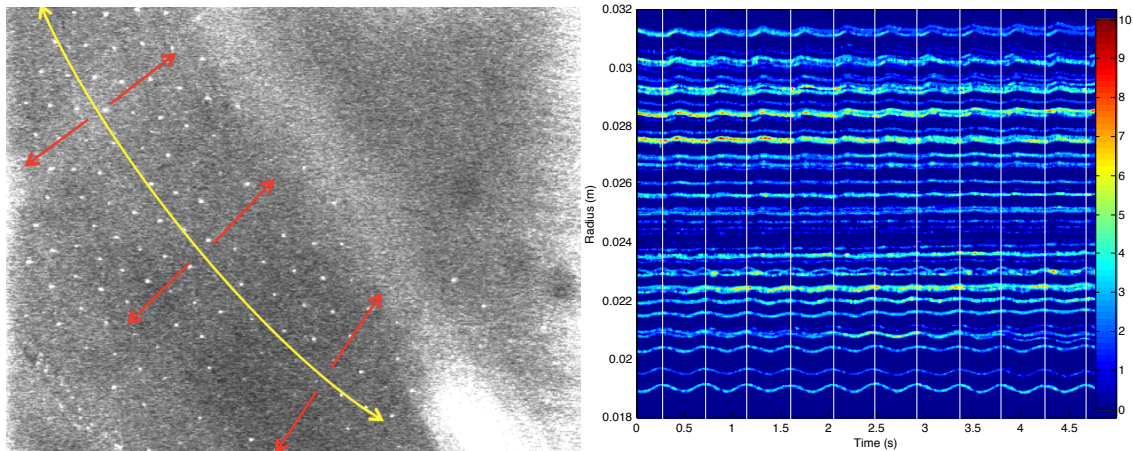


Figure 32 – Under conditions sensitive to small changes, a radial resonance effect can be generated. In this case, dust near the center of the crystal exhibits low amplitude oscillation, and dust on both sides show larger amplitude oscillation. In addition, the motion of dust on either side of the line is out of phase (left). The low central amplitude is shown in a space-time diagram (right), where the profile intensity has been averaged radially as a function of the distance from the probe, and plotted over time. Vertical lines are drawn once per cycle to indicate the change in phase as a function of the radius.

4.4 Dust Chain Waves

4.4.1 Introduction

Placing a glass box on the lower electrode provides additional horizontal and vertical confinement that can be exploited to create chains of dust particles. Impulses delivered to these chains can produce both longitudinal and transverse dust lattice waves (DLW). Particles exhibit coupled oscillator motion, exhibiting all of the longitudinal normal modes under different plasma conditions. Applying a square wave potential and fitting the particle motion decay to a damped harmonic oscillator, the damping coefficient and resonant frequencies can be found for both the longitudinal and transverse directions.

4.4.2 Longitudinal Dust Chain Waves

To create longitudinal dust chain waves, the probe is positioned directly above the dust chain (Figure 33) and its potential is oscillated. Employing this technique, experimental longitudinal dust chain waves can be generated which have characteristics which are well-modeled by coupled oscillators. All longitudinal wave modes predicted by such a model for a three-particle chain can be seen experimentally.

The general equation of motion for coupled oscillators is

$$-M\omega^2 a_j + \kappa_j(a_j - a_{j+1}) - \kappa_{j-1}(a_{j-1} - a_j) = 0 \quad (4.3)$$

where κ_j are the spring constants, ω is the frequency of oscillation, and a_j are the mode amplitude coefficients. Each of these can be experimentally determined and then applied in the simulation. For example, the spring constants are inversely proportional to the inter-particle equilibrium distances, not required to be equal, and can be determined from the equilibrium distances found from the particles in the experiment. However, many approximations for equidistant particles are not valid here since the grains are not necessarily equally spaced and this makes the analytical solution complicated. Additionally, the full system of equations, with the number of equations equal to the number of particles in the chain, must be solved simultaneously. A numerical simulation may be used, assuming the dust chain to be a series of coupled oscillators and then solving the system of equations assuming periodicity in each particle's motion to find the eigenvalues/eigenvectors.

Figure 34 displays the experimental data for both the longitudinal dust chain waves, and the data resulting from simulation. The constant of proportionality (A) in the spring

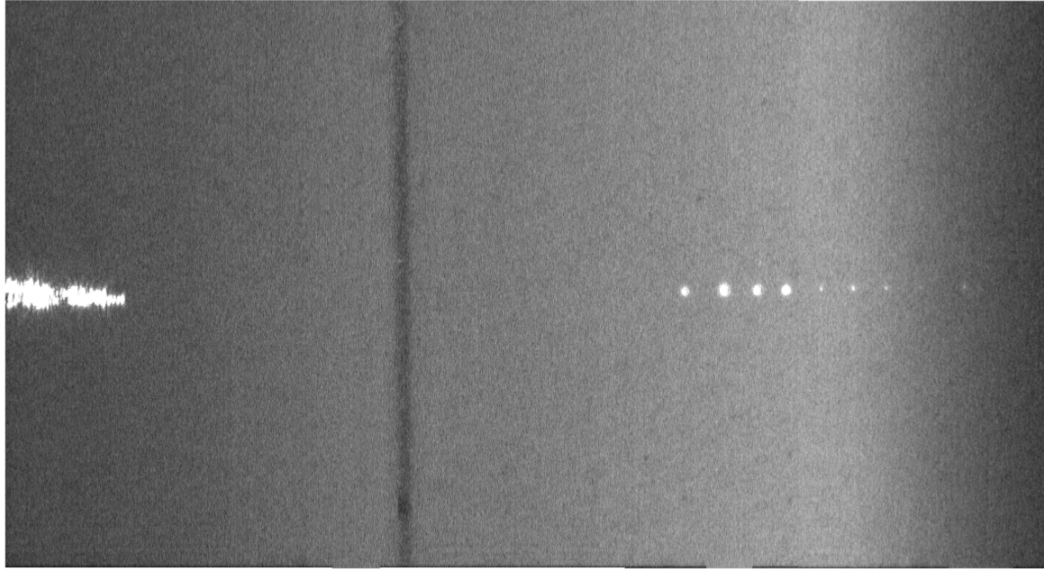


Figure 33 – The experimental setup required to produce longitudinal waves in a dust chain, where the image has been rotated so that the vertical upwards direction is to the left. A vertical probe attached to the S100 is positioned in line with the dust chain. The upper edge of the glass box, used to confine the dust vertically, is observed as a dark vertical band.

constants ($\kappa_j = A/d_j$) is the same for all spring constants of a particular mode, and is determined to be 2.6×10^{-10} N for both the standing (central particle stationary) and antisymmetric (central particle out of phase) modes, and 3.1×10^{-9} N for the symmetric mode (all particles moving in same direction). The standing mode is found at 6 Hz and 43 mTorr, the antisymmetric mode at 9 Hz and 150 mTorr, and the symmetric mode at 9 Hz and 80 mTorr. Each mode was only observed at the given parameters. The model requires the amplitude of one particle as an input; therefore, one particle's experimental amplitude was used. This implies that the amplitudes of the other particles in the simulation are a test on the model, and they agree quite well. For example, the antisymmetric mode simulation accurately predicts that the central particle will have the greatest amplitude of motion, because equidistant outer masses sit askew (away) from the theoretical antinodes (see first circle in Figure 34).

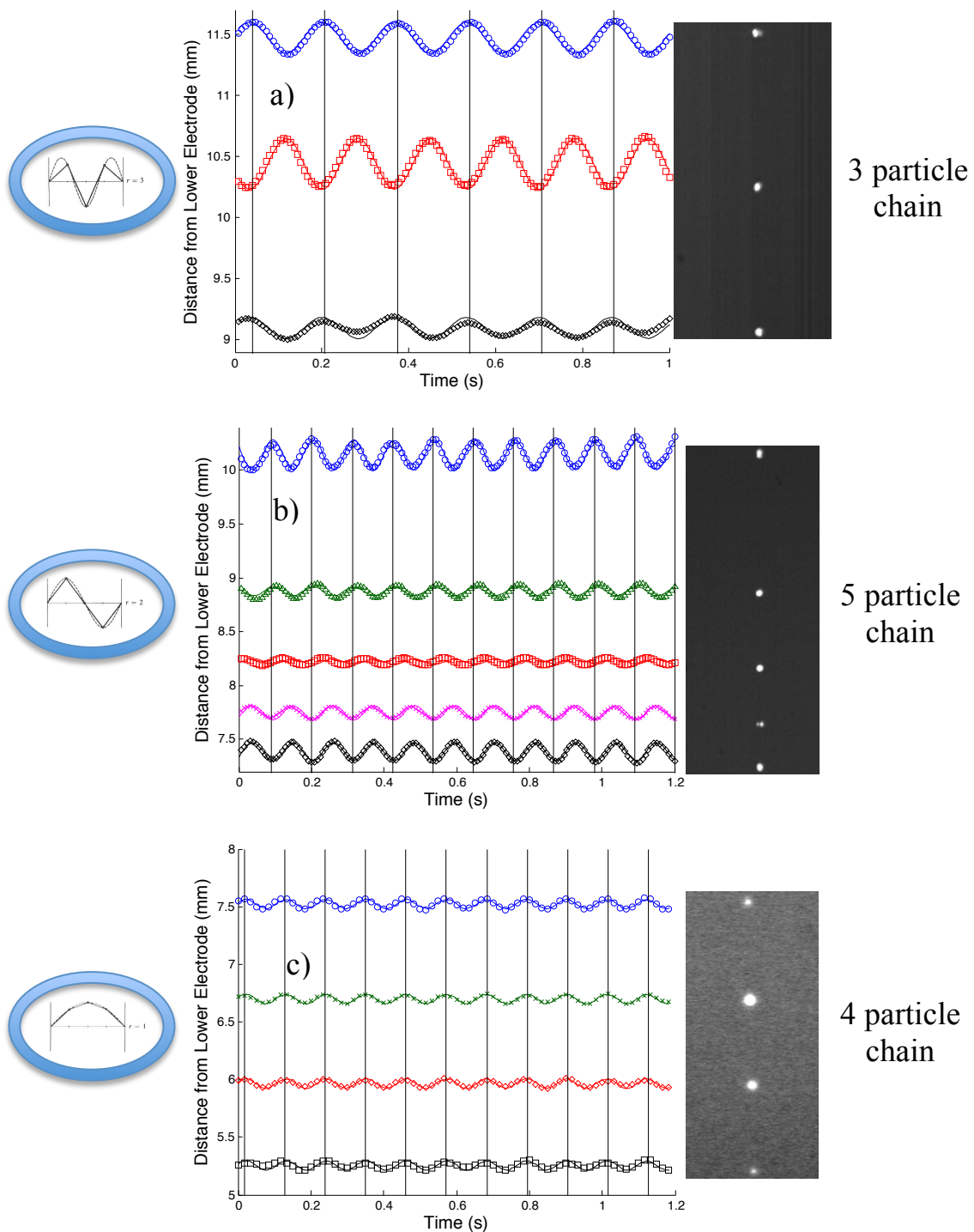


Figure 34 – Longitudinal dust chain waves with the central particle out of phase (a, antisymmetric mode), the central particle stationary (b, standing wave mode), and all particles moving together (c, symmetric mode). The experimental data is shown as points in plots a)-c) with vertical lines drawn for each cycle and the fits to the system of coupled oscillator equations are shown as lines. One cropped frame of each oscillation is included on the right. The relevant theoretical mode is circled at left.

4.4.3 Transverse Dust Chain Waves

Dust chains may also be perturbed in a direction transverse to their axis, by placing the probe at an appropriate off axis position (Figure 35). However, using this technique did not produce observable individual wave modes despite extensive exploration. The wave motion was always a superposition of fundamental modes. Horizontal motion of each particle in a five-particle chain transverse to the chain axis is displayed. The average positions in the plot are the equilibrium heights of the particles from the lower electrode. This allows visualization of the vertical interparticle distances. As in the longitudinal case, the phase difference, a characteristic of wave propagation, can easily be observed. Analysis of this phenomenon occurs in Section 5.4.3.

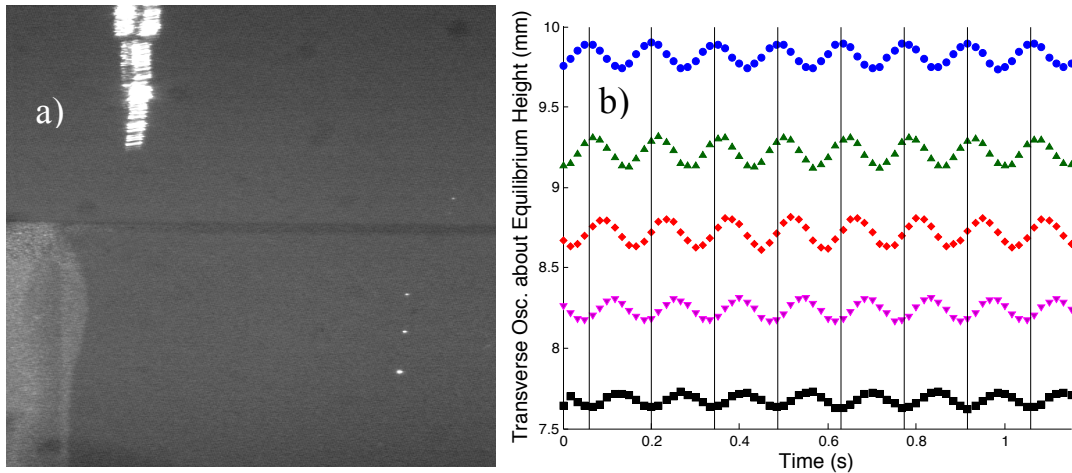


Figure 35 – a) Position of the probe utilized to generate transverse waves through dust particle chains. A three-particle dust chain is shown. b) Transverse motion of a five-particle chain, which was found to have the largest amplitude transverse waves.

CHAPTER FIVE

Results

5.1 Introduction

In this chapter, analysis is presented for each of the three experiments introduced in Chapter Four. The highlight from the experiments is their usefulness for calculation of plasma and dust parameters. In Section 5.2, the grain charge and the sheath edge electric field are found simultaneously by providing the sheath edge motion as input to the Green's function for a damped harmonic oscillator (Harris 2013). In Section 5.3, the cavities in single layer dust crystals produced from a negatively biased vertical probe are used to find the equilibrium grain charge and plasma screening length at the grain levitation height. Natural cavities are used to examine the flattening of the confinement potential at increased pressure. Cavities formed with a positively biased probe yield insight into the radial extent of the raised sheath phenomenon discovered in Section 5.2. In Section 5.4, adapted dispersion relations originally derived for horizontal chains are applied to data from the oscillation of vertical dust chains to find the grain charge and plasma screening length averaged over the chain length. Dispersion relations are fit to wave numbers extracted from data over driven frequency ranges at the system parameters used for all of the wave modes discussed in Section 4.4, finding that grain charge increases with an increase in system power.

5.2 Vertical Oscillation

Portions of this section have been previously published as: Harris, B. J., Matthews, L. S., and Hyde, T. W., *Phys. Rev. E* **87** (5), 053109 (2013).

In this section, the vertical asymmetric oscillation data discussed in Section 4.2 is analyzed, and a force balance model that assumes a linear electric field in the sheath is developed. By allowing a nonzero value for the electric field at the sheath edge, quantities such as the grain charge and ion drag are modified. Three mechanisms that have the potential to generate the oscillation are considered. When oscillating the probe potential at a frequency of 5 Hz, dust particles have less time to return to equilibrium, allowing superposition between cycles due to inertia to create higher maximum dust oscillation amplitudes than those seen at lower frequencies. This was not observed in the change of the position of the sheath edge, which consists of plasma particles much less massive than the dust. The superposition of the dust motion was exploited through the use of a Green's function to solve for the value of the electric field at the sheath edge and the grain charge.

Dust particle oscillation amplitudes were found to depend on the probe's bias and peak to peak oscillation potential (i.e., the amount of time the probe spends above the floating potential), as well as the DC bias on the lower electrode and the system RF plasma power (see Figure 22). A phase delay between the maximum driving force and the maximum particle height was observed (Figure 19). Such a phase delay is expected for a forced, damped oscillator, and is dependent on the forcing function. The measured particle oscillation amplitude was shown to follow that expected for a forced, damped harmonic oscillator, as seen by a fit to the amplitudes over a range of frequencies (Figure

17). Although sine wave potentials were applied by the probe, the asymmetric oscillations observed for the particle and sheath edge shows that the particle does not interact directly with the probe potential, but instead with the changing width of the plasma sheath.

The electric field in the sheath was also studied under applied perturbation, by analyzing the plasma glow. The plasma discharge intensity was shown to decrease by a maximum of 9% during probe oscillation (Figure 21), signaling a reduction in electron density in the plasma, with the greatest decrease occurring in the bulk (Figure 20). One unexpected result was that the position of the local maximum of the derivative of the emission profile in the lower sheath remained constant (Figure 16) under variation across all system parameters. Under the low power regime examined, the 1/e point of the emission profile was found to be a useful measurement of the sheath edge, as corroborated by Beckers (2011), and Samarian (2001).

The following numerical model was developed to examine the data described in Section 4.2 and shown in Figure 16. The general equation of motion for a dust particle is given by

$$m\ddot{z} = F_E - F_g - F_i + F_\beta, \quad (5.1)$$

where F_n are the forces produced by the electric field, gravity, streaming ions, and neutral damping (whose sign changes so that it always opposes the particle motion), respectively. The electric force is explained below, the gravitational force is constant for monodisperse particles, the ion drag is found from Eqn. 3.32, and the neutral drag force is dependent on a coefficient (β), which may be determined experimentally from vertical oscillation over a range of frequencies as described in Section 4.2 with the fit to Eqn. 4.1 multiplied by the negative of the grain speed.

The electric potential within the sheath is generally assumed to be parabolic (Tomme 2000),

$$V(z) = \left[\frac{(V_0 - V_p) - E_0 d}{d^2} \right] z^2 + \left[\frac{2}{d}(V_p - V_0) + E_0 \right] z + V_0, \quad (5.2)$$

where the fixed DC potential on the lower electrode is V_0 at $z = 0$ and equal to the plasma potential ($V_p = 39.5$ V for a system power of 1 W and a background gas pressure of 100 mTorr) at the sheath edge ($z = d$). By taking the derivative of Eqn. 5.2 to get the electric field, the electric force acting on a dust particle is

$$F_E(z) = 2Q \left[\frac{(V_p - V_0)}{d} \left(\frac{z}{d} - 1 \right) + E_0 \left(\frac{2z}{d} - 1 \right) \right], \quad (5.3)$$

where $Q < 0$ is the charge on a dust particle. The electric field at the sheath edge, E_0 , remains a free parameter and may be determined employing the method outlined below. This model was used to estimate the charge on the dust particle for each parameter configuration. Once the values of charge were found, changes in the plasma (for example, the sheath edge position and emission magnitude) based on changes of the experimental parameters were explored. A Green's function method will be used later to find E_0 and Q simultaneously; however, since E_0 is immediately required for further analysis, the result (2,800 V/m) is shown in all subsequent figures. The electric potential and electric field for a selection of values of E_0 is shown in Figure 36.

As discussed in Section 3.1.2, ions stream from the plasma bulk and are accelerated into the sheath (Chen 2006). For this experiment, it is initially assumed these ions exit the sheath edge at the Bohm velocity into a collisionless sheath. However, the ion-neutral mean free path ($\lambda = 625$ microns at 80 mTorr using the total cross-section from Lieberman (2005)) is smaller than the sheath thickness, which means the sheath exhibits

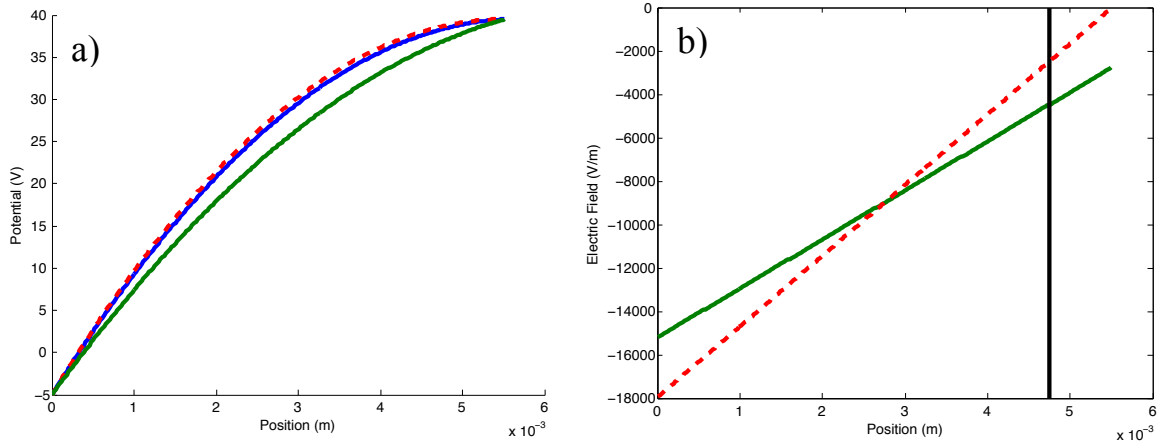


Figure 36 – a) The electric potential from Eqn. 5.2 and (b) electric field from Eqn. 5.3 in the region extending from the lower electrode ($z = 0$) to the sheath edge for the base configuration. The red dashed lines are with $E_0 = 0$ V/m and the green lines are for $E_0 = -2,800$ V/m. A value used in other work, $E_0 = -500$ V/m, is shown in blue for the potential. The slope of the electric field is reduced with an increase in the magnitude of E_0 . The black line in (b) denotes the dust position. The electric field at the dust position is 4,500 V/m for $E_0 = -2,800$ V/m, and -2,500 V/m for $E_0 = 0$ V/m.

some collisionality. Ignoring this effect overestimates the ion drag on a dust particle, since some momentum is transferred to the neutrals; however, this is still quite small relative to the other forces considered (Beckers 2011). Ion drag was calculated as explained in Section 3.2.2 using Eqn. 3.32, and added to the downward gravitational force. In this method, the ion and electron densities at the dust position were determined given the electric potential at the dust height, using the densities in the plasma bulk at the sheath edge. The plasma densities were calculated under the assumptions of energy conservation (i.e., the speed of the ions increases as they are accelerated toward the lower electrode, see Figure 37), the continuity equation for the ions (Lieberman 1988) (which quantifies the decrease in ion density as the ions accelerate toward the lower electrode, see Figure 37), and a Boltzmann distribution of electrons.

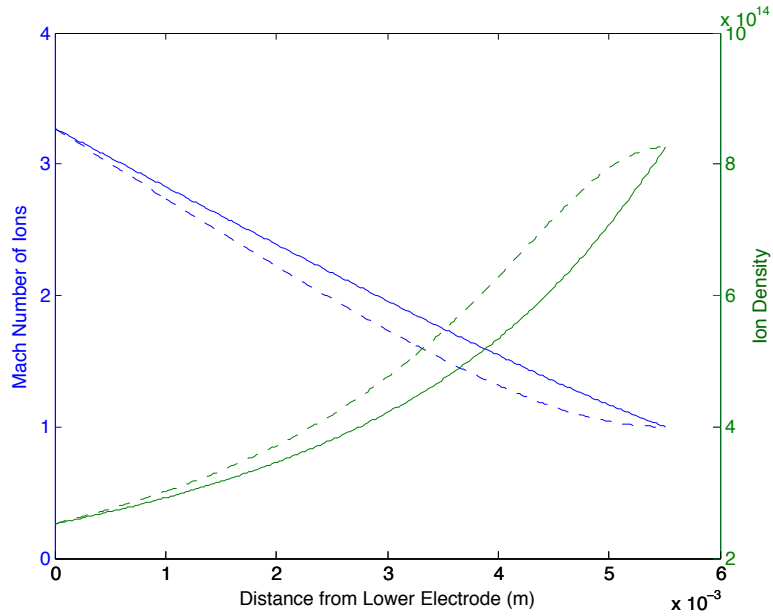


Figure 37 – Mach number of the ions (blue, left axis) and ion density (green, right axis) as a function of the distance from the lower electrode. Ions are moving faster as they accelerate toward the lower electrode, but their density decreases per the continuity equation. The solid lines represent calculations made with $E_0 = 2,800$ V/m and the dashed lines $E_0 = 0$ V/m. The ion drag resulting from these parameters is shown in Figure 39.

The initial force balance ($F_E = F_g + F_i$) for the base configuration (as given in Table 3) is shown in Figure 38, where the forces are normalized by the gravitational force upon a dust grain. The charge on the particle was adjusted so that the electric force balances the gravitational and ion forces at the experimental levitation height. For the base configuration, $Q = 8,300e$, which is 44% smaller than that found at the same pressure in a previous experiment in this GEC cell (Zhang 2010). However, in that experiment the charge was based on an assumed parabolic horizontal confinement potential; conceptually, if the confinement potential was smaller in the center, which may come about from the flat-bottomed cutout (employed in both experiments), the predicted horizontal amplitude would be greater, requiring a reduction in charge to match experiment. Note that the experimental charge must be found numerically because

changing the grain charge changes the ion drag force, and the resultant transcendental function does not admit an analytical solution.

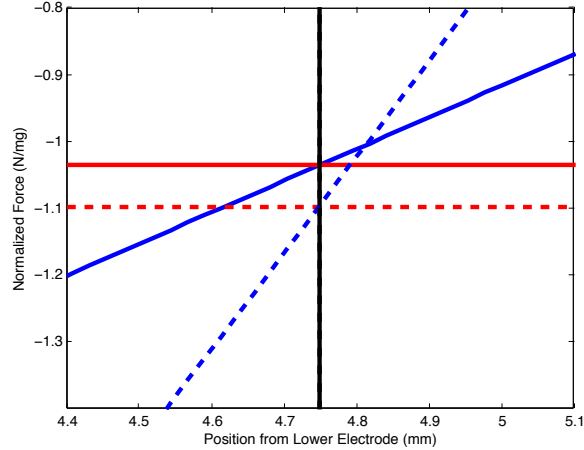


Figure 38 – Forces involved in levitation of the dust within the plasma sheath for $E_0 = -2,800$ V/m (solid) and $E_0 = 0$ V/m (dashed). The (red) horizontal lines represent the downward force of gravity including ion drag (hence the deviation from -1). The diagonal (blue) lines show the electric field calculated by Eqn. 5.3. The experimentally measured levitation height (black vertical line) is used to determine the particle charge by adjusting the electric force so that it intersects the combined downward force at the levitation height. For $E_0 = 0$ this charge is $16,600e$, whereas for $E_0 = -2,800$ V/m it is $8,300e$, which results in the ion drag decreasing with increasing $|E_0|$, shown in the change of the downward forces.

Table 4 gives the resulting particle charge found for all parameters. As shown, the charge increases with power, DC bias, and probe bias, but decreases with pressure, consistent with the observed rise and fall in particle height, respectively. Calculating the percentage difference in charge as the remaining parameters are changed finds them to be consistent within 2%.

The nonlinear increase in charge found with increasing power may be in part due to overestimation of the ion speed, as mentioned previously. For the case where $P = 1.5$ W, the particle levitates near the sheath edge, where nonlinearity of the electric field (Douglass 2011) occurs, which is not incorporated into the model. This results in an

Table 4 – Dust particle charge determined from the balance of forces as discussed in the text. All parameters were changed independently relative to the base configuration. The large particle charge for the highest power occurs due to the particle approaching the sheath edge. The values are in units of 10^3e .

Parameter	Low	Mid	High	Parameter	Low	Mid	High
Probe Bias	8.4	8.3	8.5	Height	8.3	8.1	8.3
Peak to Peak	8.2	8.3	8.2	Frequency	8.3	8.3	8.2
Power	7.1	8.3	10.5	DC bias	7.8	8.3	8.7
Pressure	8.5	8.3	8.1				

unrealistic increase in the ion drag. Note that the resulting charge increase with power is due to both the decrease in position of the sheath edge and the increase in the particle height as shown in Figure 16c.

Given the charge, the ion drag may now be calculated as a function of position. The value of the electric field at the sheath edge value sets the plasma density, which is then used to calculate the grain charge. Note that while the grain charge could also be a function of position (OML also becomes less applicable as a grain gets farther away from the bulk), the charge is fixed to that found for its equilibrium levitation height in order to isolate the dependence of ion drag on height for this analysis. Figure 39 shows how the ion drag and densities vary in the sheath, given charge calculated using two values of the sheath edge electric field. Though the Mach number increases lower in the sheath (Figure 37), the ion drag reaches a maximum and actually decreases as distance from the sheath edge is decreased (starting less than 1 mm below where the dust levitates for $|E_0| = 2,800$ V/m), due to the decrease in ion density. Though the electron density drops smoothly to zero at the lower electrode as electrons are repelled, the ion density remains

finite. While the lower region of the sheath is not important for this experiment, it becomes more relevant for the vertical dust chains discussed in Section 5.4.

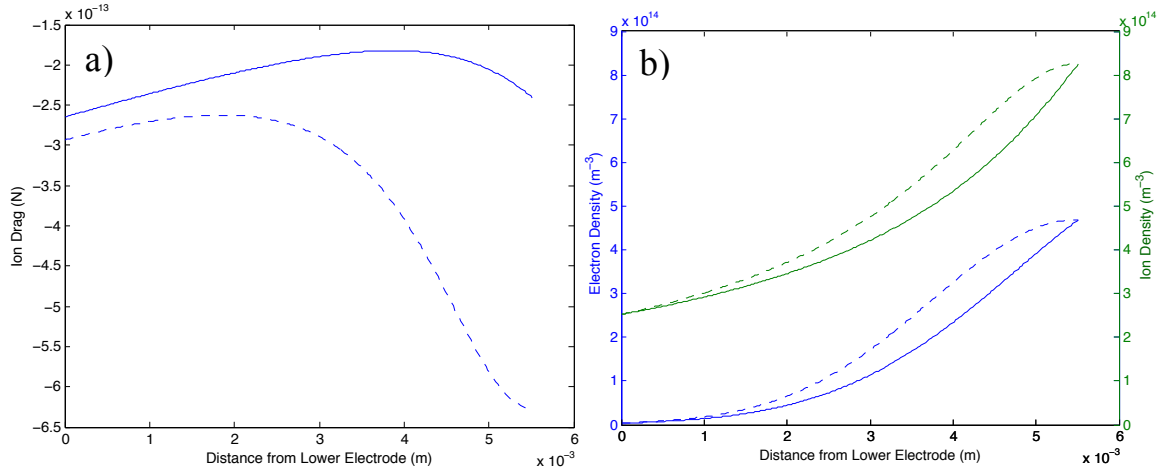


Figure 39 – a) Ion drag and (b) plasma densities as a function of position from the lower electrode. The solid lines represent calculations made with $E_0 = 2,800$ V/m and the dashed lines $E_0 = 0$ V/m. Here the equilibrium dust charge at the levitation height plays the largest role in modification of the ion drag for different values of E_0 . Note that the gravitational force for an 8.89 micrometer diameter particle is 5.4×10^{-12} N, about an order of magnitude greater than the ion drag force.

It is useful to consider how sensitive these results are to a variation in the electric field at the sheath edge. The most important quantities are the ion drag, Mach number, plasma densities, and sheath potential, as shown in Figure 40. The ion drag decreases in magnitude, as a result of the sheath potential decreasing at the dust position, which decreases both the ion and electron densities. The ion Mach number increases, due to the a greater difference between the plasma potential and the potential at the dust. Note that the ion Mach number increases to become greater than 1 since the ions are accelerated by the sheath electric field.

Adjusting the ion Mach number at the sheath edge also adjusts two relevant values as shown in Figure 41. Since the dust is close to the sheath edge, the Mach number does not

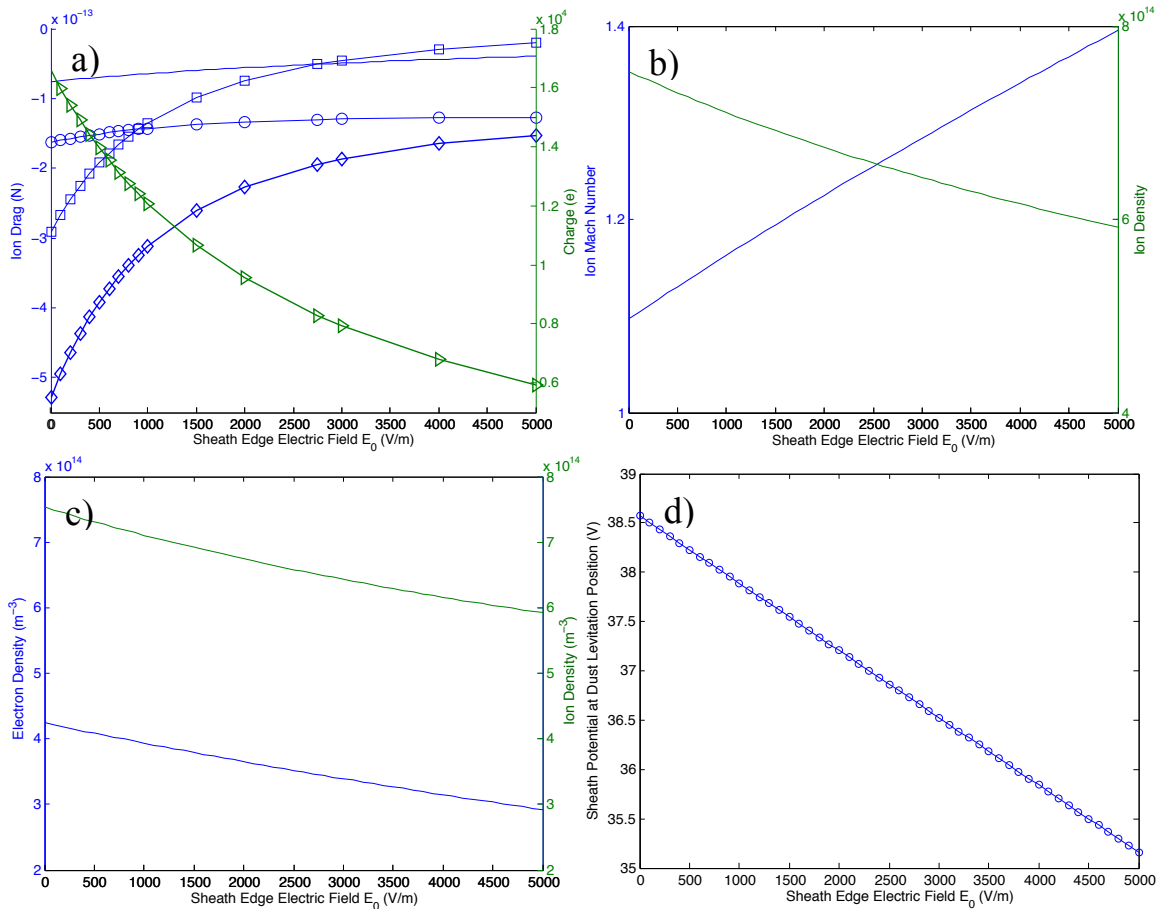


Figure 40 – Changes as a result of modifying the value of $|E_0|$, at the experimentally determined dust positions for the base configuration. With an increase in $|E_0|$, (a) the ion drag due to collection (circles), scattering (squares), and total (bolded, diamonds) decreases in magnitude, (b) the ion Mach number increases, (c) the ion/electron density decreases, and (d) the sheath electric potential decreases. Only the ion drag depends on the dust charge. If the charge is fixed at 8,300e (a, line without markers), the total ion drag does not change much, but if the equilibrium dust charge is allowed to vary for each value of E_0 (a, all other ion drag lines) the ion drag has a much greater variation over the range of values for E_0 .

have time to increase much by the time the ions reach the dust. The difference between the Mach number at the sheath edge and at the dust levitation position decreases as the Mach number at the sheath edge increases, because of energy conservation (see Eqn. 3.22). As shown in Eqn. 3.35, ion drag consists of contributions from ion scattering (passing by the grain) and from ion collection (directly impacting the grain). Increasing the ion Mach number at the sheath edge above 1 increases the magnitude of the ion drag.

As shown in Figure 41b, ion collection is the dominant contributor to the total ion drag at high Mach numbers, while ion scattering has its greatest contribution at low Mach numbers, when the ions spend more time within the Coulomb interaction range (about one screening length). The ion scattering is enhanced for high dust charge (which occurs for lower values of the electric field at the sheath edge).

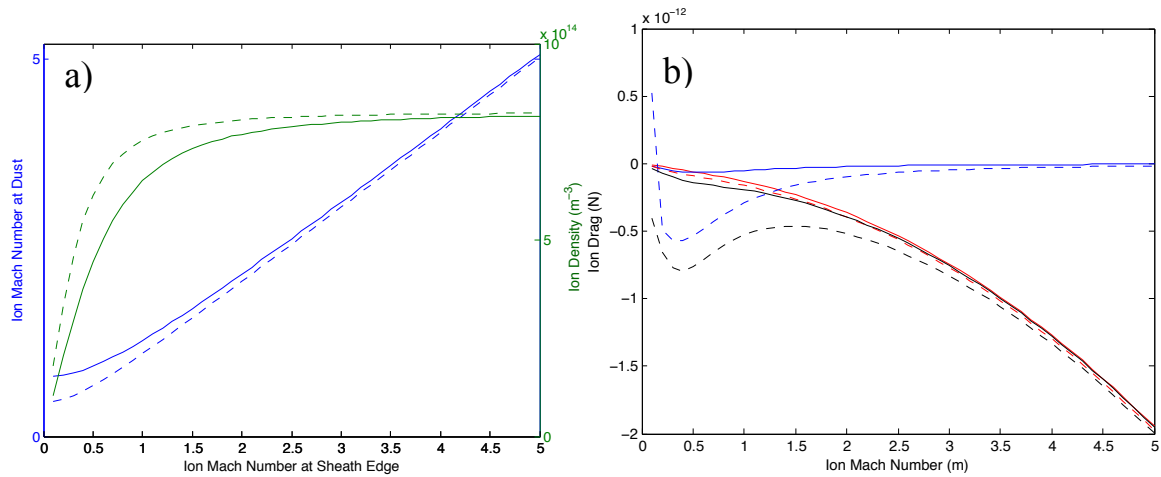


Figure 41 – As the sheath edge ion Mach number is increased, the change to (a) the ion Mach number at the dust height and (b) the ion drag at the dust are shown. The solid lines are for $E_0 = -2,800$ V/m and the dashed lines are for $E_0 = 0$ V/m. In (b), the red lines represent the ion drag from collection.–The blue lines represent the ion drag contribution from scattering. The black lines represent the total ion drag.

Comparing the experimental data with the model allows examination of the mechanism behind the asymmetric oscillation observed (see Figure 16). There are several ways to perturb the electric field model in order to produce a vertical oscillation. First, the 1/e point (see Section 3.1.2), when experimentally tracked over time, can be used to monitor the position of the sheath edge, which changes the electric field calculated by Eqn. 5.3. Second, the potential at the sheath edge (i.e., the plasma potential V_p) can be altered sinusoidally to follow the potential on the probe while the sheath edge position remains fixed. Third, the charge on the particle can be changed by oscillating

the plasma power, which also changes the ionization rate and plasma density. Since the change in plasma power and the manner in which it affects the grain charge requires many assumptions, the charge was instead estimated as a function of the grain's vertical position and the plasma emission intensity measured during probe potential oscillation. For each of these methods, force balance can be used to predict the position of the particle as a function of time. Changes in ion flow due to the probe potential were also considered. However, when the probe is more positive than the plasma potential, downward ion flow should increase in speed, reducing the particle levitation height. Therefore, it cannot independently generate this oscillation.

The results of the perturbations discussed above are shown in Figure 42, using the experimentally determined particle charge. As shown, calculations based on applying the experimental shift of the sheath edge yield the best prediction of the particle's motion (green circles). Taking the probe bias directly into account by applying a sinusoidal plasma potential results in sinusoidal particle motion (red squares). For the base configuration, the probe bias and amplitude used in the model had to be reduced from experimental values by about 70% in order to match the measured equilibrium height and oscillation amplitude of the dust. This reduction is due to plasma shielding: for the parameters given in Table 3 (in Section 4.2) a Debye length of 695 microns was calculated following the formula in (Popel 2003),

$$\left[\frac{1}{\lambda_{De}^2} + \frac{1}{\lambda_{Di}^2(1+u^2)} \right]^{-1/2}, \quad (5.4)$$

where u is the ion streaming velocity normalized to the ion thermal velocity, which was used for the ion drag calculation. The correction factor to the ion Debye length term is required to compensate for superthermal ions, which can't participate in screening

(Khrapak 2005). However, increased shielding from the probe is expected since the probe is several millimeters away from the dust. Nevertheless, the electron temperature change in the vertical direction was not measured (as was done by Samarian et al. (2001)), so shielding was not included. For the third perturbation where a possible change in charge is considered, the resulting grain motion is determined by allowing the charge to change as a function of the maximum emission intensity, $I(t)$, resulting in motion indicated by the blue diamonds. In this case, the charge ranges from its equilibrium value (Q_0) to the value found from the force balance when the particle is at its maximum position (Q_{max}). This result is adjusted following an interpolation inversely proportional to the reduction in $I(t)$, with functional form

$$Q(I(t)) = Q_0 + (Q_{max} - Q_0) \frac{I_{max} - I(t)}{I_{max} - I_{min}}, \quad (5.5)$$

where I_{min} (I_{max}) is the minimum (maximum) value over time of the maximum plasma intensity. The ion drag calculation in this case is fixed, and uses only the equilibrium charge value.

Although a reduction in intensity generally signals a reduction in power delivered to the plasma and thus a reduced grain charge, the fact that the particle position increases implies the reverse. There are several possible explanations for this. Increasing the electron flow to the positive probe would increase the electron flux impacting the dust. The particle could also rise due to the increase in plasma shielding length due to a reduced electron density; this would increase direct attraction by the probe and repulsion from the lower electrode. The probe's electric field could interact with that of the sheath as well; however, since the tip is approximately 10 shielding lengths away from the dust,

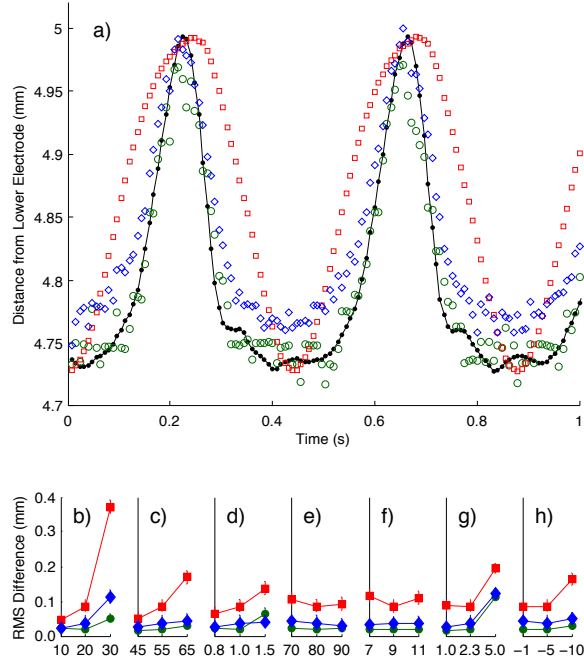


Figure 42 - Predictions of multiple perturbations to the simple electric field model for the base configuration with $E_0 = -2,800$ V/m. The dust grain position as a function of time is shown in (a). The (black) dots give the experimental particle position. The (red) squares represent the result of adjusting the sheath edge. The (blue) diamonds represent changing the plasma potential based on the probe oscillation. The (green) circles represent changing the grain charge (with the ion drag calculated from the equilibrium charge). The average RMS deviation of the perturbations to the experimental data are shown in b)-h), where the parameter varied is (b) probe bias (V), (c) probe peak to peak (V), (d) system power (W), (e) pressure (mTorr), (f) probe height (mm), (g) frequency (Hz), and (h) DC bias (V). The only qualitative difference with $E_0 = 0$ V/m is that the potential oscillation is not flattened on the rise. Error bounds, determined by adding one pixel of distance (23 microns) to the particle position and calculating the resulting RMS differences, are included. The same is done after subtracting one pixel, so the error bars are not necessarily symmetric.

these effects are limited. It may be surmised that the most likely process is that the plasma bulk contracts due to a reduction in electrons as the probe collects them, raising the sheath edge, while the charge remains relatively constant.

The plots shown in Figure 42b-h illustrate the average root mean square (RMS) deviations for the parameters tested as compared to experimental results. The RMS deviation for modifying the location of the sheath edge is smallest in 13 of the 15 cases, implying this is the best possible explanation, although the other effects discussed may

contribute to the oscillation as well. Besides these perturbations, the speed of the flowing ions could also be directly affected by the probe; however the ion drag would need to increase by a few orders of magnitude in order to independently generate the observed particle amplitude, and the greatest motion would then occur during the maximum negative potentials (a phase shift of π rad from that seen in the experiment). Therefore this oscillation can be considered a far, secondary plasma interaction, unlike the near field effect studied in a powered horizontal wire experiment (Samsonov 2001).

To enhance the argument that sheath edge movement is the primary generating mechanism for the oscillations observed, the particle motion is predicted using a damped, forced, oscillator Green's function in discrete form,

$$Z(t) = \sum_{t'=0}^t \frac{F(t')}{m\omega_1} e^{-\beta(t-t')} \sin[\omega_1(t-t')] \Delta t' + Z_0 \quad (5.6)$$

where $\omega_1 = (\omega_0^2 - \beta^2)^{1/2}$, and $F(t')$ is the force applied. If this force comes solely from movement of the sheath edge, the net force will be due to the difference between the electric force when the sheath edge is at equilibrium position d_1 and the electric force after the sheath has moved to d_2 at time t' , which is

$$F(t') = -2Q \left(\frac{1}{d_2(t')} - \frac{1}{d_1} \right) \left\{ (V_0 - V_p) \left[\left(\frac{1}{d_2(t')} + \frac{1}{d_1} \right) z - 1 \right] - E_0 z \right\}. \quad (5.7)$$

A recursive method was used so that Eqn. 5.6 calculates the present dust position $Z(t-\Delta t) \rightarrow z$. Therefore, the only inputs to Eqn. 5.6 are the sheath edge as a function of time, the initial particle position, and the equilibrium particle height (Z_0). A method was attempted that adjusted d_1 to be the sheath edge position a particular number of time steps before that found at d_2 . Despite adjusting the number of time steps, this did not improve the results.

The Green's function method was first applied to the data in which the probe potential oscillation frequency in the base configuration has been increased to 5 Hz (henceforth referred to as the 5 Hz configuration), as shown in Figure 43. The Green's function prediction in the figure is shown with the amplitude fit parameters (neutral drag and resonant frequency) taken from Figure 17; these are in very good agreement (42 μm average RMS difference after $t = 0.4$ s). The result using the best fit parameters $\beta = 6.5$ s^{-1} , $\omega_0 = 66$ rad/sec, $Z_0 = 4.7$ mm, with the charge and E_0 value set below, is also shown with slightly better agreement (24 μm average RMS difference after $t = 0.4$ s). Using the best fit parameters, the base configuration is also modeled in Figure 43, with an average RMS difference from the data of 17 μm . The differences using best-fit parameters correspond to 0.68% and 0.51% of the particle amplitudes for the base and 5 Hz configuration, respectively. Note, on the other hand, that the increase in amplitude around 5 Hz shown in Figure 17 and Figure 22f, is not well modeled using the force balance method alone to predict the change (Figure 42g). As observed before, damped oscillators inherently have a phase difference between the force and the resultant particle motion. This model does predict the correct phase difference, once again confirming the prior statement that the standard phase difference formula for damped, harmonic oscillators does not apply for nonharmonic forces.

Increasing the magnitude of the sheath edge electric field (E_0) decreases the amplitude of the force, requiring an increase in charge magnitude to match the amplitude found in the data. The charge needed to match the amplitude is shown as a function of E_0 in the Green's function method and in Figure 44 by the red line. This is opposite of

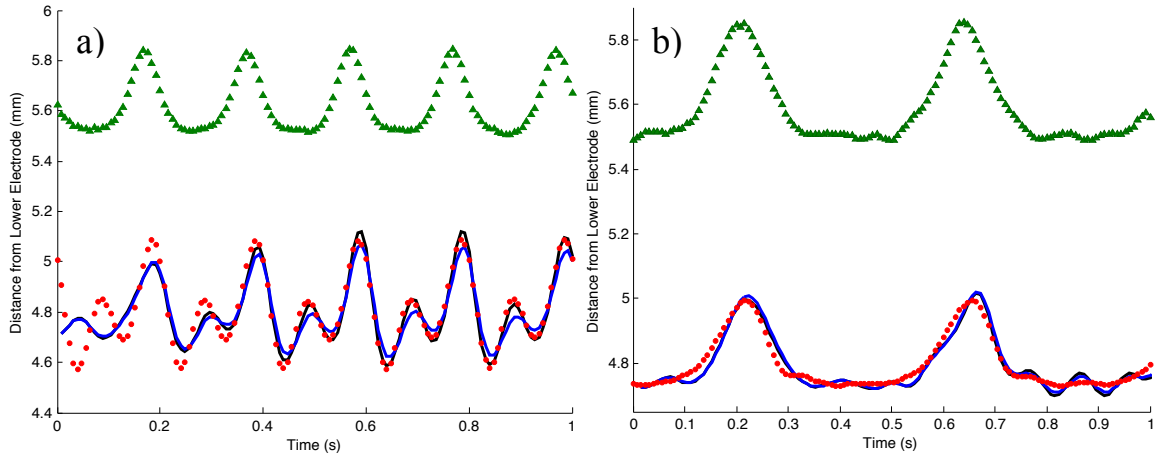


Figure 43 - Particle levitation height (red circles) and location of the sheath edge (green diamonds) as a function of time for probe potential oscillation frequency of (a) 5 Hz and (b) base configuration. The particle levitation heights predicted by the oscillator Green's function using the damping and resonant frequency found from Figure 17 (blue line) and best-fit parameters (black line) are superimposed.

the effect of E_0 on the force balance method as shown by the blue curve in Figure 44. The two methods match at $E_0 = -2,800$ V/m, with a charge of 8,300e, as shown in Figure 44; this falls in between previously published estimates of -500 V/m (Sharma 2012) at lower pressure and -15,000 V/m using $E_0 = kT_e/\lambda$ (Tomme 2000). Although the calculated charge has changed substantially, other charge determination experiments have rarely used E_0 when estimating the electric field. Changes in previous predictions of charge may have occurred had they done so.

To summarize, a discrete Green's function for a forced, damped oscillator (Eqn. 5.6) was applied to the 5 Hz configuration which accurately predicted the particle behavior, using only the force generated from the changing location of the sheath edge. A non-zero value of the electric field at the sheath edge, E_0 , was incorporated into the equation for the electric force acting on the dust particle (Eqn. 5.3). This parameter was adjusted in conjunction with the particle charge in order to match the measured particle oscillation.

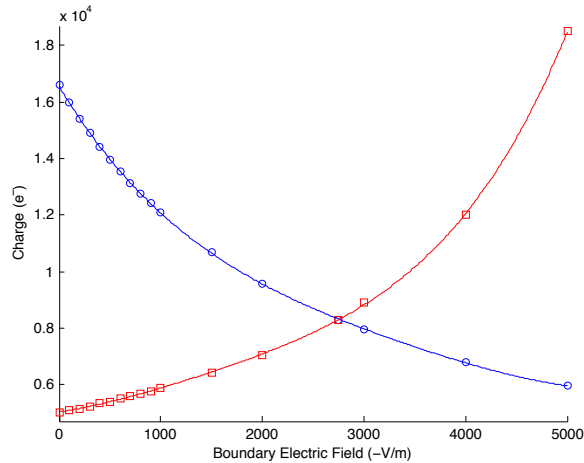


Figure 44 - Method to find the sheath edge electric field value. The (blue) circles reflect the resulting grain charge using the force balance method, and the (red) squares reflect the grain charge using the Green's function fit, as a function of the sheath edge electric field value. The intersection point occurs at $|E_0| = 2,800$ V/m, $Q = 8,300e$.

Using these parameters in the force balance equation allowed both E_0 and Q to be determined. Parameters found to match the 5 Hz configuration ($E_0 = -2,800$ V/m, $Q = 8,300e$, $\beta = 6.5$ s⁻¹, $\omega_0 = 66$ rad/sec, and $Z_0 = 4.7$ mm) also provided an excellent fit to the particle motion for the base configuration of the experiment. This method was further confirmed by the output of a phase difference that matched experimentally observed results.

In conclusion, a new technique has been developed which allows determination of both the charge on a dust particle and the electric field at the sheath edge within complex plasma. This was accomplished using an adjustable, powered vertical probe inserted into the system to create an intentional oscillation of the dust through direct modification of the plasma bulk. The resulting perturbation physically displaces the sheath edge allowing dust particles to be used as probes, the dynamics of which also provide direct measurement of the neutral drag coefficient and the resonant frequency. Measured values are comparable to those found in previously published experiments (Trottenberg

1995, Zhang 2010), except for the sheath edge electric field, which has not been previously measured.

This experimental technique lends itself to several plasma diagnostics. With appropriate calibration, the intensity reduction observed in the bulk could be used to calculate the change in electron density. This could provide an additional experimental parameter for plasma electromagnetic wave transmission studies, such as Faraday rotation. Additionally, the fixed point of the position of the local maximum of the derivative of the emission profile may be dependent only on the geometry of the cell; if so, it could be useful as a point of reference for image analysis. Finally, ion drag in the numerical model may be improved by changing the formulas used to calculate the decrease in ion and electron densities from the sheath edge (Land 2009), or testing the importance of the ion-neutral collisions and the nonlinearity near the sheath edge. Though the ion drag is small for most of the plasma parameters in this experiment, it does increase significantly with power and would increase if the ion speed was found to be greater than the minimum Bohm velocity.

5.3 Dust Cavities

5.3.1 Introduction

In this section, the cavities (as described in Section 4.3), generated by three different mechanisms, are analyzed. First in Section 5.3.2, repulsion of micrometer-sized particles by a negatively charged probe is investigated. A model of this effect developed for a DC plasma is modified and applied to explain new experimental data in RF plasma. In Section 5.3.3, the formation of natural cavities is surveyed; a radial ion drag proposed to

occur due to a curved sheath is considered in conjunction with thermophoresis and a flattened confinement potential above the center of the electrode. Finally in Section 5.3.4, cavity formation unexpectedly occurs upon increasing the probe potential above the plasma floating potential. The cavities produced by these methods appear similar, but are shown to be produced by fundamentally different processes.

5.3.2 Negative Probe Potential Induced

The cavities formed by applying a negative potential to the S100 probe (as described in Section 4.3) were modeled. Initially, the probe was assumed to be a line charge and a Yukawa interaction potential applied between it and the dust. However, no parameters were found that predicted the cavity sizes observed experimentally. A second model, previously published (Thomas 2004) for a DC experiment, was adapted and found to fit the data. The procedure of this model is as follows: the negative probe is assumed to attract the plasma ions, and to account for collisions between ions, the flow is assumed to be mobility limited, with mobility defined to be

$$\mu = \frac{e}{m\nu}, \quad (5.8)$$

where ν is the collision frequency given that the ions are singly ionized. The ion velocity is then μE . The linear continuity equation,

$$n_0 u_0 = n u, \quad (5.9)$$

where n_0 and u_0 are the initial density and ion speed and n and u are the density and ion speed at any other position, is now assumed to apply in the horizontal direction with a radial coordinate. The boundary electric field value at the inner dust ring edge was found using a model for ion drag force (Eqn. 3.35) and the assumed source of the cavity a balance between outward electric field and inward ion drag, both of which are provided by the probe potential. The electric potential at the inner edge of the dust ring is defined

to be 0 V. The value the model predicts at the center of the cavity, if it is correct, should then match the difference between plasma potential and applied probe potential.

A series of plots of cavity sizes over various parameters (flattened from the 3-dimensional shown in Figure 27) is given in Figure 45. As shown, the cavity size increases linearly with decreasing negative probe potential. At high pressure the range of the cavity size is reduced (reflected in decreased slopes), as the cavities are initially larger (shown later to be the result of a natural cavity contribution). At low pressure, plasma densities are also lower and the sensitivity to the probe is increased due to the increase in screening length, as reflected in larger slopes of the fit lines. At low power, the size increases since ionization is smaller making the screening length larger. The reverse is true for high power (though again, the natural cavity takes effect at high pressure, as shown for 300 mTorr in Figure 45).

It is important to note that differences in our system from those used by Thomas et al. exist. First, a single ring of dust particles is difficult to achieve, especially when changing the size of the ring drastically with the probe. Therefore, dust outside the inner ring creates an inward force. This was added to the inward ion drag force using the formula

$$F_d = \sum_{dust} \frac{Q^2}{4\pi\epsilon_0 r_d^2} e^{-r_d/\lambda_D} \left[\frac{1}{r_d} + \frac{1}{\lambda_D} \right] \cos(\theta), \quad (5.10)$$

where the sum is over all other dust particles, each a distance r_d away from a given inner ring particle, and θ is the angle between each outer particle and the line produced by connecting the probe position to an inner ring particle. The results of this calculation are shown in Figure 46. While the particles are repelled to a greater extent from the

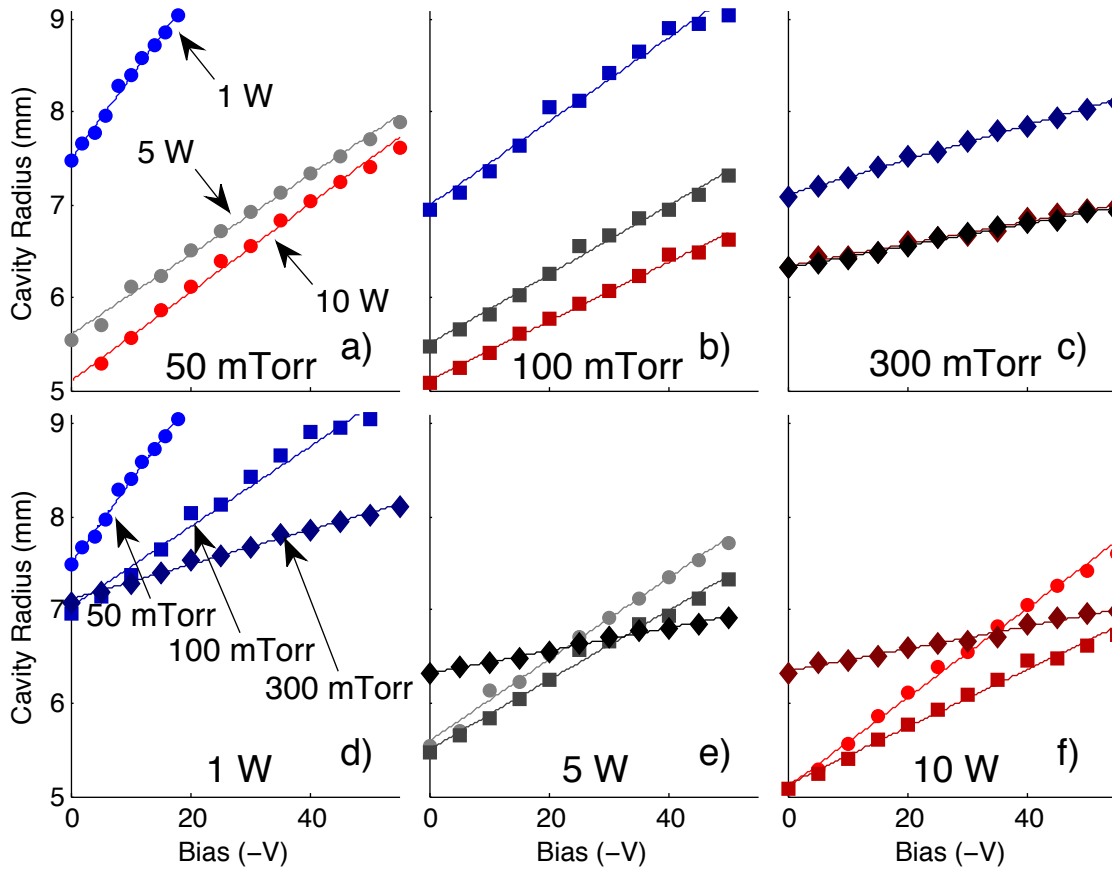


Figure 45 - Cavity radii as a function of the probe bias with respect to ground with linear fits. Data in each plot is taken at the fixed value listed at the bottom. The plasma power is represented in blue for 1 W, grey for 5 W, and red for 1 W. The neutral gas pressure is represented by circles for 50 mTorr, squares for 100 mTorr, diamonds for 300 mTorr.

confinement potential as they are pushed farther away from the center at more negative probe potentials, this is countered by less surrounding dust as the cavity grows. This dust force was added to the ion drag force (shown in Figure 48) to find the electric field at the inner dust ring (right), which is required as a boundary value in the Thomas model. Though only particles near a particular inner ring particle apply significant repulsion due to plasma screening, it was simpler in the numerical model to allow it to calculate all interactions instead of incorporating a method to consider only particles in a specified vicinity. These outer dust particles may also inhibit the ion flow, though this effect was

not included. The line charge model mentioned before not only failed to predict the cavity size directly, but using the differences between cavity sizes (and Eqn. 5.10 to provide the total dust force) at different probe potentials in the line charge model also failed to predict grain charge and screening length.

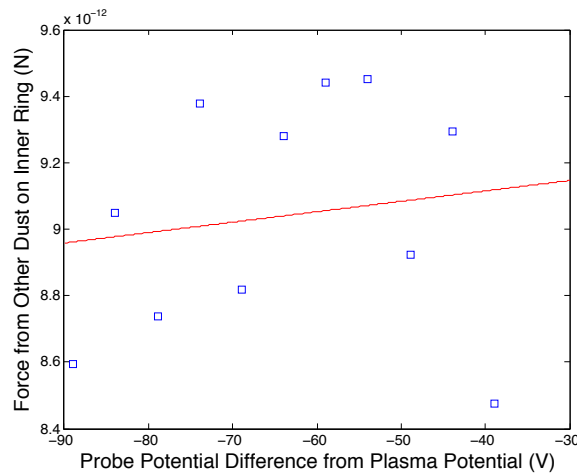


Figure 46 – Average dust force on the inner ring. Data points indicate the result for a given probe potential difference from the plasma potential, while the red line denotes the average.

Because Langmuir probe measurements are only valid in the bulk, plasma parameters in the sheath at the location of the dust were calculated using the methods discussed in Section 5.2. In this experiment, the sheath edge was found using the equilibrium levitation height of 0.46 micrometer diameter particles. This calculation resulted in an ion density of $3.4 \times 10^{14} \text{ m}^{-3}$ at the equilibrium dust height. Since the asymmetric oscillation damps above 1.5 W system power, and 10 W were used for primary analysis in this model, the Green’s function method explained in Section 5.2 could not be applied here to find the electric field at the sheath edge. Though the cavity model did not directly require this value, it is used in the estimation of the plasma ion density at the dust position. However, as seen in Figure 39, changing the sheath edge electric field does not

alter the plasma densities significantly, so the electric field at the sheath edge was taken to be 0 V/m for this experiment. Since the Khrapak model for ion drag was already established for the vertical oscillation experiment, it was also applied here in place of the ion drag calculation by Barnes et al. (1992) that was used by Thomas et al.

The model used by Thomas et al. was able to correctly predict the cavity sizes found in experiment, given that the electron density was allowed to change. Because the

$$\phi''(r) + \frac{en_{i0}}{\epsilon_0} \left(\frac{E_0}{|\phi'(r)|} - \frac{n_{e0}}{n_{i0}} e^{e\phi(r)/kT_e} \right) = 0, \quad (5.11)$$

electrons move faster than the ions, it is reasonable that the electrons would respond first, being increasingly repelled as the negative probe bias is decreased. It is plausible that the electrons expelled radially from the cavity would increase the electron density at the dust. A reduction in the electron repulsion at large distance from the probe would occur due to plasma screening. The model used by Thomas et al. (2004) quantifies the electron density change, which is shown in Figure 47. The electric field as a function of radius is found (by taking the negative derivative of the potential) from a solution of the Poisson equation,

where ϕ is the electric potential, kT_e is the electron energy, and E_0 is the electric field at the cavity edge. The negative current to the probe below the floating potential is much lower in magnitude than the positive current above the floating potential. The cavity radius grows linearly with decreasing probe potential below the floating potential, but increases less uniformly above the floating potential. The model used by Thomas et al. only applies to the potentials below the floating potential. As employed by Thomas et al., the quantity nu (see Eqn. 5.9) equals the flux (nu has units of particles per area per time) to the probe, I/eA_p , where I is the probe current (also shown in the figure) and A_p is the

probe area. The plot versus current looks very similar to that shown in Thomas et al. The floating potential is found where the current goes to zero, 8.9 V in this case, which is coincidentally where the smallest cavity radius is found. The electron densities at the dust are comparable to the natural bulk electron density of $2.7 \times 10^{15} \text{ m}^{-3}$.

Other quantities necessary to use the Thomas et al. model are shown in Figure 48. As shown in Figure 47b the electron density at the dust was found to change, and therefore OML theory produced dust charge values that changed (Figure 48a-b). These charge values increased in magnitude by 10.1% over the range of probe potentials of -5 to -55 V with respect to ground. As the dust charge increases in magnitude, the magnitude of the ion drag force increases. Both of these variations were found to be linear. Note that the ion drag force is used to find the boundary value of the horizontal electric field, shown in

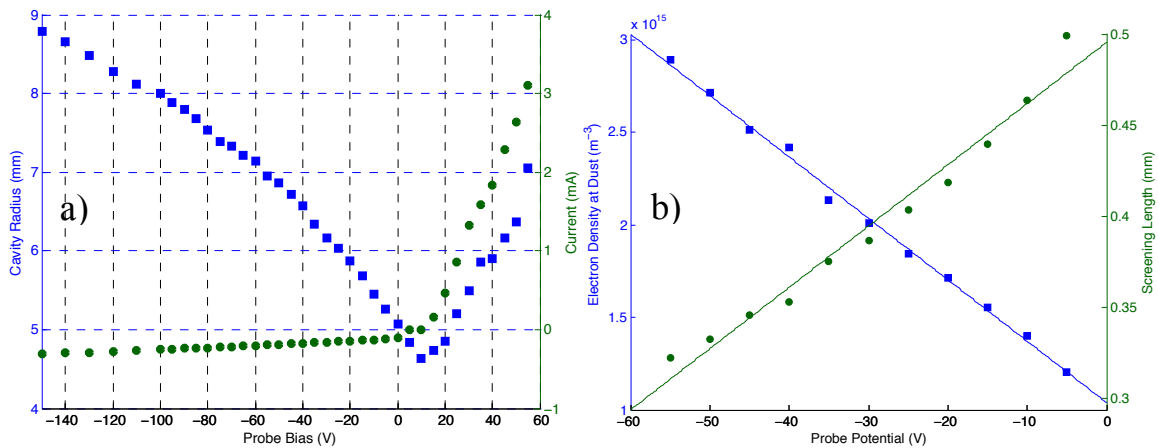


Figure 47 – a) A detailed plot of the cavity radii (blue squares), (b) electron density (blue) and screening length (green) at various probe potentials. The electron density points are calculated by solving Eqn. 5.11 such that the model simultaneously predicts the correct potential at the probe and measured cavity size, which then change the screening lengths (right axis).

Figure 49, calculated to equal to the inward ion drag in addition to the net force from the outer particles. Extrapolation of the dust charge as a function of the probe potential to the

probe floating potential, which is -25.0 V (for 10 W, 100 mTorr) with respect to the plasma potential (defined to 0 V as done by Thomas et al.), results in a value of 48,900e. Proceeding with the same method for the electron density, the equilibrium electron density at the dust is found to be $5.3 \times 10^{14} \text{ m}^{-3}$. This is comparable to the values calculated using the continuity and energy conservation equations from the bulk electron density at the dust levitation height for a value of the electric field at the sheath edge of 2,800 V/m, $3.9 \times 10^{14} \text{ m}^{-3}$, and of 0 V/m, $8.7 \times 10^{14} \text{ m}^{-3}$. Because the electron density changes, the screening length changes as well. As the electron density increases, this causes a decrease in screening length, because more electrons are available for screening. Again through extrapolation, the equilibrium screening length is found to be 530 microns at the dust levitation height. As n_e , Q , and λ_D are important quantities to characterize the dust/plasma system, this method provides a new way to measure them without relying on inaccurate Langmuir probe measurements in the sheath.

Since this experiment is run at higher power than the experiment in Section 5.2, plasma parameters in the vertical direction will change more significantly. The characteristic finite ion density at the lower electrode is shown in Figure 50, as found for the vertical oscillation parameters in Figure 39. However, in this case the ion density more closely approaches the electron density. Because the dust charge changes as a function of the probe potential, the natural vertical ion drag also increases, though it is not as strong as that in the horizontal direction for any of the applied probe potentials. It is primarily from the ion scattering portion and not the ion collection.

The results from the model used by Thomas et al. are shown in Figure 51. The end

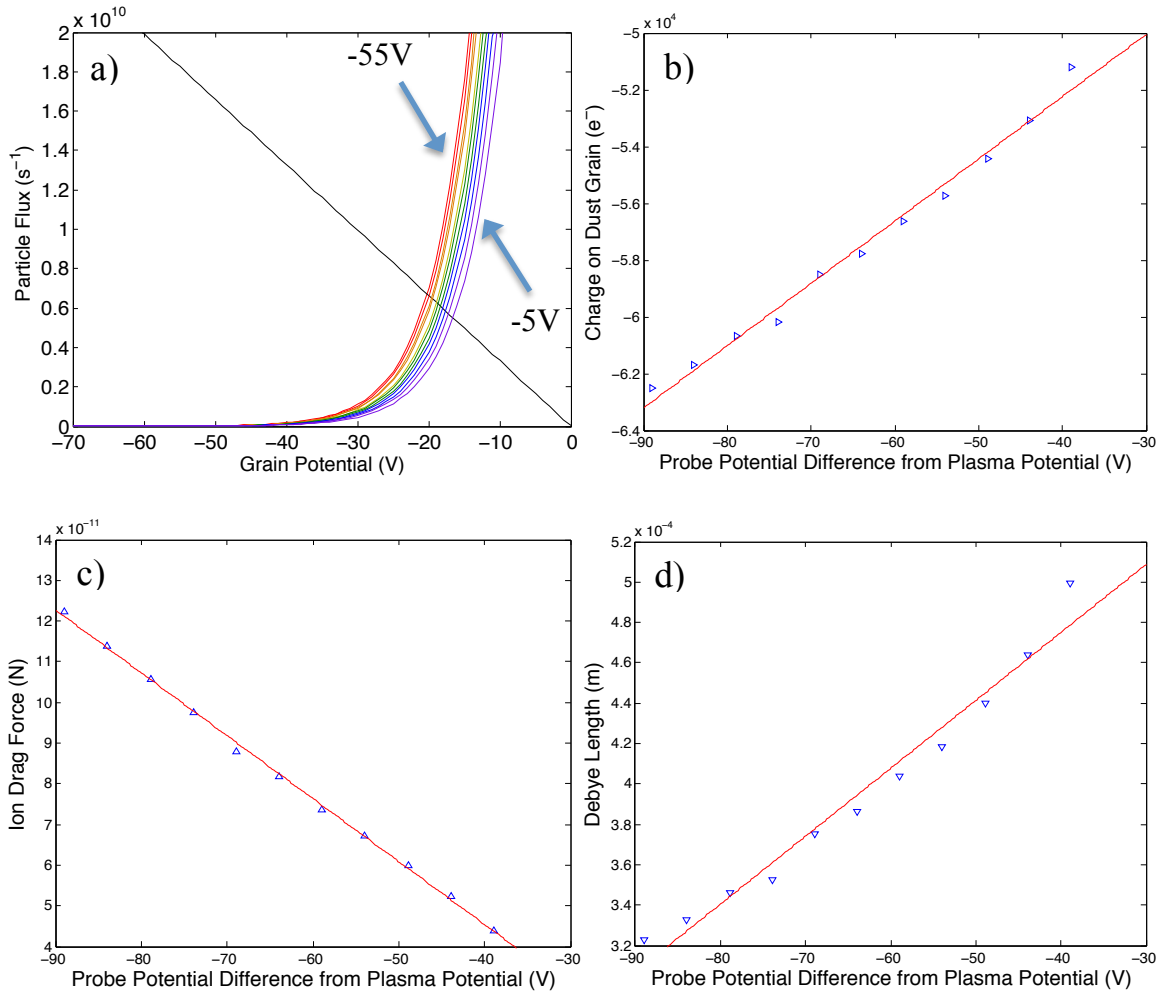


Figure 48 – Quantities which affect the size of cavities produced by the negative probe potential. OML is used to find the particle charge. a) Particle flux to a charged dust grain. The ion flux (diagonal line) is fixed at each probe potential, while the electron flux is shown for probe potentials ranging from -5V (violet) to -55V (red). b) Grain charge as a function of probe potential, calculated using the particle fluxes shown in (a). c) Ion drag as a function of probe potential, using the charges shown in (b). d) Electron screening length at the location of the dust. In (b)-(d) points represent calculated values, while the red line is a linear fit.

points of the electric potential (with respect to the plasma potential) in the cavity are fixed in position by the radius of the experimental cavity and in potential by the difference between the bulk plasma potential and the probe potential at the probe. For a large range of distances from the probe (0 to 5 mm), the electric potential is parabolic and

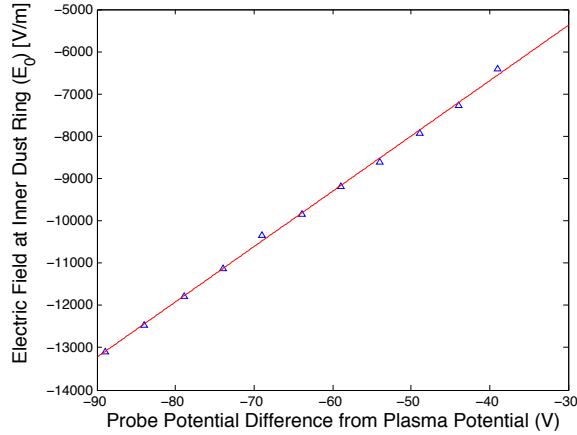


Figure 49 – Boundary electric field value (E_0) as a function of the probe potential. Points represent the calculated values, and the red line is a linear fit.

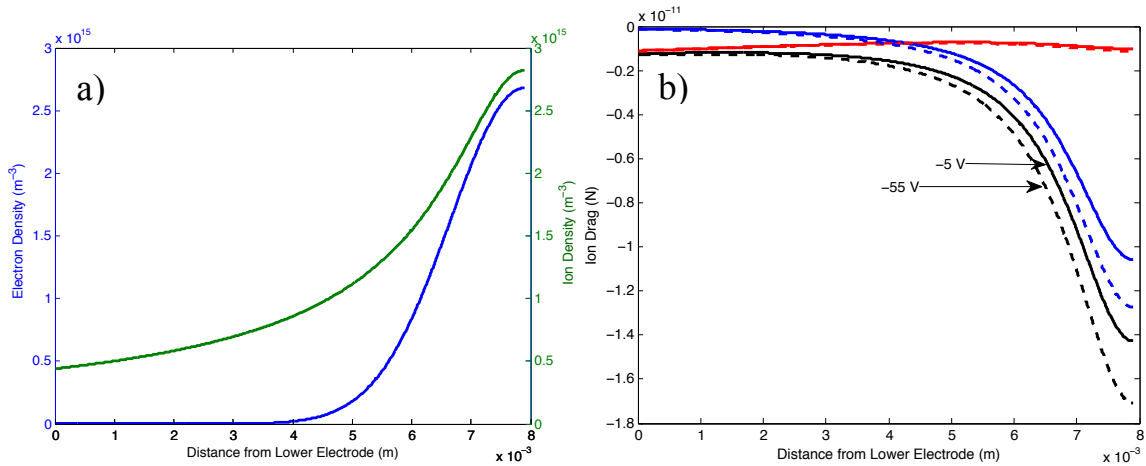


Figure 50 – a) Ion and electron plasma density and b) ion drag in the vertical direction as a function of distance from the lower electrode for 10 W plasma power and 100 mTorr system pressure (compare to Figure 39). The total ion drag (black) is the sum of ion scattering (blue) and ion collection (red). Ion drag is affected by the particle charge, which is a function of the probe potential. Results are shown for dust charge with probe potential at -5 V (solid lines) and -55 V (dashed lines).

the electric field linear, similar to electric fields found in the vertical direction experimentally (Tomme 2000). The small deviation in the electric potential near the inner dust ring results in a more abrupt change in the electric field at that position. As discussed above, the dust in the plane outside the inner ring could disrupt ions streaming

horizontally toward the probe, reducing the ion drag. This would in turn reduce the magnitude of the electric field at the inner dust ring, applied as a boundary condition, which would allow reduction of the electric field gradient in that region. However, the ions can be accelerated within a distance of about an interparticle spacing (Figure 11), and most likely have a vertical component due to the streaming ions as well as the sheath electric field acceleration. A molecular dynamics simulation of this effect would be useful for further consideration.

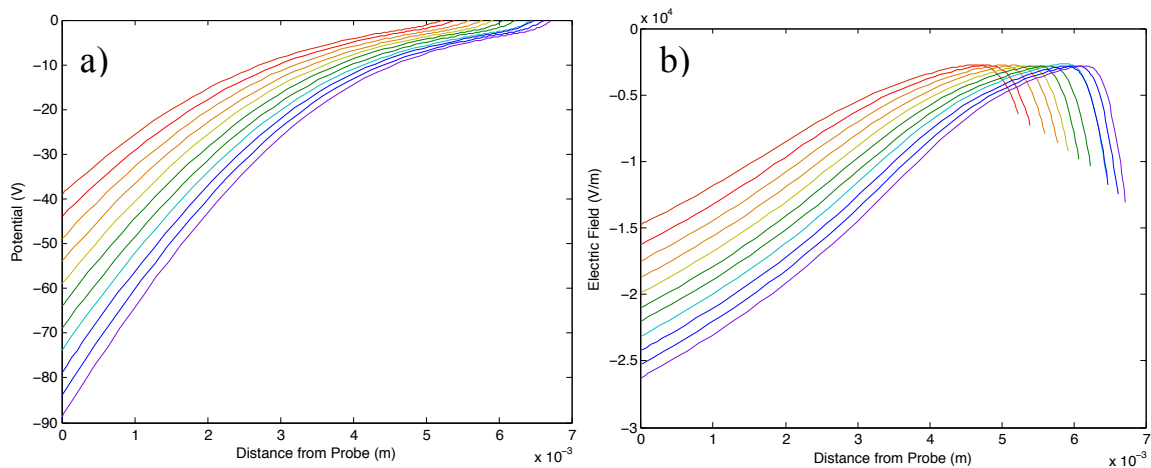


Figure 51 – a) Electric potential (relative to the plasma potential) (b) and electric field as a distance from the probe as calculated from the negative derivative of the potential solved from Eqn. 5.11. The results are shown for a range of probe voltages from -5 V (red) to -55 V (violet) in steps of 5V.

Though the probe current is known, determining the change in the densities of the plasma is not a straightforward calculation. Ionization is not often discussed in the literature for GEC plasma experiments. At a large (in magnitude) negative potential, the probe can stimulate ionization (by attracting the ions and repelling the electrons), or the plasma can adapt to the change through an adjustment to the ionization rate. Because a formula for plasma ionization has previously been derived (Chen 2006) when ambipolar

diffusion can be applied, an adaptation of this was employed. As discussed previously, electrons leave the plasma first, producing a positive bulk plasma potential in the steady state. This implies that quasineutrality is not a valid assumption, and this is confirmed by Langmuir probe measurements of the bulk. Under almost all conditions, the ion density is greater than the electron density. Since standard ambipolar diffusion derivations assume quasineutrality, the equations used in Chen (2006) had to be slightly modified. The key point of ambipolar diffusion is that fluxes to the lower electrode must be equal in the steady state. Allowing differing initial bulk densities, results in the following sheath electric field,

$$E = \frac{D_i \nabla n_i - D_e \nabla n_e}{\mu_i n_i + \mu_e n_e}, \quad (5.12)$$

where D_s represents the diffusion coefficient for species s , defined as kT_s/mv . This electric field model was first applied to the conditions of the vertical oscillation experiment described in Section 5.2 to determine validity with the results, shown in Figure 52. Since the electric field calculated by Eqn. 5.12 resulted in one very similar (near the dust levitation heights) to the successful electric field model applied in Section 5.2, it was used to estimate the ionization at the higher system power employed in this experiment. Although the methods developed in the previous experiment to find the sheath edge electric field only apply at lower power, E_0 was still assumed to be 2,800 V/m. This should not create problems in this experiment since the ion and electron plasma densities in the sheath do not change significantly with E_0 (as can be seen in Figure 40). The ionization formula (again modified to allow differing bulk densities)

$$\frac{\partial n}{\partial t} - D_1 \nabla^2 n_e - D_2 \nabla^2 n_i = Q_d(z) \quad (5.13)$$

is applied to estimate the bulk ionization where Q_d is the density change per second, and the new diffusion constants are defined as

$$D_1 = \frac{\mu_i n_i D_e}{\mu_i n_i + \mu_e n_e}, \quad D_2 = \frac{\mu_e n_e D_i}{\mu_i n_i + \mu_e n_e}. \quad (5.14)$$

Without the probe inserted in the system, the density does not change with time, so the first term of Eqn. 5.13 is zero. These results are plotted in Figure 52, and show that the change in plasma density due to probe current is insignificant (a few orders of magnitude less) when compared to the plasma ionization. Therefore, any change in electron density at the dust is most likely due to the local repulsion from the probe, not a change in ionization.

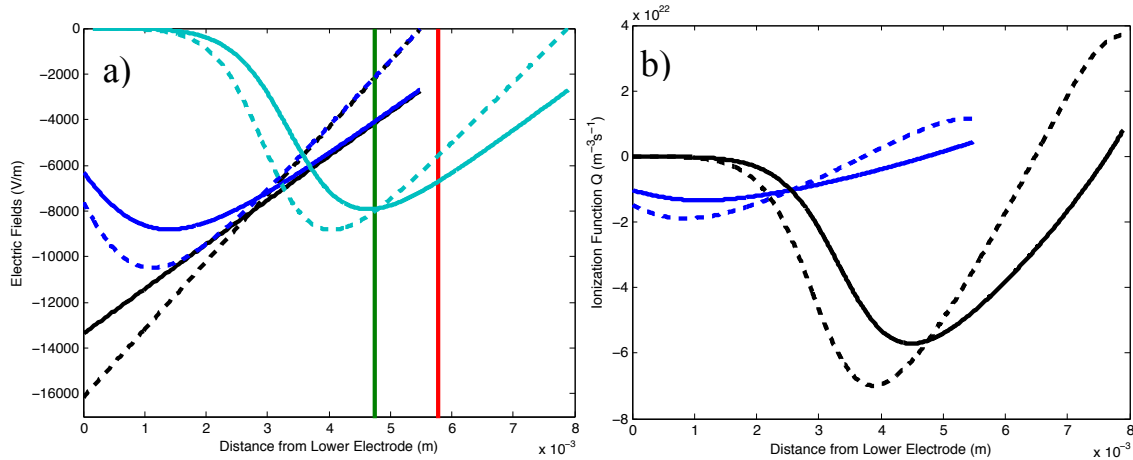


Figure 52 – a) The sheath electric fields found in the vertical oscillation experiment (black) are superimposed with results from ambipolar diffusion (blue for vertical oscillation parameters). The teal line is the field calculated using ambipolar diffusion for the 10 W, 100 mTorr parameters used for the negative probe potential induced cavities (with no sheath edge electric field). The dashed lines assume an electric field at the sheath edge of 0 V/m. Dust equilibrium positions are shown as vertical lines for the vertical oscillation experiment (green) and the comparison cavity conditions (red). b) The result of the ionization function Q_d (Eqn. 5.13) is shown for the vertical oscillation experiment (blue) and the comparison conditions for the cavity experiment (black). All lines end at their respective sheath edges.

Given the derivation of ambipolar diffusion provides appropriate results, the steady state plasma particle flux may now be calculated. This then provides the framework

needed to study the number of particles that impact the lower electrode per second. Since the entire cell (including the upper electrode) is grounded, it can be assumed the majority of plasma ions stream toward the negatively biased lower electrode, even though electrons are likely to be collected on all surfaces. Nevertheless, to justify the claim of large ionization, a substantial flux must be leaving the plasma in order that the plasma densities remain constant in the steady state. Figure 53 shows the approximate number of neutral gas atoms that are ionized per second, and the approximate number of ions/electrons that hit the lower electrode (1% of the plasma electrons for the conditions which produce the cavity). Results for the point at the sheath edge are most accurate because the change in the electron temperature from the bulk is not known. The flux of particles in the sheath multiplied by the cylindrical cross-sectional area between the electrodes gives the number of particles that flow per second. The 10 W, 100 mTorr case for nonzero E_0 finds a value in the bulk plasma of 1.3×10^{17} ionizations per second, with 2.2×10^{13} plasma particles incident upon the lower electrode per second. The number of ions flowing toward the lower electrode at a given height increase toward the central region of the sheath because they have been accelerated, but decrease toward the lower electrode where the species densities decrease (they must recombine or be redirected away from the lower electrode through collisions). This could be further studied by analyzing the current to the lower electrode.

5.3.3 Natural Cavities

Several theories have previously been proposed to explain the formation of natural cavities (Paeva 2004, Hu 2010, Paeva 2005, Goree 1999). Samsonov and Goree

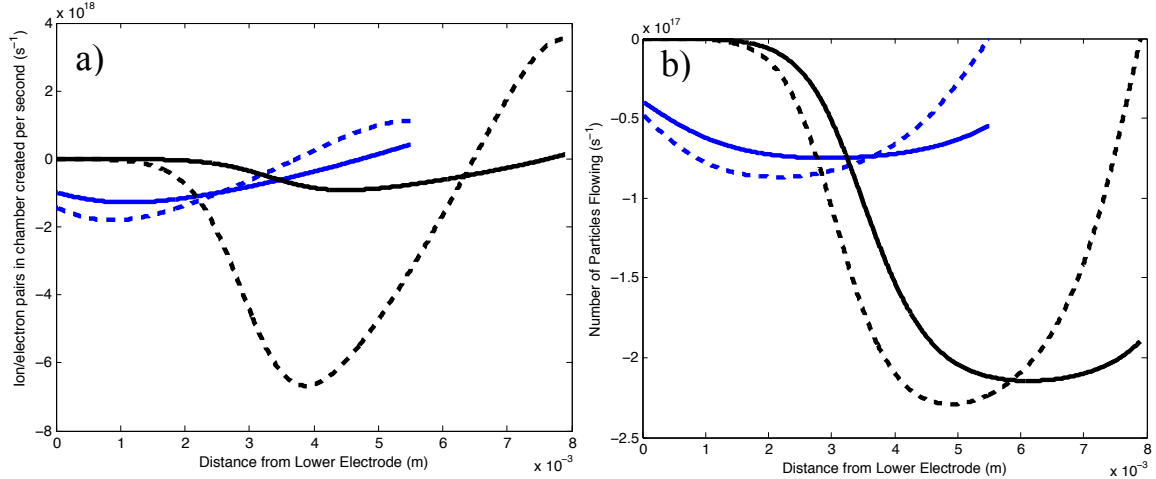


Figure 53 – a) Ionization rate and (b) number of particles flowing in the sheath as a function of distance from the lower electrode. Ionization rate is estimated by multiplying the ionization function Q_d (Eqn. 5.13) by the plasma volume. The dashed lines assume an electric field at the sheath edge (E_0) of 0 V/m, and the solid lines have $E_0 = 2800$ V/m. The blue lines relate the results for the conditions of the vertical oscillation experiment (Section 5.2), and the black for the negative probe potential-induced cavities.

proposed that at high powers (≥ 100 W), natural cavities are produced due to an instability caused by a local change in ionization created by electron depletion from the plasma to the dust cloud (i.e., Havnes parameter of 1-2) (Samsonov 1999). The total number of electrons in our plasma equals $n_e V = n_e A_e \Delta S = 2.1 \times 10^{14}$, where A_e is the area of the electrode and ΔS is the plasma width (from sheath edge to sheath edge), which is much greater than the total number of electrons on the dust, 4.6×10^6 (calculated using the electron density and particle number for a pressure of 300 mTorr shown in Table 5). Given this and the fact that we have an open system, electron depletion to the dust may be considered to be negligible.

Natural cavity formation has also been attributed to other mechanisms. Recently, Hu et al. through numerical simulation identified an increased central radial electric field, and a reduced central radial confinement as one possible cause, although they did not consider ion drag (Hu 2010). Alternatively, Paeva et al. included radial ion drag due to

the curvature of the sheath edge, but did not include the reduced confinement (Paeva 2004). Later numerical modeling results including a flat-bottomed cutout, used for horizontal confinement in all experiments, confirmed a non-zero radius of curvature for the sheath edge (Paeva 2005).

In the present work, natural cavity formation is explained by analyzing the potential energy of the dust particles. This offers an advantage over the model in Section 5.3.2, which cannot be used without a probe to find the electric field in the cavity. The potential energies involved include the interparticle repulsive (PE_r), the ion (PE_{ion}), the thermophoretic (PE_{therm}), and the confinement (PE_{conf}). PE_r is given by

$$\sum_{dust} \frac{Q^2}{8\pi\epsilon_0 r_d} e^{-r_d/\lambda_D}, \quad (5.15)$$

where r_d is the separation between each pair of particles. PE_{ion} is determined from the radial component of the ion drag force (Eqn. 3.35) of the streaming ions. PE_{therm} is estimated from the force of the radial temperature gradient. PE_{conf} is calculated from the gravitational potential energy difference between levitation heights for particles inside and outside the electrode depression (see Table 5). Since PE_r , PE_{ion} , and PE_{therm} direct particles parallel to the lower electrode while gravity acts perpendicularly on them, the only radial escape for a particle is to move upward, out of the cutout, making energy rather than force the more useful quantity to examine. Coupling these with flattened confinement, the potential energies produced are sufficient to generate the observed natural cavity sizes, which will be shown by finding the minimum of their sum.

A number of changes occur as pressure is increased. The interparticle potential energy decreases initially due to a decrease in charge, but increases again primarily

Table 5 – Experimental parameters found for natural cavity conditions. The radial ion drag is listed as a percentage of the gravitational force on a dust grain of radius 4.45 μm . The zero point is defined as the radial distance at which the horizontal confinement potential energy was found to be zero before increasing quadratically in order for the location of the minimum potential energy to equal the average particle distance from the electrode center (see Fig. 10). Energies are listed as totals for all particles. The screening length and plasma densities are reported at the dust levitation height.

Parameter	Pressure (mTorr)				
	300	400	500	600	700
System Power = 10 W					
Particle Number	451	423	393	323	311
Sheath Edge (mm)	4.2	3.3	3.1	3.0	3.0
Dust Height / Sheath Edge (%)	64	69	64	56	45
Sheath Shift (μm)	280	310	330	360	390
Confinement Energy (10^{-12} J)	3.1	3.0	2.8	2.4	2.3
Ion Density (10^{-15} m^{-3})	1.3	1.4	1.2	1.0	0.8
Electron Density (10^{-15} m^{-3})	0.7	1.0	0.7	0.4	0.1
Electron Temperature (eV)	8.7	8.8	9.0	9.3	9.0
Mean Free Path (μm)	160	120	90	73	61
Screening Length (m)	660	580	700	960	1500
Dust Charge (10^4e)	10	8.8	8.1	8.2	8.6
Repulsive Energy (10^{-14} J)	4.9	3.2	3.5	3.2	4.3
Radial Drag (%)	0.24	0.24	0.25	0.28	0.31
Zero Point (mm)	6.3	7.0	7.5	7.9	8.0

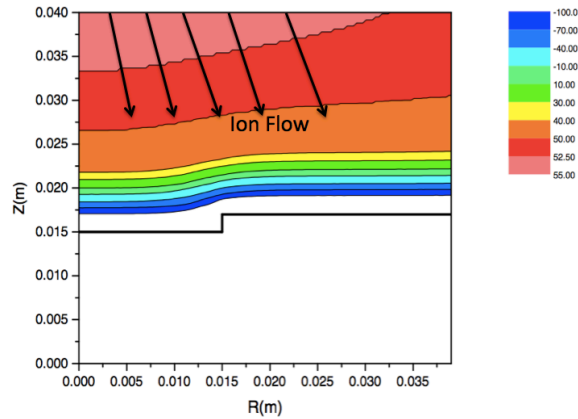


Figure 54 – Simulation result by Paeva et al. (2005) with added lines perpendicular to the first contour line denoting the direction of the ion flow. In the current experiment, an analogous radial component of the ion drag force is calculated based on the sheath edge curvature found from plasma emission. Near the lower electrode inside the cutout, the contour lines exhibit flattening, which is modeled for horizontal confinement for the first time below.

because of an increase in areal density of the dust (Figure 55). The sheath edge and the levitation height of the particles also decrease. The levitation height decreases linearly, while the sheath edge (defined by the levitation height of 0.46 micrometer nanoparticles (Samarian 2001)) asymptotically approaches a minimum value. A formula for a collisional sheath width derived by Sheridan et al. (1991) agrees with the experimentally determined sheath edge. The dust particle number decreases (Table 5) with increased pressure, signifying that PE_{conf} is exceeded by the sum of other potential energies. The horizontal confinement potential has typically, as a first approximation, been assumed to be parabolic (Zhang 2010). At higher pressures, as the particles approach the lower electrode, the amount of plasma between the electrode and dust is too thin to provide a smooth horizontal electric field transition all the way to the electrode center, due to the discontinuous electrode surface (from high outside the cutout to low inside). This confinement flattening reduces the total outward force required to form natural cavities.

The ratio of the equilibrium dust height to the sheath edge position (shown in Table 5) was found to decrease from 69 to 45 percent as the pressure increased from 400 to 700 mTorr. The slight increase from 300 to 400 mTorr can be explained by the small increase in plasma densities over the same pressures, despite the levitation height decreasing. The mean free path and screening lengths for each pressure are also reported in Table 5.

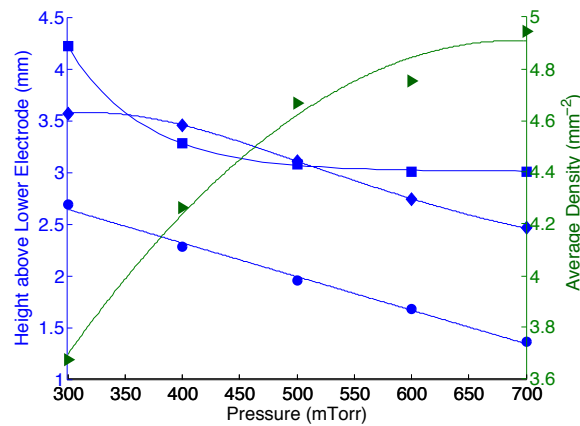


Figure 55 – Characteristic heights as a function of pressure, including the equilibrium levitation height of the dust (circles), the sheath width defined by Sheridan et al. (1991) (diamonds), the sheath edge found from the equilibrium levitation height of 0.46 micrometer diameter particles (squares), and the average areal density of the dust (triangles). All points besides the areal density refer to the left axis.

The curvature of the sheath edge can be determined by examining the intensity of the plasma glow. As shown in Figure 56, the curvature becomes more pronounced at higher pressures as the sheath width decreases and the plasma and the particles move closer to the lower electrode. This provides an added level of complexity; not only does the dust get closer to the lower electrode with increased pressure, but sheath curvature increases as well. It is typically assumed that ions flow in a direction perpendicular to the sheath edge; the average radial component of the ion flow was found by $(\Delta S_e - \Delta S_0)/R$, where ΔS_e is the sheath width at the cutout edge, ΔS_0 is the sheath width at the cutout center, and

R is the radius of the cutout. In order to analyze the radial ion drag, vertical image profiles of small regions (300 microns wide and the height of the image) at the center of the electrode cutout and at the cutout edge were used to determine the sheath edge, defined for this analysis to be the height at which the plasma intensity decreases by a factor of 1/e from the maximum intensity (Beckers 2011). The difference in sheath width ranged from 0 to 400 μm as pressure increased from 200 to 700 mTorr (see Table 5) as $\Delta S \propto P^{1/2}$, the same functional relationship as for the cavity size. The levitation of nanoparticles could not be used for determination of the sheath edge at these pressures because the plasma emission intensity increased to such a degree that the nanoparticles could no longer be distinguished.

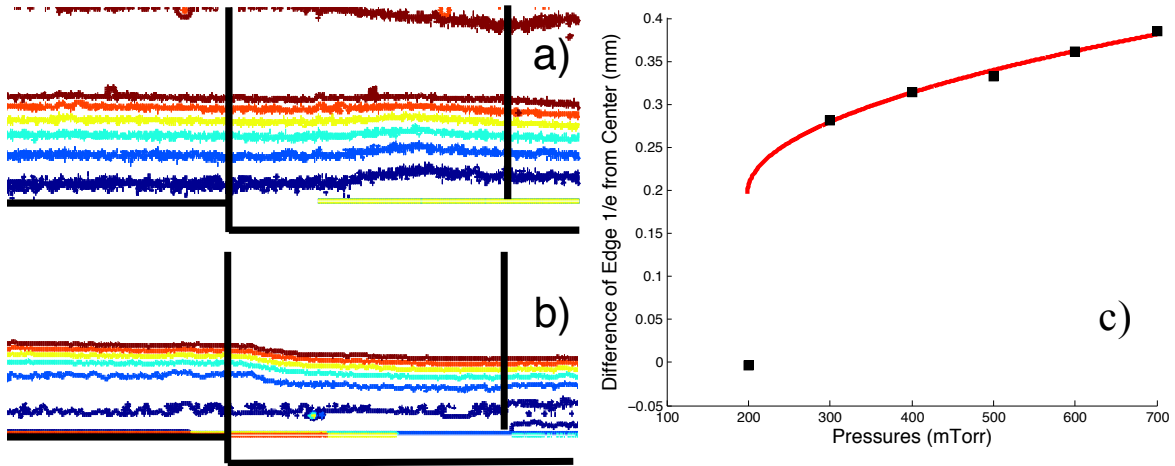


Figure 56 – Plasma intensity profiles for 200 mTorr (a) and 700 mTorr (b) with vertical lines showing the cutout edge (left) and the cutout center (right). The difference in the 1/e point between the cutout center and cutout edge was found to increase with pressure (c). The black squares represent the raw data, and the red fit line is of the form $\Delta S \propto P^{1/2}$, which best models the abrupt closure of the cavity at 200 mTorr.

The most significant contribution to natural cavity formation comes from thermophoresis. Land et al. recently provided a numerical simulation, which modeled the

plasma particles as a fluid and included dust grain dynamics for the conditions used in this experiment (Land 2010). They found an outward radial force on the dust. The thermophoretic force was calculated through estimation of the change in temperature between the cutout center and edge from the model results and scaling the plasma dimensions in the thermophoresis simulation (Land 2010) to this experimental plasma volume size in this experiment. It was found to be nonzero above a pressure of 100 mTorr, although the model is not applicable below this pressure. Therefore, a thermophoretic force is not significant for the conditions discussed in Sections 5.2 and 5.4, where the pressure was 100 mTorr. For intermediate pressures the force was approximated from a linear fit, and its corresponding potential energy determined by taking the integral of its dot product with the unit tangent vector of the confinement.

To model the flattening of PE_{conf} , the gravitational potential energy was set to zero up to a particular radial distance, referred to as the “zero point.” The confinement potential was then increased quadratically, since this provides the simplest (linear) restoring force that increases toward the cutout edge. The zero point was adjusted until the minimum of the total potential energy matched the experimental average annular radius of the dust in the ring, which monotonically increased in size with increased pressure. Decreasing the plasma power decreases the cavity size, so the zero point will drop to 0 mm at lower powers, reducing horizontal confinement to a parabolic potential well, a model that was assumed by Zhang et al. (2010) for 1 W. The end point of the horizontal confinement potential energy was set to the gravitational potential energy found from the height of the cutout in addition to the shift of the sheath at the cutout edge ($F_g \times (D + \Delta S_e - \Delta S_\theta) = 7.5 \times 10^{-15}$ J for 700 mTorr, where D is the depth of the electrode depression). By

considering the average annular radius (effectively the radial center of mass), the repulsive potential energy between dust grains could be ignored. Additionally, the radial component of the interparticle repulsion becomes less significant as the pressure increases due to a decrease in the annular width.

The horizontal confinement depends on the vertical dust position (the shape of the potential well is a function of height), so the dust lattice density is of interest. The areal dust density increases with pressure, as the cavity increases in size, which compresses the dust against the horizontal confinement. The dust density also reaches a maximum limit, as dust is pushed out of the confinement after the total potential energies of the outward forces exceed the inward forces.

The average dust density as a function of the radial position is also a point of interest in both gravity and microgravity experiments. On the ISS, the highest dust density occurs near the void edge (Figure 2 in Lipaev et al. (2007)), because the ion drag at the void edge increases toward the center of the void faster than the electric field decreases. However, for a natural cavity, the maximum density is found at the outer edge of the dust annulus, as shown in Figure 57. This effect occurs because the total potential energy grows faster at the outer edge of the cavity (due to the electrode cutout edge) rather than toward the cutout center, as shown below.

Since the mean free path of the ions decreases with pressure, a collisional model was employed to calculate the dust charge, and in turn the ion drag, at each pressure shown in Table 5 (see Section 3.2.1). The mean free path and resultant average potential energy per particle is shown in Figure 58. Although the radial ion drag force increases with an

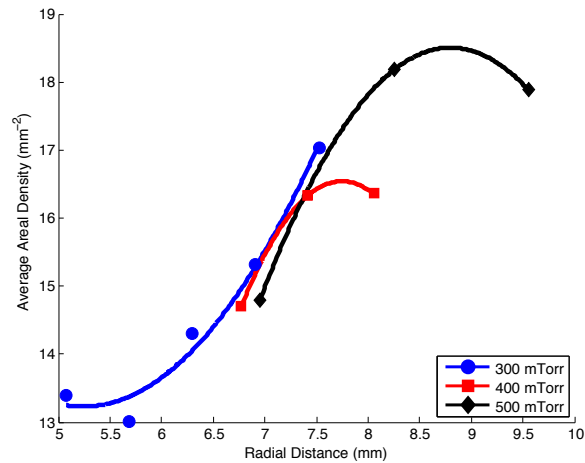


Figure 57 - The average areal dust density as a function of the radial position, where radial distance of dust particles is binned and the interparticle distance averaged. The dust density increases as a function of the radius until it reaches a maximum near the outer edge of the annulus.

increase in pressure (see Table 5), the increase of the thermophoretic force and flattening of the confinement provide contributions of much greater magnitude.

In summary, natural cavities form under increased pressure and/or power, and in a single horizontal layer in the sheath under gravity. They are particularly important to consider as background contributions to probe-induced cavities when those are generated at conditions favorable for natural cavity emergence.

5.3.4 Positive Probe Potential Induced Cavities

As shown in Figure 47, cavity size also grows when the probe potential is increased above the floating potential. One difference from negative probe potential-induced cavities is the time required to establish the cavity; positive probe-induced cavities form in seconds as opposed to almost immediately for negative probe biases. This is primarily due to the fact that a positive probe takes time to absorb electrons (since this is limited by

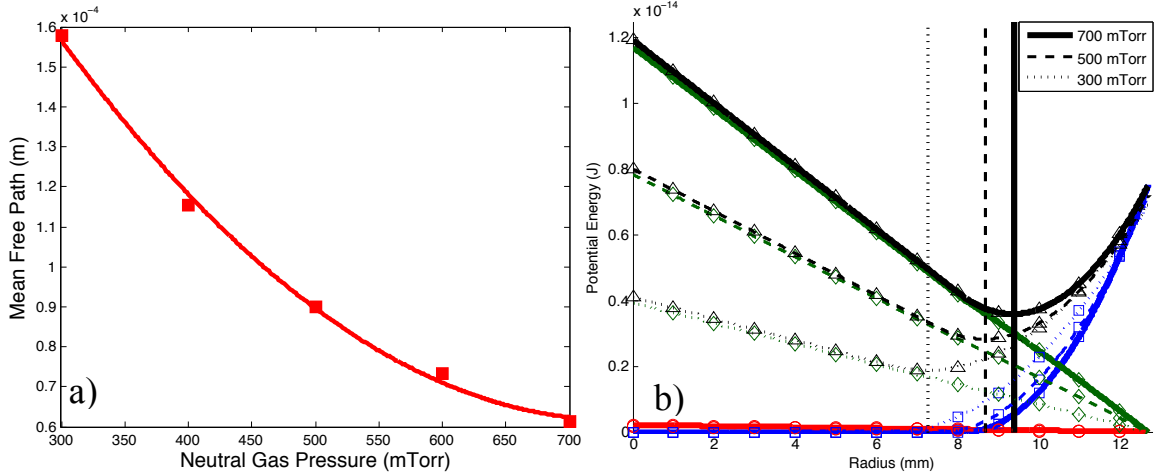


Figure 58 – a) Ion mean free path as a function of neutral gas pressure, and b) the potential energy of the average particle in a dust crystal having a naturally formed cavity for various pressures. The (black) vertical lines show the average annular radii, which coincide with the minima of the total potential energy (black triangles). Contributions to the total potential energy include the potential energy of thermophoresis (green diamonds), radial ion drag (red circles), and horizontal confinement (blue squares).

the plasma-probe surface area) and establish an outward directed ion flow, whereas a negative probe rapidly evacuates the less massive electrons from the a probe region, diminishing shielding and allowing the repulsive electric field to affect the dust. This is corroborated by the finding that current to a positive probe is much greater than that for negative potentials; this implies such cavity growth occurs through an independent mechanism from those described in the previous section. Experimental data also shows that the sheath edge directly beneath the probe is raised upon application of positive probe potentials, which may provide another explanation (Harris 2013). The radial expanse of that perturbation was not considered previously, but due to plasma shielding the radial extension of sheath perturbation *is* expected to be limited, and thus modeled in the manner below.

Because ions in plasma are not typically considered to have a Boltzmann distribution around a charged particle (Gurnett 2005) and electrons are not mobility limited (i.e., the

drift velocity is negligible (Lieberman 2005)), the reverse of the negative probe electric field model (combining linear continuity (Eqn. 5.9), energy conservation (Eqn. 3.22), and a Boltzmann electron distribution (Eqn. 3.2)) could not be applied. Therefore, as in the previous analysis of natural cavities, cavity growth was modeled using a potential energy analysis ($PE = PE_{\text{sheath}} + PE_{\text{conf}} + PE_{\text{ion}}$). As a first approximation, it was assumed the potential energy from the raised sheath edge decreases with distance as

$$PE_{\text{sheath}}(r) = E_0 e^{-0.5(r/\sigma)^2}, \quad (5.16)$$

where r is the radial distance, σ is a parameter quantifying the extent of the shielding, and E_0 is the gravitational potential energy of a dust particle above the electrode center. In this case, the shielding parameter, σ , was chosen such that the location of the minimum total potential energy matched the average experimental radial dust position (σ was found to equal 4.7 mm for all cases), and $E_0 = mgh$, where h (the dust levitation height) was found from the oscillation amplitudes of the dust at corresponding positive probe potentials as in Harris et al. (2013).

Since system pressure and power were held constant the horizontal confinement potential energy, PE_{conf} , was fixed. Its characteristic zero point was found by extrapolating the quadratic fit of the natural cavity zero points (listed in Table 5) to 100 mTorr, resulting in a value of 4.3 mm.

In this case, the potential energy due to the ion flow away from the probe, PE_{ion} , plays a significant role. Since the cavities formed are large compared to the shielding length, it is reasonable to assume that ions reach the sheath plasma potential at the equilibrium levitation height of the dust before impacting the dust. Therefore, energy conservation

may be used to find the ion velocity, and the continuity equation applied to calculate ion density and solve for the ion drag upon the dust.

The only remaining unknown parameter is the initial ion velocity at the probe, which will differ from the thermal velocity. In this case, the initial ion velocity was left as a free parameter and adjusted to fit the data, as shown in Figure 59. Although it increases from the thermal velocity by a factor of 10 at a probe potential of 55 V, this is still less than the Bohm velocity, which is larger than the thermal velocity by a factor of 13.5. At these potentials, an enhanced glow around the probe suggests new sheath formation, justifying the ion acceleration.

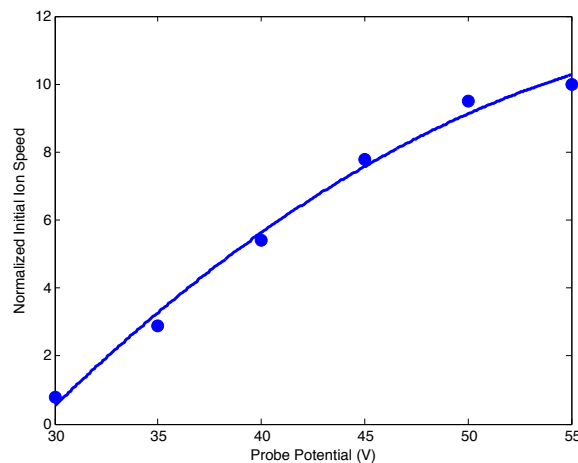


Figure 59 – Initial ion speed as a function of positive probe potential normalized to the equilibrium ion thermal speed at the dust levitation height. The line is a quadratic fit. The values are found by fitting the minimum of the total potential energy to match the average radial dust position.

The results of the potential energy calculations are shown in Figure 60. The ion drag force is found to decrease with increasing probe potential, but remains larger than the force from the raised sheath. However, the contribution from the raised sheath grows nonlinearly and becomes more important at higher probe potentials.

5.3.5 Annular Dust Waves

Analysis of the annular dust waves (Section 4.3.5) after the creation of a negative probe potential induced cavity required the use of a cylindrical wave equation,

$$A = \frac{A_0}{\sqrt{r}} \cos(kr - \omega t + \delta) \quad (5.17)$$

where A_0 is the amplitude constant, r is the radial distance, k is the wave number, ω is the

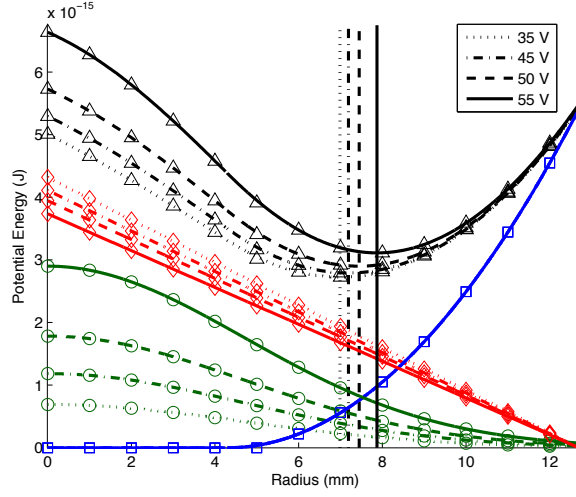


Figure 60 - Potential energy plot for positive-probe-potential induced cavities. The (black) triangles indicate the total potential energy, with contributions from the repulsive energy due to the raised sheath edge (green circles), outward ion drag (red diamonds) and the horizontal confinement (blue squares). The vertical lines indicate the minimum in the total potential energy, which coincides with the average experimental radial position of the dust.

wave frequency, t is time, and δ is the phase shift. Eqn. 5.17 has a coefficient ($A_0/r^{1/2}$) that ensures energy is conserved (Harker [http:// www.cmmmp.ucl.ac.uk](http://www.cmmmp.ucl.ac.uk)). This was applied to the experimental radial waves by fitting the amplitude parameter and radial position to the particle motion in the space-time plot (shown in Figure 61) nearest the probe. The wave number was found by finding the distance (λ) from one peak in the space-time diagram in the radial (shown vertically in plot) direction until it reaches the next peak. $2\pi/\lambda$ yields the wave number, k . The same parameters were used for the particle farthest

away from the probe. However, this resulted in a phase and amplitude mismatch, as shown in Figure 61.

The solution required superposition of a reflected wave, which has a different amplitude A_0 based on the amount of reflection. Even though there are no hard radial barriers for direct particle collisions, the plasma can still absorb and reflect some of the

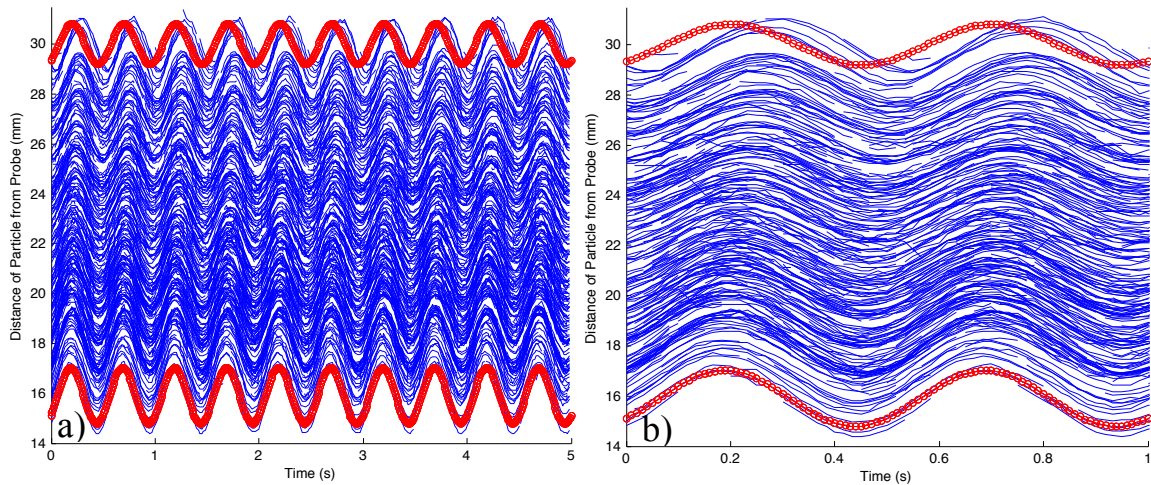


Figure 61 – a) Space-time diagram of the radial distance of the dust particles (blue) from the probe during potential oscillation. The outgoing cylindrical wave (red) is fit to the particle nearest the probe (bottom) and then solved for the radius of the particle farthest from the probe (top). b) A view expanded in time shows more clearly that the calculated wave does not match in either phase or amplitude.

outgoing wave energy. Given this data exhibits only a partially reflected wave implies wave implies the superposition is not uniform in terms of its time evolution, which can best be seen with a 3D plot, as shown in Figure 62.

The phenomenon of radial resonance can also be modeled using a superposition of the outgoing and reflected cylindrical waves (Eqn. 5.17). By adjusting the reflected incoming cylindrical wave amplitude to equal the outgoing amplitude, and reducing the

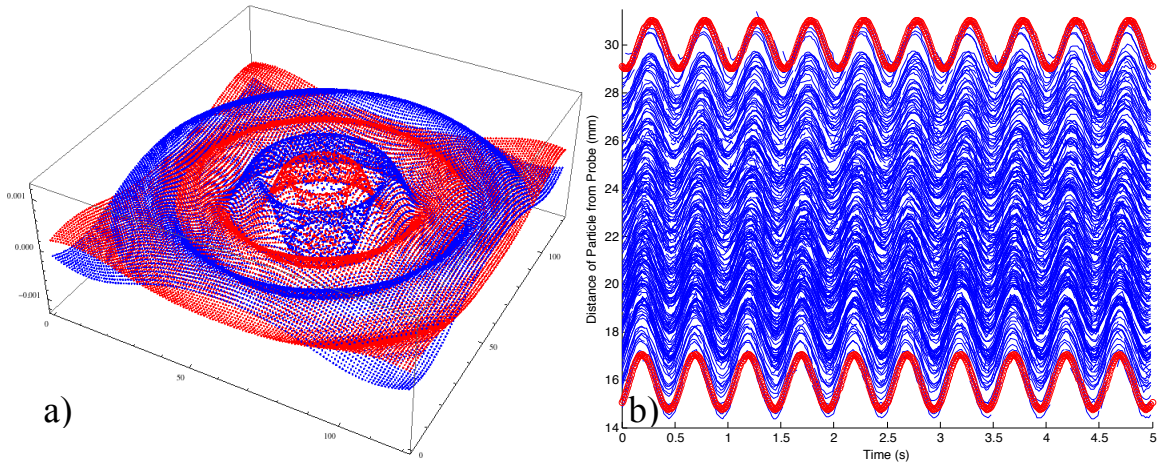


Figure 62 – Radial dust grain motion in a single layer crystal driven by a central probe under an oscillating potential. a) By superimposing a reflected cylindrical wave (red), the phase and amplitude found from b) the experiment (blue) were matched to that predicted by the cylindrical wave equation. The reflected wave had 76% of the outgoing wave amplitude, and a phase shift of 1.0 rad.

phase difference of the reflected wave (to 0.1 radians), appropriate conditions were discovered which allowed intermediate particles to remain stationary. This was confirmed by the fact that particles on either side of this line oscillated precisely out of phase with each other. A representative plot of this effect is shown in Figure 63, with the boundary lines (nearest to and farthest from probe) fit to experimental data. Note that the position of radial resonance is not in the center of the boundary lines.

5.3.6 Conclusions for Cavity Formation

Cavity formation in complex plasma crystals occurs in several forms: induced by a probe charged negatively relative to the plasma, naturally, and induced by a positively charged probe. Each of these is produced due to a different mechanism.

Negative probe potential induced cavities may be explained by an electric force directed outward from the probe, balanced against an inward directed ion drag. This was

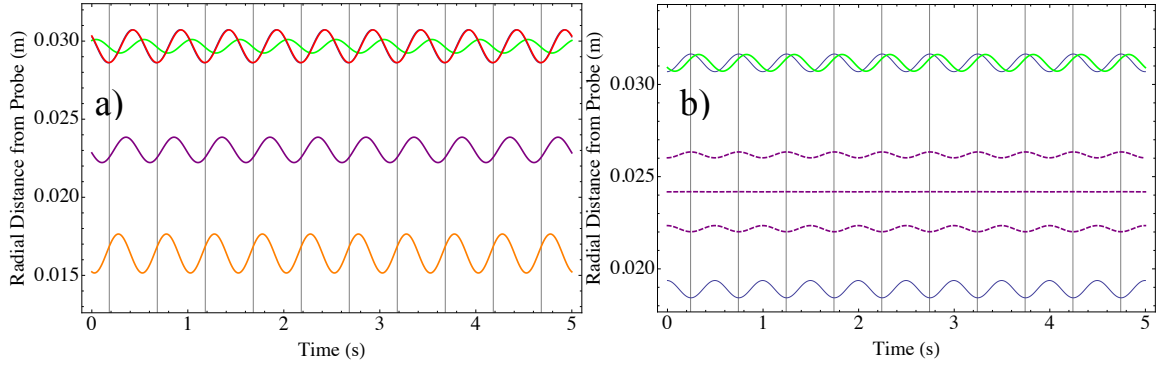


Figure 63 – a) Radial dust position versus time for the annular dust wave discussed in Figure 62 and b) for radial resonance. The orange, red, and blue lines are all fits to data. The green lines show the reflected wave amplitude at the mean position of the particle farthest from the probe. The purple lines show the superimposed wave amplitude at intermediate radial positions. For radial resonance, the amplitude of the particle does go to zero at the mean radial position of 24 mm, and grain motion at positions 2 mm in both directions are also shown further demonstrate the transition (dashed purple lines).

shown in a previous model for probe-induced cavities in a DC plasma (Thomas 2004). In the RF case, interparticle forces must be included since the annular width of the dust ring (see Figure 30) is greater than the diameter of a single grain. The electron density at the dust was found to vary over the potential range (Figure 47), becoming larger as the probe potential became more negative. This provides a method to calculate the equilibrium parameters (electron density, screening length, and charge) in the sheath at the dust height by linearly extrapolating the results to the floating potential. Current to the probe varied linearly with probe bias (Figure 47), and consequently the variation of cavity size was linear (Figure 45).

Natural cavities were found to be produced by an outward thermophoretic force and a small radial ion drag, coupled with flattening of the horizontal confinement potential at higher pressure (Figure 58). The radial ion drag was identified by employing plasma emission analysis, which showed a small shift in the sheath height between the center and edge of the electrode cutout used for horizontal confinement. The depth of the

depression of the electrode was not found to alter overall cavity size (Figure 28). This may be because the sheath curvature increases in such a manner to counteract the increased horizontal confinement of the deeper well. All natural cavities examined here differed from the voids observed in ISS experiments in that the maximum radial dust density occurred near the cavity edge (Figure 57) rather than at the outer dust crystal edge. Low power laboratory cavities were also shown to exist in the sheath and not the bulk, making them more than simply 2D analogs of the voids found in microgravity.

Positive probe potential-induced cavities are perhaps the most interesting of the three cases because their existence was not expected. Although a positive probe attracts negatively charged dust, other effects often override that attraction. From the experiment in Section 5.2, the sheath edge was found to be raised by a positively charged probe. This forms a central cylindrical potential energy barrier (Figure 60), which repels the dust. Simultaneously, the positive probe repels plasma ions, generating an outward radial ion drag force. While ion drag played little role for the negative probe potential-induced cavities, it constitutes the largest generating force in this case.

Finally, waves in cavities were produced by oscillating the probe potential with the probe tip located at the plane of the dust crystal. A phase difference of 1.0 rad was found between the oscillations of the dust nearest to and farthest from the probe. Under appropriate conditions, a resonance was shown to occur (for the endpoints) where dust along an intermediate radial distance in the crystal remained stationary (i.e., at a node of a standing wave). Both cases were modeled with a superposition of incoming and outgoing radial waves using the cylindrical wave equation.

Future work should employ additional electrode depression depths and radial sizes to further examine whether the natural cavity size remains unaffected; examination of the average particle potential energy with a decrease in power to test for a reduction to a parabolic confinement potential; and utilize a polydisperse dust distribution to observe how the dust size affects cavity radius as well as whether this provides a method for radial dust separation by size.

5.4 Dust Chain Waves

5.4.1 Introduction

In this section, the dust chain waves described in Section 4.4 are analyzed. First in Section 5.4.2, the dispersion relation originally derived for longitudinal waves in a horizontal dust chain is applied to new data for vertical dust chain waves. This provides the ability to find the average grain charge and screening length over the chain, the first such determination for vertical dust chains formed with the use of a glass box. Next in Section 5.4.3, a dispersion relation derived for transverse waves in horizontal dust chains is adapted by inclusion of restoring force due to streaming ions and fit to transverse wave data in the vertical direction. In Section 5.4.3, the harmonics of the longitudinal waves in a vertical chain are examined. Finally in Section 5.4.4, a previously derived wave model assuming a continuous string is employed that includes neutral drag, reaffirming the usage of a coupled oscillator model for dust chains. Parameters required as inputs are taken from experimental results of the model in Section 4.4.

5.4.2 Longitudinal Chain Wave Dispersion

One dimensional longitudinal chain waves have previously been used in the horizontal direction to measure both the grain charge and screening length. For these experiments, horizontal chains were formed using a lower electrode cutout plate with a slit or other asymmetric confinement. Driving the chain at one end of this cutout allows wave propagation. Although many of the fundamental parameters change when examined for a vertical chain, in this experiment, the same dispersion relation that was derived for waves in the horizontal direction was successfully applied,

$$\omega^2 = \frac{4\beta(a)}{m} \sin^2 \left(\frac{ak}{2} \right) \quad \beta(a) = \frac{Q}{2\pi\epsilon_0 a^3} e^{ak_d} \left(1 + k_d a + \frac{k_d^2 a^2}{2} \right) \quad (5.18)$$

where ω is the driving frequency, a is the mean interparticle distance, k is the wave number, k_d is the inverse screening length, and β is defined as shown (Melandso 1996).

Figure 64 shows the results of the application of Eqn. 5.18 to the data described in Section 4.4.2. The agreement is remarkable given that plasma densities, screening length, sheath electric field, and even temperature can change in the vertical direction. Although the grain charge may change depending on the particle's position in the vertical chain, this dispersion relation is only sensitive to changes in the average charge. A second advantage of the method is that it does not require measurement of plasma densities, the sheath electric field, or position of the sheath edge. Using the technique described, it was found that the grain charge is $44,000e^-$ for the antisymmetric chain wave generated at 2.4 W system power, $48,000e^-$ for the symmetric chain wave generated at 3.0 W, and $58,000e^-$ for the standing chain wave at a power of 3.9 W. Notice that the charge increases with power, which is understandable since ionization increases with power. The screening length was found to be $1000 \mu\text{m}$ in all cases. However, it must be

understood that the model is much more sensitive to changes in charge compared to changes in screening length, as exhibited in Figure 65.

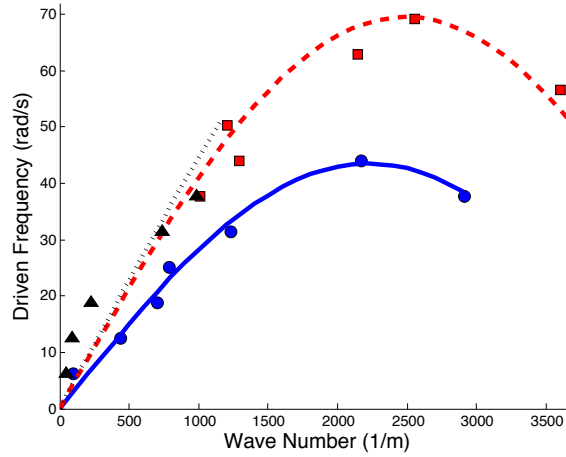


Figure 64 – Dispersion relations found experimentally (points) and theoretically (lines) for the antisymmetric (blue circles), symmetric (black triangles), and standing (red squares) longitudinal waves.

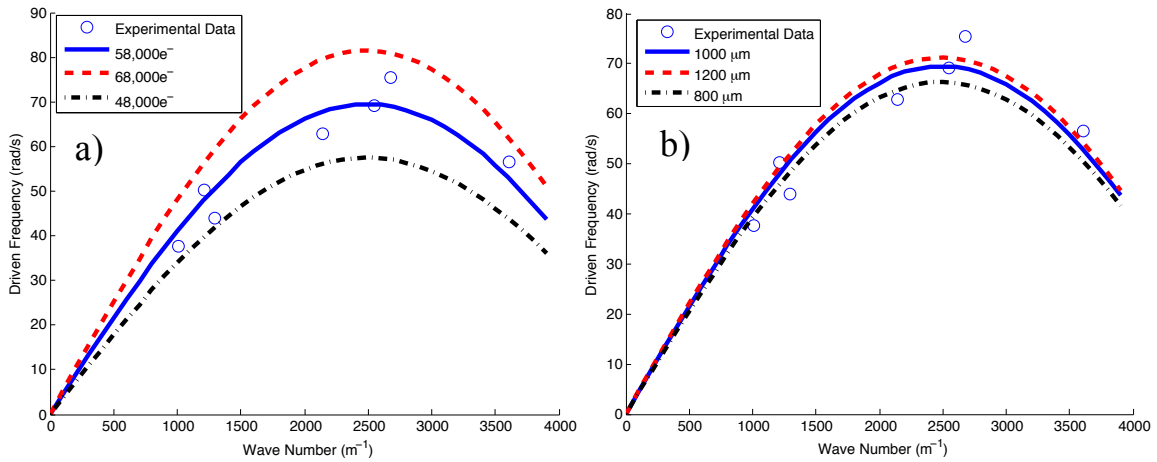


Figure 65 – Dispersion relation for the standing wave for a) various values of charge and b) screening length. Given a 20% change for each quantity in both directions, the dispersion relation is shown to be more sensitive to changes in charge.

5.4.3 Transverse Chain Wave Dispersion

Similar to the method described in Section 5.4.2, a dispersion relation for a horizontal chain of particles with waves propagating transverse to its axis (vertically) has been previously derived (Misawa 2001). Unfortunately in this case, blind application of the relationship derived for transverse waves (horizontal motion) in vertical dust chains does not admit a credible fit to the data. In this case, a major difference between the previously studied horizontal chains and the vertical chains in this experiment is ion streaming. This effect is much more important for the transverse waves in vertical chains because the movement of the particles in the horizontal direction allows the ions to pass, affecting lower particles. Lapenta (2001) has shown that ions curving around upstream particles can impact the dynamics of lower particles, with this is resulting in a much more uniform effect for a longitudinal wave. He also analyzed particles moving perpendicular to the chain and found a restoring force, which was also examined by Piel (2011). The basic premise is that if the downstream particle is displaced slightly horizontally, ions on the opposite side of the direction of motion are lost by collection with the upstream particle, and so the ions impacting on the side of the direction of motion generate a restoring force. Piel found that ions that cross through the chain, deflected toward the chain axis by attraction to the upper particle, provide a force to the lower particle, which encourages return to the chain axis. Both effects are illustrated in Figure 66. Using Piel's data, the restoring force is found to first order to be linearly dependent on the distance from the chain axis. When adding this to the transverse chain wave dispersion relation, with a constant coefficient (A) to adjust the relative strength of this force versus

the restoration from the horizontal confinement provided by the glass box, the dispersion relation becomes

$$\omega^2 = \omega_{0,x}^2 - \frac{Q^2}{\pi\epsilon_0 d^3 m} e^{-d/\lambda_D} \left(1 + \frac{d}{\lambda_D}\right) \sin^2\left(\frac{kd}{2}\right) + Akd, \quad (5.19)$$

where $\omega_{0,x}$ is the horizontal resonant frequency and d is the interparticle spacing. A fit to Eqn. 5.19 is shown in Figure 67.

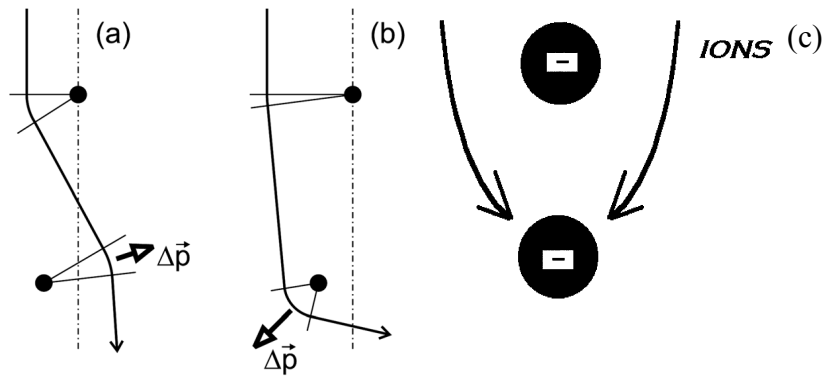


Figure 66 - Lower particle ion streaming forces (Δp is the change in momentum) through two mechanisms. The first mechanism comes from scattering ion drag (attraction) where an ion either (a) crosses over the axis, or (b) passes the lower, of two vertically aligned dust grains. The angles represent the Coulomb collision region for comparison between (a) and (b). Piel (2011) found over the range of parameters for the present experiment that (a), which restores the lower particle to the axis, is dominant over (b), which deflects it from the axis. The ion Mach number determines whether the total horizontal force favors (a) or (b). The second force comes from (c) collection ion drag, where ions collide with a downstream particle as they curve past the upstream particle (Lapenta 2001). Figures a-b) are reproduced from Piel (2011) and c) from Lapenta (2001).

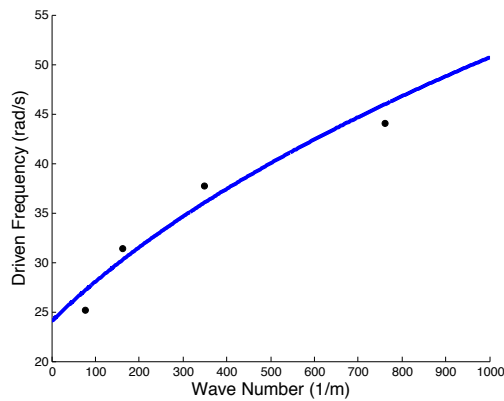


Figure 67 – Transverse chain wave dispersion results, data points are from experiment while the fit line is from Eqn 5.19.

While the resulting screening length found by the fit to Eqn 5.19 agrees with that found for longitudinal waves, the calculated grain charge (14,000e) does not agree with those found in Section 5.4.2. The reasons for this include the following. First, omitting direct collisional ion drag in the longitudinal wave analysis removes a form of vertical damping that may be compensated to maintain a fit to the data with an increased interparticle interaction, which would require an elevated charge. Second, greater oscillation amplitudes of the probe potential are required to generate the transverse waves in comparison to the longitudinal waves, potentially due to increased confinement from the glass box walls. This may drive nonlinear particle oscillations, overriding the linearity the dispersion relation derivations require. Third, despite the result from the asymmetric particle oscillation (Section 5.2) that ion drag alone is not enough to create asymmetric vertical dust oscillation, horizontal ion motion due to the off-center probe potential oscillating at higher amplitudes compared to oscillations discussed in Section 5.2 may drive this motion, requiring this force to be added to the model. Finally, it is possible that both charge predictions are correct, if the probe changes the charging process. Oscillations at higher probe potential oscillations during transverse wave stimulation leads to electrons moving at greater speeds.

5.4.4 Harmonics

Harmonics often play important roles in the identification of wave mode excitations. Therefore, Fourier transforms of the time domain of the particle oscillation were generated (Figure 68). For the longitudinal antisymmetric mode, the second harmonic has an amplitude (8 micrometers) that is 4% of the fundamental (200 micrometers). The subfrequency resolution was obtained by transforming multiple oscillation cycles

simultaneously. The ratio of harmonics to the fundamental may yield a quantification of either plasma or dust parameters, given a model (such as an analogy to second-harmonic generation seen with optics in nonlinear crystals (Franken 1961)) and further analysis. However, the mere observance of these harmonics enhances the argument that wave energy is being reflected from the bottom of the chain, which is assumed in the dispersion relation derivation (Melandso 1996).

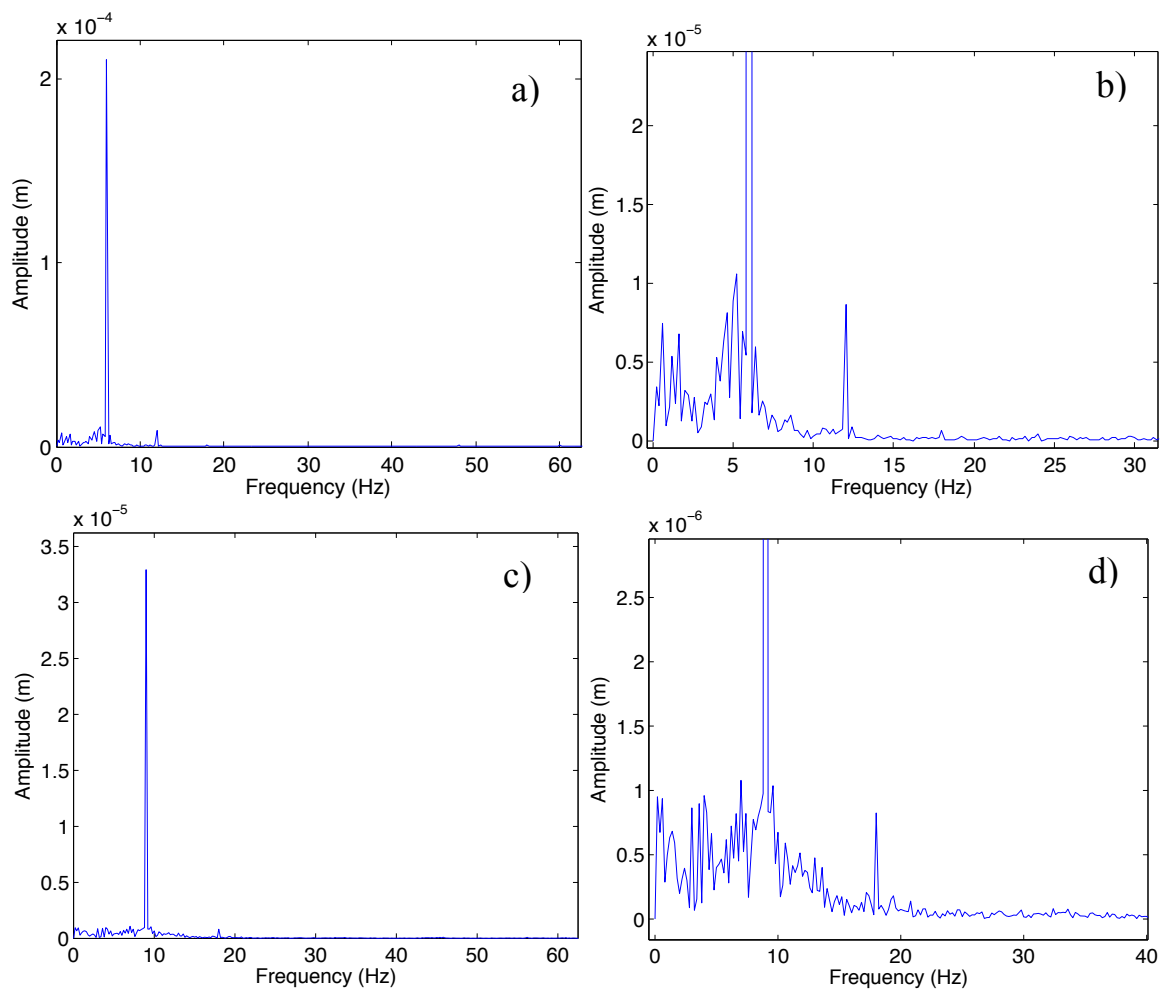


Figure 68 – Fourier transforms of the central particle's position as a function of time in an oscillated chain for a) the antisymmetric mode, showing the relative size between the fundamental frequency and the second harmonic. b) The enlarged plot shows that the third and possibly fourth harmonics are also present. c-d) For the central particle of the standing wave mode, the first harmonic is also clearly visible.

No harmonics were confirmed for the transverse chain wave mode. This may be due to the fact that the horizontal confinement is much stronger than the vertical confinement, which would damp the harmonics quickly. Considering that the chain formation only allows a single particle for a given height, this makes sense. However, the transverse mode required significantly greater probe potential oscillation to emerge, so it is also possible that the signal to noise ratio is just too low to discern the harmonics at present.

Given the experimental presence of the wave harmonics, it is reasonable to assume that inclusion of harmonics into the wave model would improve the results. Unfortunately, the RMS deviation between wave model prediction and experiment did not markedly improve, implying that harmonics are not important in generating the wave modes. Another parameter that was considered in wave model improvement was the spring constant amplitude, analogous to the tension of a string exhibiting wave motion. Initially assumed to be the same between all dust grains, it is reasonable that allowing these values to be independent could improve the prediction because the plasma densities change as a function of the height from the lower electrode. However, this adjustment also did not improve the model, leading to the conclusion that the “tension” does not change appreciably over the dust chain.

5.4.5 Neutral Drag in Chain Model

The final avenue of exploration involves the addition of neutral drag into the dust chain wave model. Because the typical eigenvalue/eigenvector analysis method is assumed to be in steady state, direct insertion of a loss of energy over time causes the waves to vanish. However, a formula has been derived to include drag,

$$q(x, t) = \sum_{r=1}^{\infty} \frac{2F_0 \sin\left(\frac{r\pi}{2}\right) \cos(\omega t - \delta) \sin\left(\frac{r\pi x}{b}\right)}{\rho b \sqrt{\left(\frac{r^2 \pi^2 \tau^2}{\rho b} - \omega^2\right) + \frac{D}{\rho} \omega^2}}, \quad (5.20)$$

where F_0 is the amplitude, δ is the phase shift calculated, ρ is the linear mass density of the chain, ω is the oscillation frequency, and b is the “string” length (Marion 1988). The results when applied to this experiment are very good, as shown in Figure 69. The experimental equilibrium positions are taken as inputs to Eqn 5.20, and F_0 was adjusted to provide the best fit to the data. The test on the model is then the relative amplitudes and phase differences, which match the data well. The reduced amplitude for the top and bottom particles of the antisymmetric mode as discussed in Section 5.4.1 is also seen in this model. The “tension” value is used from result of the model used in Section 5.4.1. The “string” length was adjusted for best fit to the data to be 16 mm for both cases shown in Figure 69.

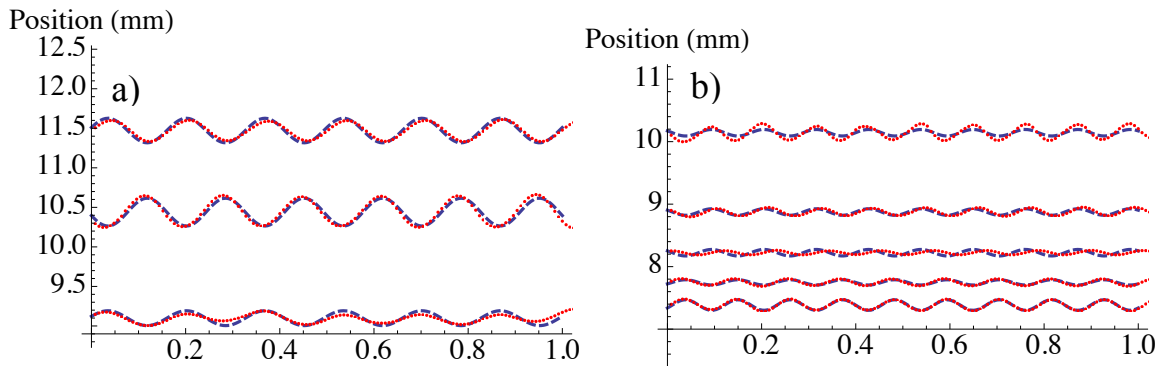


Figure 69 – Heights of individual dust grains (red dots) above the lower electrode located in a vertical chain versus time (in seconds) that is being oscillated longitudinally by the varying potential of a probe, superimposed with the results of Eqn. 5.20 (blue dashed lines), for a) the antisymmetric mode, and b) the standing wave mode.

5.4.6 Conclusions Drawn from Oscillation of Vertical Chains

Vertical dust chains have been shown to be extremely useful for measuring grain charge and plasma screening length when using a glass box for confinement. Through

oscillation of a probe's potential, longitudinal and transverse waves were produced. The longitudinal wave motion exhibited all of the theoretical wave modes for three masses oscillating on a string, under unique conditions. Dispersion relations used in describing horizontal chains were successfully adapted to vertical chains. Several experiments have employed an insulated glass box on the lower electrode, and this has posed a problem because charge collects on the glass box walls and can alter the plasma. As the glass box is required to create one-dimensional vertical dust chains through increased horizontal confinement, this experiment provides much needed measurements of charge and screening length. Most importantly, these values were obtained without using OML theory or needing to know where the sheath edge was located. Future studies could be improved by including the sheath electric field.

Improvements to the original chain wave model were discussed. Harmonics were found in the chain wave motion, though they had Fourier transform amplitudes of only a few percent of the amplitude of the fundamental frequency. However, these and independent "string" constants were found not to improve the fit of the original model. Neutral drag, given its potential importance at the pressures employed, was considered using an alternative formula. The fit was appropriate, further justifying the initial assumption that vertically aligned dust grains behave as coupled oscillators.

CHAPTER SIX

Conclusions

The experiments presented in this dissertation yield insight into plasma and dust parameters through the use of a powered, remote controlled, position adjustable, vertical probe. Dust is manipulated by variations in the applied probe potential. As the dust levitates below the bulk plasma, analysis of the dust motion allows analysis of the sheath conditions in both the horizontal and vertical directions.

In the initial experiment, oscillation of the probe potential probe with a positive bias generated an asymmetric vertical oscillation of a particle directly beneath the tip of the probe. The direct oscillation allowed determination of the neutral gas drag coefficient. It provided data used in a model of a linear sheath electric field that admitted calculation of grain charge and the first direct measurement of the electric field at the sheath edge, which was compared to previous theoretical estimates. This required a new application of the damped, harmonic oscillator Green's function. In this model, drag from the streaming ions in the sheath was included. The probe was found to modify the plasma by reducing the vertical extent of the plasma bulk and raising the sheath edge.

For the second experiment, the probe was lowered toward the plane of a dust crystal and a central cavity opened in the crystal. It was found that cavities appeared for both negative and positive potentials applied to the probe. Through a model for the electric potential involving differential equations previously applied to a DC experiment, equilibrium grain charge and electron density at the dust levitation height were found,

when the probe was biased negatively. With an increasingly positive bias, the cavity also grew, due to ion drag and the radial extent of the raised sheath edge effect found in the first experiment. By oscillating the probe potential at a positive bias, radial waves were observed. To clearly differentiate the probe's influence from cavity formation, it was removed and cavities formed naturally at the higher powers and pressures available in the reference cell. These were compared to cavities studied in another laboratory in addition to the International Space Station, and primarily explained by a radial thermophoretic force. Since the sheath decreases in width with an increase in pressure, dust levitate closer to the lower electrode, and the flat bottom electrode cutouts used to generate horizontal confinement cause a flattened confinement potential in a radially central region.

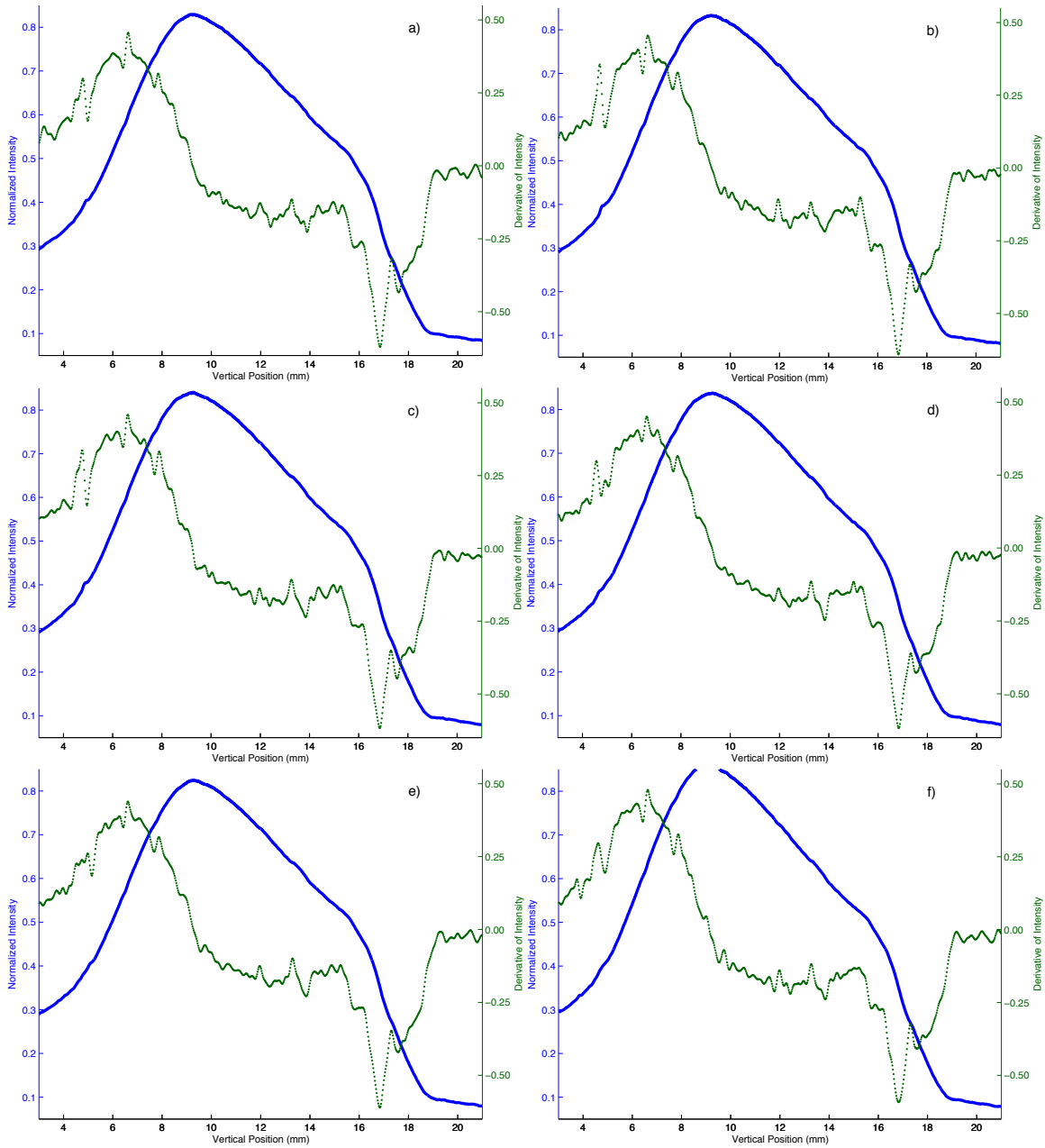
The final experiment employed vertical dust chains, formed by the addition of a glass box upon the lower electrode to provide horizontal confinement. At the appropriate system power and neutral gas pressure, a single chain was levitated. Oscillating the probe potential drove waves through the chain. All of the wave modes theoretically studied for three coupled oscillators were found in the dust chain waves at unique parameters of probe potential oscillation frequency, system power, and system pressure. Application of dispersion relations that were previously used for horizontal dust chains, parallel to the lower electrode, yielded reasonable values for the grain charge and plasma screening length. Since the glass box walls collect charge like all surfaces in plasma, this method is superior because it does not require plasma densities, the sheath electric field, or the sheath edge for its application.

As a whole, this project has opened new avenues of experimental analysis and produced independent measurements of quantities previously estimated such as neutral drag, grain charge, plasma screening length, sheath thickness, ionization, and the value of the electric field at the sheath edge. It has considered former models for cavity formation with a biased probe in DC plasma in addition to waves moving through single horizontal dust chains and adapted them to different conditions including a ring of dust particles surrounding a biased probe with an annular width greater than a single grain in a RF plasma and a vertical geometry for the dust particle chain waves. With a greater understanding of the forces and behavior of complex plasma, the ability to manipulate matter larger than but suspended within the basic plasma particles is enhanced, and the interaction between the two further elucidated, lending acumen to such diverse fields as semiconductor manufacturing and protoplanetary development.

APPENDICES

APPENDIX A

Extended Data



(continued)

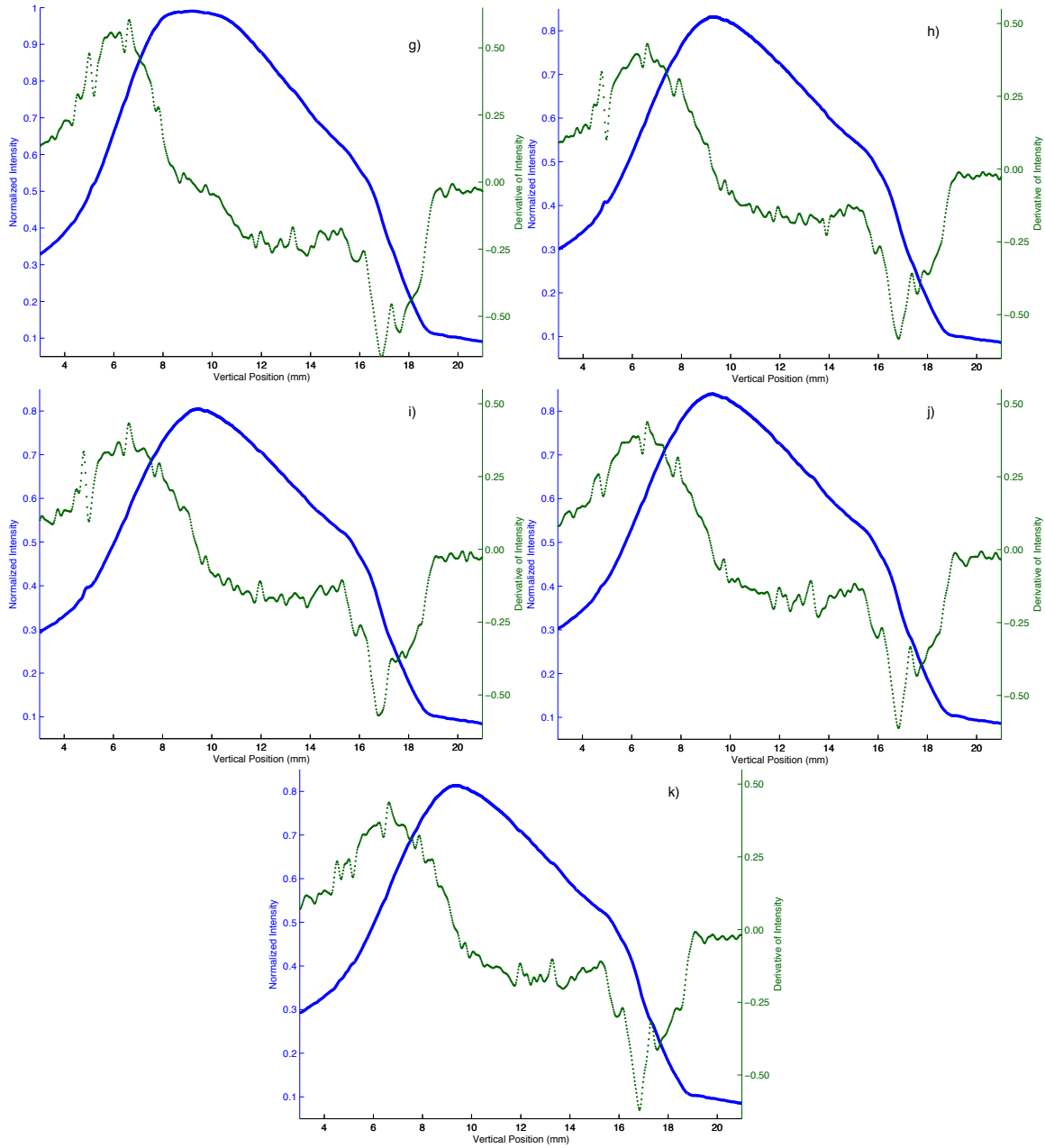
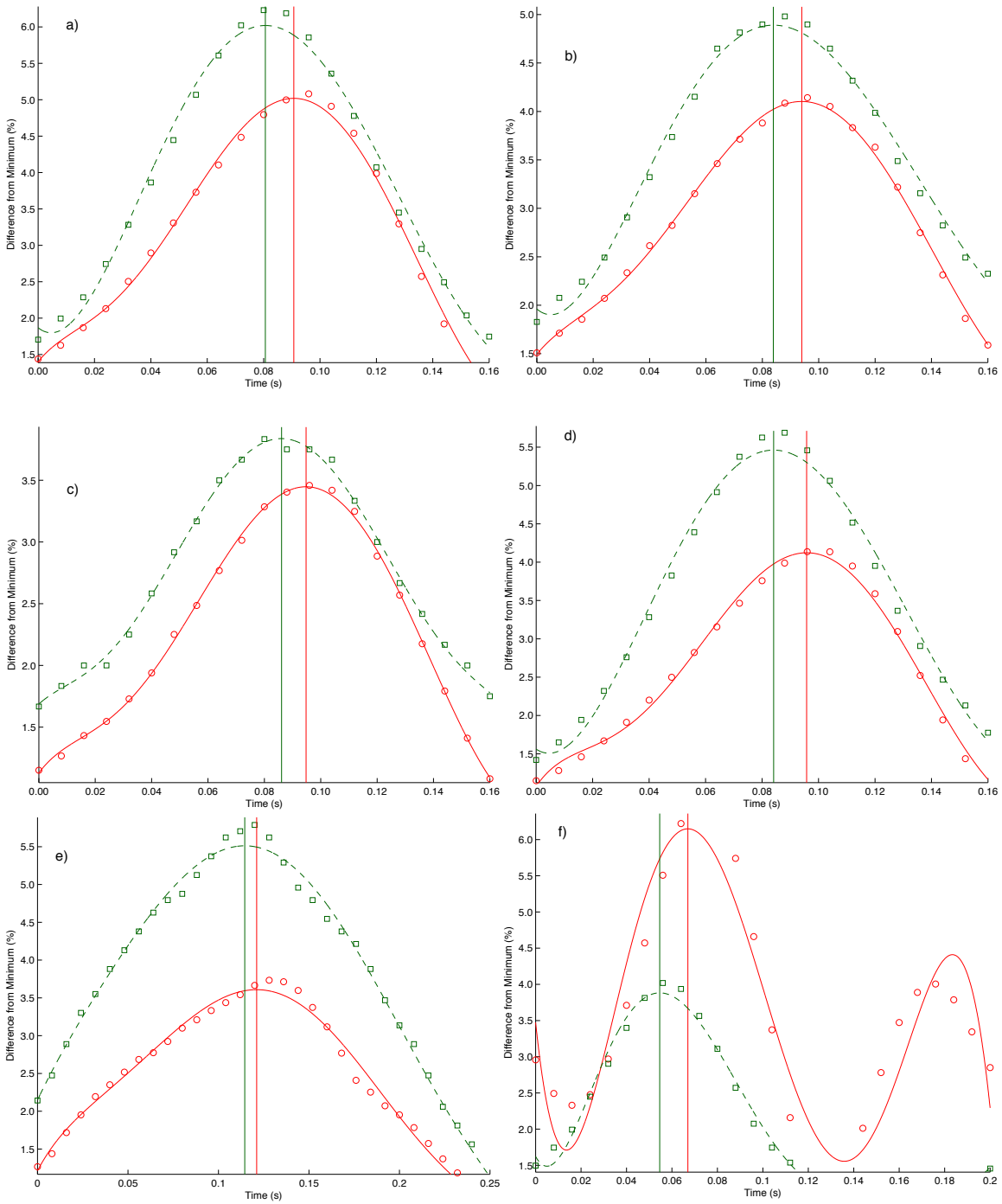
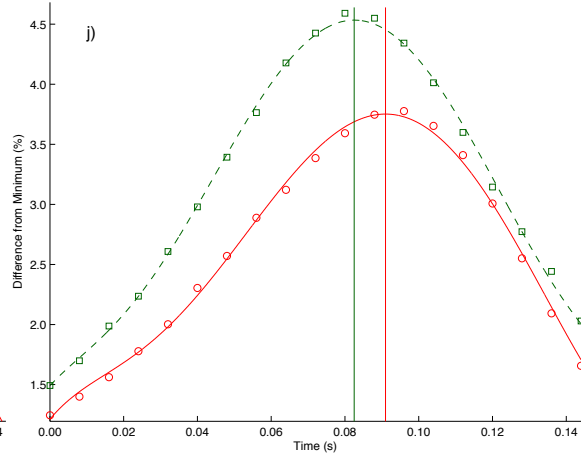
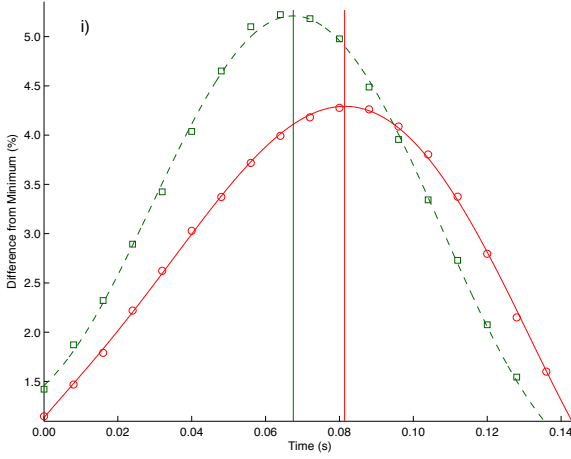
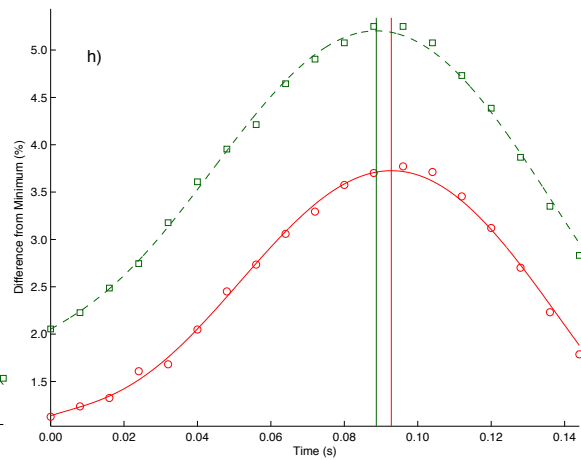
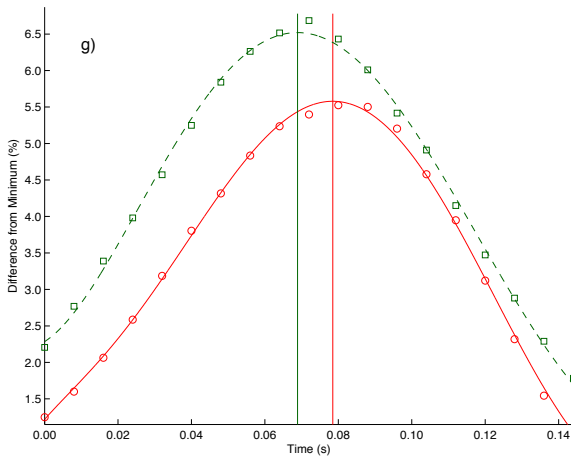


Figure 70 - Normalized optical emission intensity profile (solid blue line) of the plasma (Figure 14) averaged over the horizontal coordinate as a function of the distance above the lower electrode (where the upper electrode is located at $z=19$ mm). The derivative of the intensity (green dots) is superimposed with vertical lines indicating the levitation height of the dust (red dashed), the sheath edge (green dash-dot), the local maximum of the derivative emission intensity (dotted black), and the maximum of the intensity (solid blue). Plots are shown for a) 1.50 W, b) 90 mTorr, c) 45 V probe peak to peak (VPP), d) 65 VPP, e) 10 V probe bias, f) 1 Hz oscillation g) 5 Hz oscillation, h) 9 mm probe height, i) 11 mm probe height, j) -1 V DC bias, and k) -10 V DC bias.



(continued)



(continued)

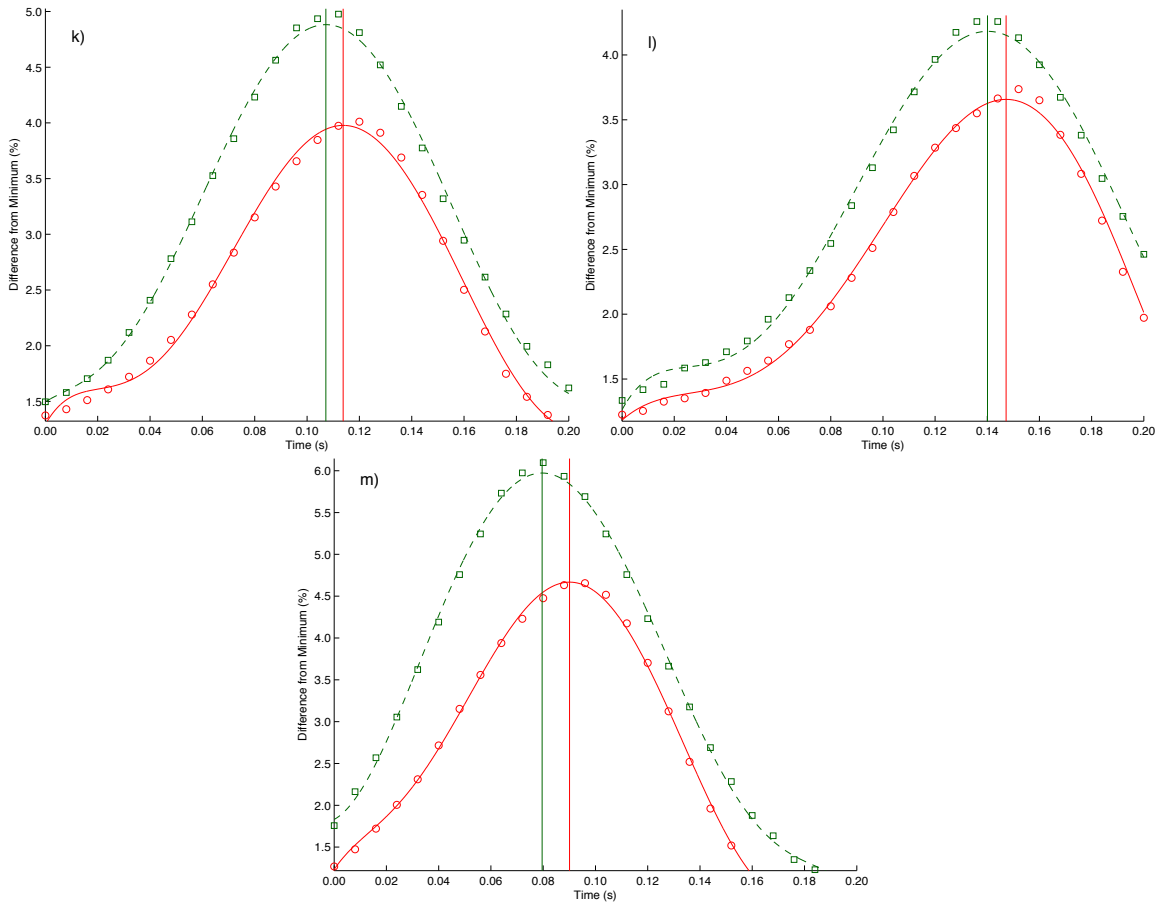
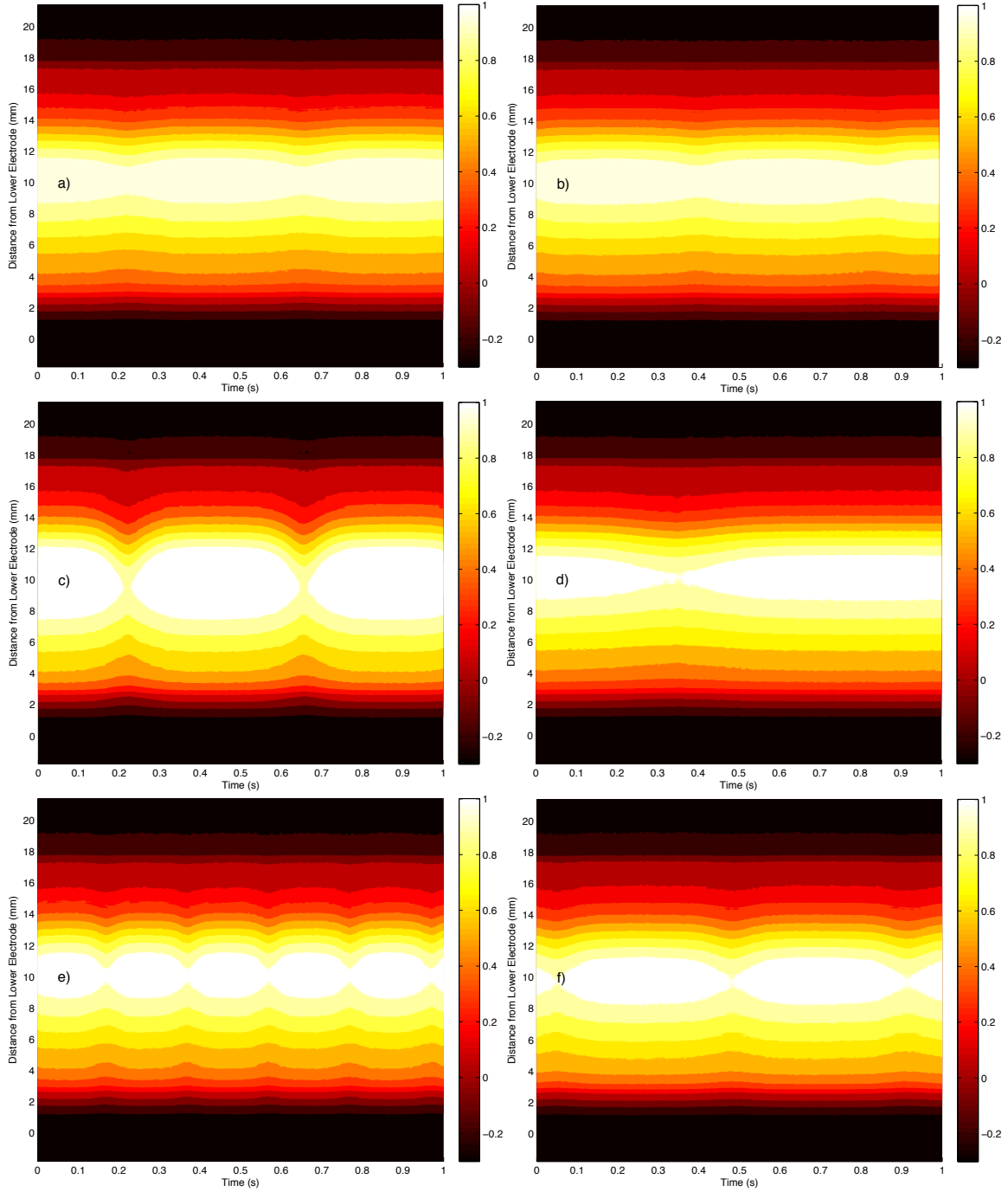
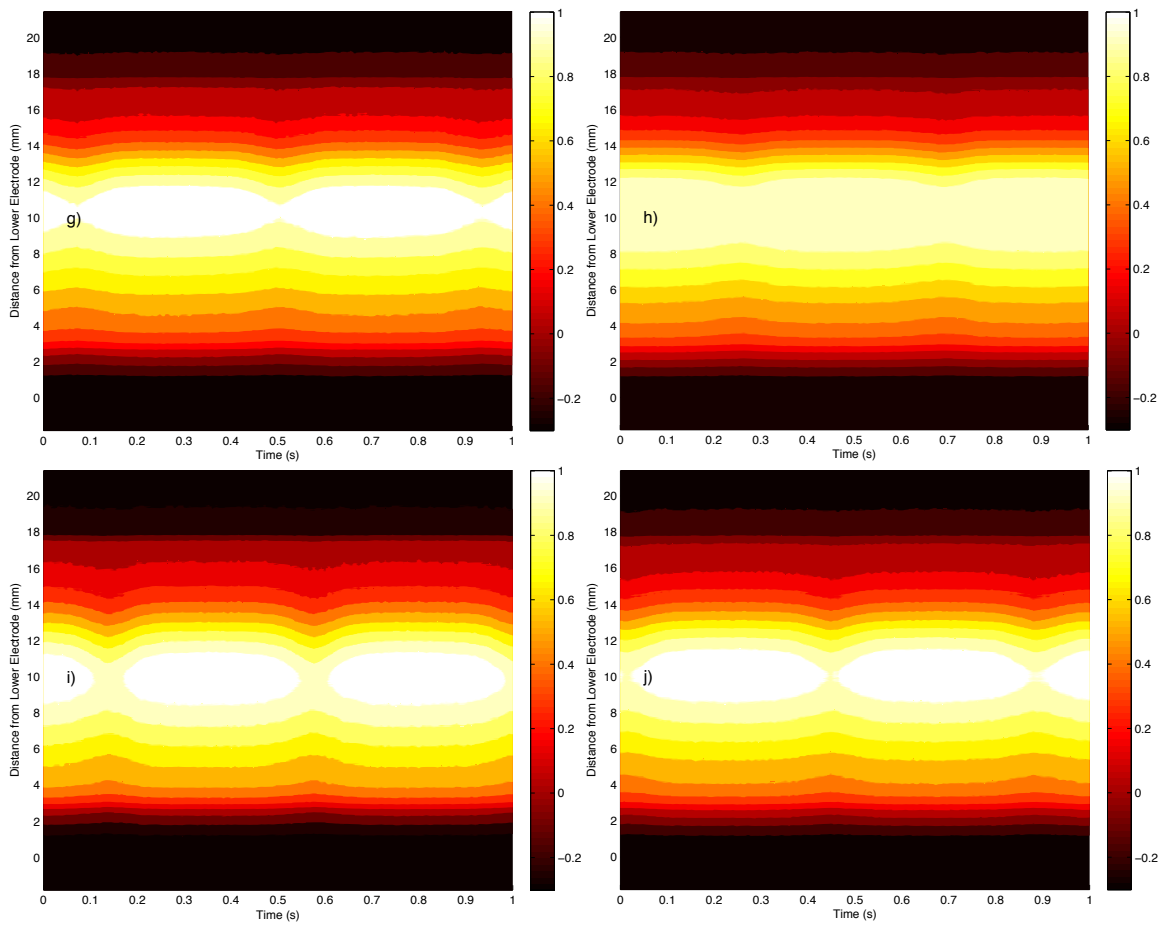


Figure 71 – Phase shifts between the sheath edge and particle position. The solid (red) line represents a polynomial fit to particle position (red circles) over time while the dashed line represents the fit to the sheath position (green squares). The vertical lines shown indicate the peaks of these fit lines illustrating the delay between maximum particle response and maximum sheath response. All values are shown as percentage differences from their respective minima for a) 0.75 W system power, b) 1.50 W, c) 90 mTorr, d) 45 V probe peak to peak (VPP), e) 65 VPP, f) 10 V probe bias, g) 30 V probe bias, h) 1 Hz oscillation i) 5 Hz oscillation, j) 9 mm probe height, k) 11 mm probe height, l) -1 V DC bias, and m) -10 V DC bias.



(continued)



(continued)

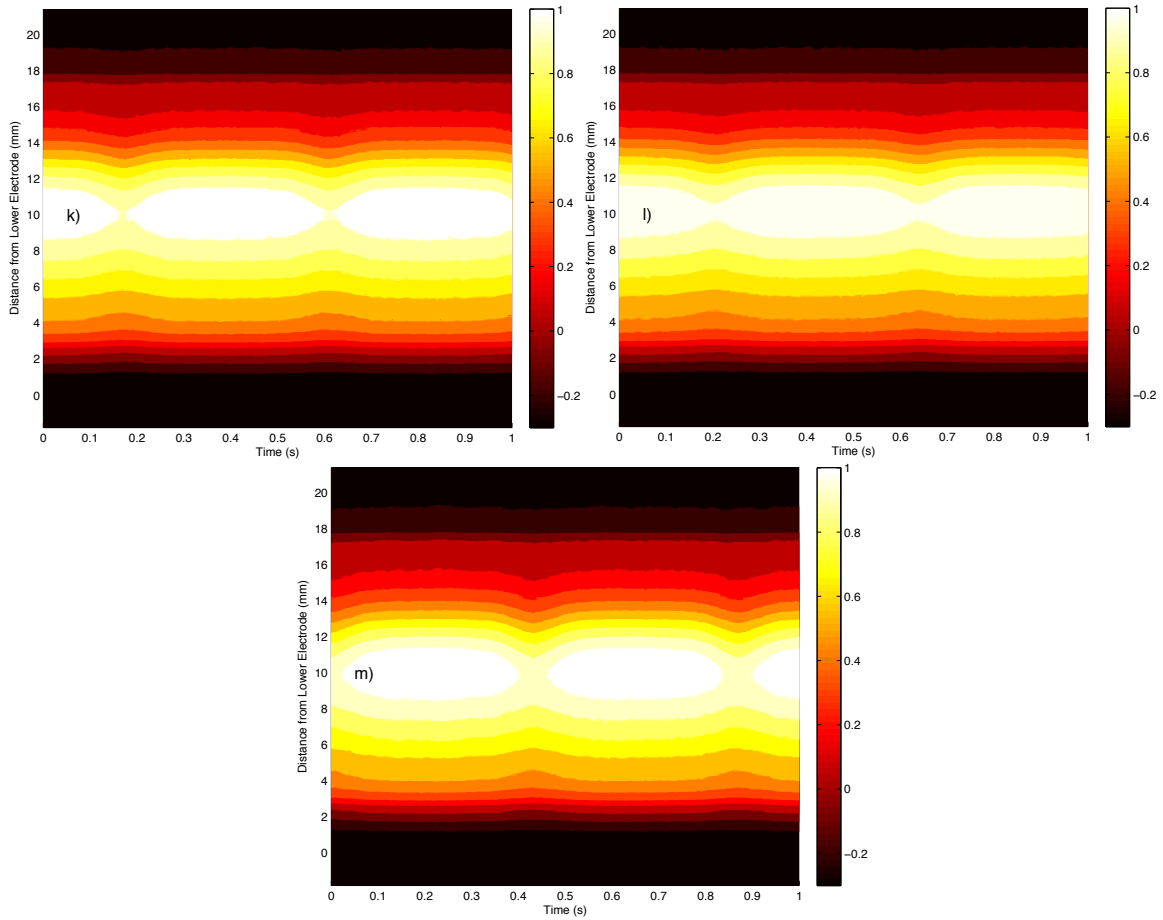
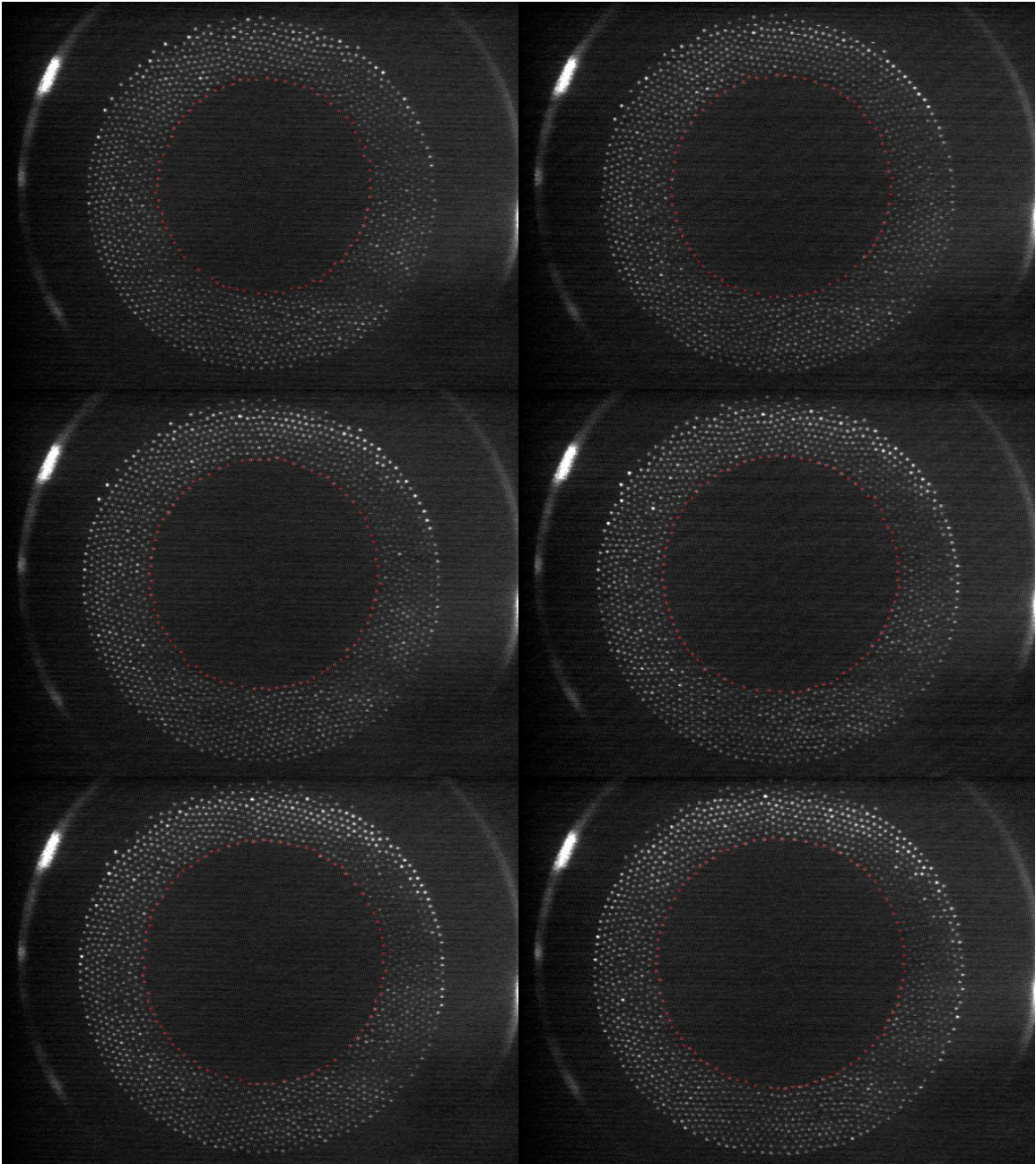


Figure 72 - Intensity space-time contour plots. The colorbar gives the intensity relative to the overall minimum, and normalized to the resulting maximum ($(I - I_{\min})/I_{\max}$). Plots shown are for the following conditions: a) 0.75 W system power, b) 1.50 W, c) 70 mTorr, d) 90 mTorr, e) 45 V probe peak to peak (VPP), f) 10 V probe bias, g) 30 V probe bias, h) 1 Hz oscillation i) 5 Hz oscillation, j) 9 mm probe height, k) 11 mm probe height, l) -1 V DC bias, and m) -10 V DC bias.



(continued)

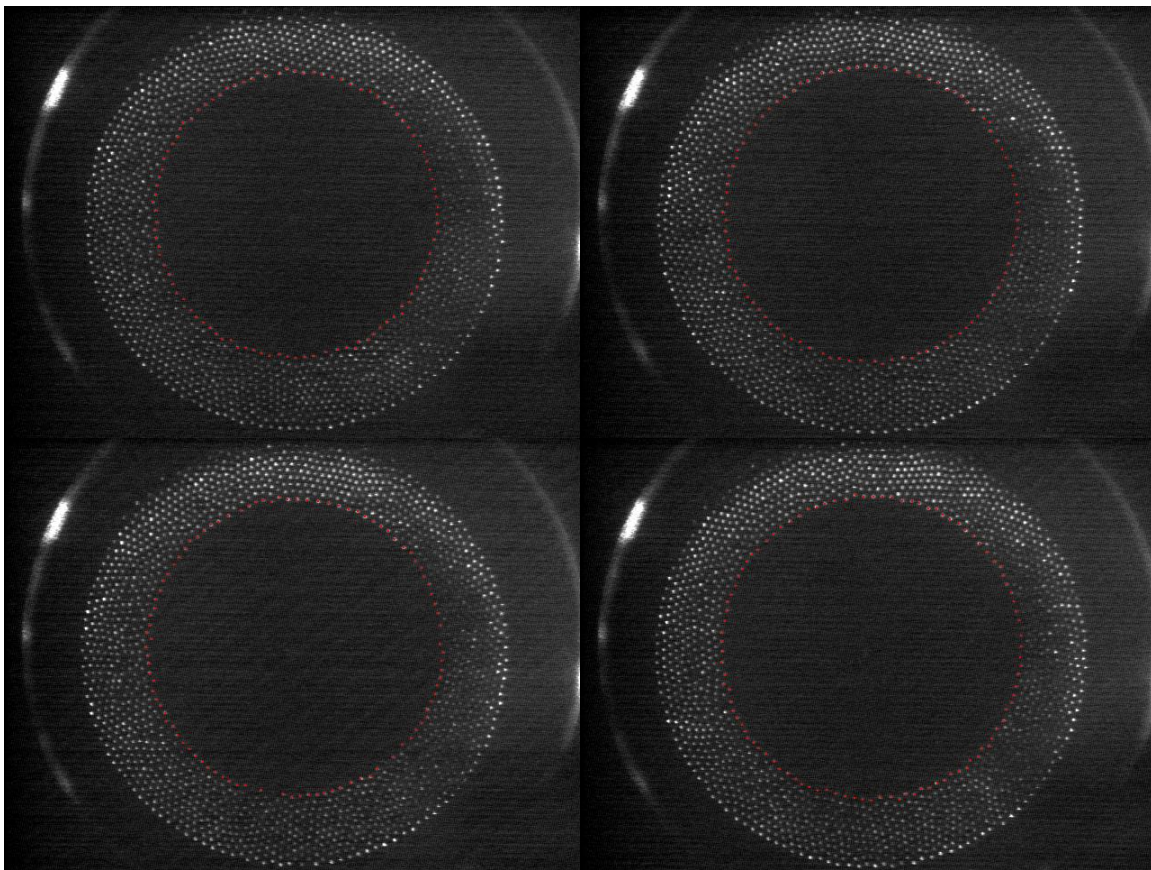


Figure 73 – Intermediate cavity growth using negative probe potentials, from -5 V to -50 V, in increments of -5 V, ordered from left to right.

APPENDIX B

Core Programming Code

Damped Harmonic Oscillator Green's Function (Mathematica Version 8)

Set up recursive algorithm:

```
endOfRec5[t_, charge_, beta_, w2_, yshift_, E0_] :=
  Sum[1.6*10^-19*charge*2*(1/Hz5oneovere[[Floor[y*125]]) -
  1/Hz5oneovere[[1]])*((V0 - Vp)*(1/Hz5oneovere[[Floor[y*125]]) +
  1/Hz5oneovere[[1]])*Hz5particle[[1]] - 1) + E0*Hz5particle[[1]]/
  dustmass*1/125/Sqrt[w2^2 - beta^2]*Sin[Sqrt[w2^2 - beta^2]*(t - y)]
  *Exp[-beta*(t - y)], {y, 2/125, t, 1/125}][[1]] + Hz5particlemin + yshift
```

```
recMethod5[t_, charge_, beta_, w2_, yshift_, E0_] :=
  If[t == 2/125, recResults5[2] = endOfRec5[2/125, charge, beta, w2, yshift, E0],
  recResults5[Floor[t*125]] = Sum[1.6*10^-19*charge*2*
  (1/Hz5oneovere[[Floor[y*125]]) - 1/Hz5oneoveremin)*((V0 -
  Vp)*(1/Hz5oneovere[[Floor[y*125]]) + 1/Hz5oneoveremin)*
  recResults5[Floor[t*125 - 1]] - 1) + E0*recResults5[Floor[t*125 -
  1]]/dustmass*1/125/Sqrt[w2^2 - beta^2]*Sin[Sqrt[w2^2 - beta^2]*(t - y)]*
  Exp[-beta*(t - y)], {y, 2/125, t, 1/125}][[1]] + Hz5particlemin + yshift]
```

Run recursive algorithm:

```
For[m = 2, m < 127, m++, recMethod5[m/125, 8295, 9.66, 65.0, 0.000145, 2750];
  If[Mod[m, 10] == 0, Print[m]]]
```

Plot result:

```
Manipulate[For[m = 2, m < 127, m++, recMethod5[m/125, charge, beta, w2, yshift, E0]];
  Show[{ListLinePlot[Table[{t, recResults5[t*125]}, {t, 2/125, 126/125, 1/125}]],
  ListPlot[Table[{x, Hz5particle[[Floor[x*125]]}], {x, 1/125, 126/125,
  1/125}]], PlotRange -> {{0, 1}, {0.0043, 0.0055}}, {{beta, 6.5}, 6, 40}, {{w2,
  65.5}, 40, 90}, {{charge, 8295}, 1000, 50000}, {{yshift, 0.000145}, -0.0005,
  0.0005}, {{E0, 2750}, 0, 5000} ]
```

Negative Probe-induced Cavity Differential Equation (MATLAB Version 2008b)

Specify differential equation:

```
function phicav = phiode(z,phi,elecfdge,ionfdge,startingni,startingne,E0)
    epsilon0 = 8.85e-12;
    echarge = 1.6e-19;
    % now for 100 mTorr 10 W
    ni0 = startingni;
    ne0 = startingne;
    kTe = 5.429134;
    phicav = [ -phi(2); -echarge/epsilon0*((elecfdge+ne0)*exp(phi(1)/kTe)-...
        (ni0-ionfdge)*E0/abs(phi(2))) ];
end
```

Find ion drag force:

```
ionmass = 6.633520637928e-26;
ub = sqrt(kTe*echarge/ionmass);
ionthermal = sqrt(kTi*echarge/ionmass);
% find speed of ions at inner ring of dust crystal
A_probe = 0.000012219469156;
u = current/echarge/A_probe/ni;
normalu = u/ionthermal;
tau = kTe/kTi;
elecdebye = sqrt(e0*kTe*echarge/ne/echarge^2);
iondebye = sqrt(e0*kTi*echarge/ni/echarge^2);
debye = 1/sqrt(1/elecdebye^2+1/(iondebye^2*(1+normalu^2)));
charge2 = q2*echarge^2/(dustradius*kTe*echarge*4*pi*e0);
betabar = -charge2*tau*dustradius/debye/u^2;
lambda = ((betabar + 1)/(betabar + (dustradius/debye)));
iondragforce = sqrt(2*pi)*dustradius^2*ni*ionmass...
    *ionthermal^2*(sqrt(pi/2)*erf(normalu/sqrt(2))*(1+...
    normalu^2+(1-normalu^(-2))*(1+2*charge2*tau)+4*...
    charge2^2*tau^2*normalu^(-2)*log(lambda))+1/normalu)*...
    (1 + 2*charge2*tau+normalu^2 - 4*charge2^2*tau^2*log(lambda))*...
    exp(-(normalu^2)/2));
```

Find the average dust force on dust at cavity edge (j1 is number of innermost particles):

```
forcedustmat = zeros(j1,numel(debye));
for i=1:j1
    %calculate angle from usual x axis w/probe as origin to ring particle
    %adjust for fickleness of arctangent
    if probedistxa(i) < 0 && probedistya(i) < 0
        anglea(i) = atan(probedistya(i)/probedistxa(i))-pi;
    elseif probedistxa(i) < 0 && probedistya(i) > 0
        anglea(i) = atan(probedistya(i)/probedistxa(i))+pi;
    else
```

```

        anglea(i) = atan(probedistya(i)/probedistxa(i));
    end
    % use formula to calculate force balance from all other dust in ring a
    %set the dust force sum equal to 0
    d1 = zeros(numel(debye),1);
    % forces = zeros(size(dusta,1),1);
    for k=1:size(dusta,1)
        % can't have a force on itself!
        if k == dustarraya(i)
            continue
        end
        dustdistxa = dusta(k,2)-dusta(dustarraya(i),2);
        dustdistya = dusta(k,1)-dusta(dustarraya(i),1);
        dustdista = (dustdistxa^2+dustdistya^2)^(1/2);
        %find angle to dust particle from ring particle
        if dustdistxa < 0 && dustdistya < 0
            dustanglea = atan(dustdistya/dustdistxa)-pi;
        elseif dustdistxa < 0 && dustdistya > 0
            dustanglea = atan(dustdistya/dustdistxa)+pi;
        else
            dustanglea = atan(dustdistya/dustdistxa);
        end
        relativeanglea = dustanglea - anglea(i);
        %calculate d, the sum based on dust positions and debye length
        for m = 1:numel(debye)
            ((1/dustdista+1/debye(m))*exp(-dustdista/debye(m))...
            *cos(relativeanglea))/(dustdista*4*pi*epsilon);
            d1(m) = d1(m) + d;
        end
        for m = 1:numel(debye)
            forcedustmat(i,m) = d1(m)*charge^2;
        end
    end
end
forcedust = mean(forcedustmat(:,1));
totalforce = iondragforce+forcedust;

```

Find the solution of the differential equation:

```

% calculate the electric field initial condition
E0 = totalforce/(q2*echarge);
% predict size of cavity
xspan = [ cavsize 0 ];
initphi = 0;
phi0 = [ initphi, E0 ];
options = odeset('RelTol',1e-3,'AbsTol',[1e-1 1e-1],'InitialStep',1e-4);
[x,phi] = ode45(@phiodecavity,xspan,phi0,options,elecfdge,...
    ionfdge,startingni,startingne,-E0);

```

Eigensolution Model for Waves through Dust Chains (Mathematica Version 8)

```

plot2mode1posfixRMS = Manipulate[ev6 = Eigensystem[( { {tau3*(1/d1 + 1/d0),
- tau3/d1, 0}, {-tau3/d1, tau3*(1/d2 + 1/d1), -tau3/d2},
{0, -tau3/d2, tau3*(1/d3 + 1/d2)} } )];
ev7 = Normalize /@ Transpose[ev6[[2, {1, 2, 3}]]];
test4 = {amp, 0, 0};
test4 = If[Sum[Re[test4[[r]]*ev7[[1, r]]], {r, 3}] < 0, test4 = -test4, test4];
shift = 9.0983;
tmax = 1;
Show[{
  Plot[shift + Sum[Re[test4[[r]]*ev7[[1, r]]*Exp[I*(Sqrt[(ev6[[1, r]])/m]*t +
phase)]]], {r,3}], {t, 1/125, tmax + 1/125}, PlotStyle -> {RGBColor[0, 0,
0]}],
  Plot[shift + d1 + Sum[Re[test4[[r]]*ev7[[2, r]]*Exp[I*(Sqrt[(ev6[[1,
r]])/m]*t + phase)]]], {r,3}], {t, 1/125, tmax + 1/125},PlotStyle ->
{RGBColor[0, 0, 1],Thick}],
  Plot[shift + d1 + d2 + Sum[Re[test4[[r]]*ev7[[3, r]]*Exp[I*
(Sqrt[(ev6[[1,r]])/m]*t + phase)]]], {r,3}], {t, 1/125, tmax + 1/125},
PlotStyle -> {RGBColor[1, 0, 0], Thick}],
  ListPlot[toppart, PlotStyle -> {RGBColor[1, 0, 0]}],
  ListPlot[midpart, PlotStyle -> {RGBColor[0, 0, 1]}],
  ListPlot[botpart, PlotStyle -> {RGBColor[0, 0, 0]}], PlotRange -> {{0,
tmax}, {8.8, shift + d1 + d2 + 1}}, AxesOrigin -> {0, 8.9},
  PlotLabel -> {MatrixForm[ev6[[1, {1, 2, 3}]]], MatrixForm[ev7],
  MatrixForm[{Sqrt[Total[(Table[shift + d1 + d2 +
Sum[Re[test4[[r]]*ev7[[3, r]]*Exp[I*(Sqrt[(ev6[[1, r]])/m]*t +
phase)]]], {r, 3}], {t,1/125, tmax + 1/125, 1/125}] -
Table[toppart[[Floor[t*125], 2]], {t, 1/125, tmax + 1/125,
1/125}]^2]],Sqrt[Total[(Table[shift + d1 + Sum[Re[
test4[[r]]*ev7[[2, r]]*Exp[I*(Sqrt[(ev6[[1, r]])/m]*t + phase)]]], {r,
3}], {t, 1/125, tmax + 1/125, 1/125}] - Table[midpart[
[Floor[t*125], 2]],{t, 1/125, tmax + 1/125, 1/125}]^2]],
Sqrt[Total[(Table[shift + Sum[Re[test4[[r]]*ev7[[1, r]]*
Exp[I*(Sqrt[(ev6[[1, r]])/m]*t + phase)]]], {r, 3}], {t,1/125, tmax +
1/125, 1/125}] - Table[botpart[[Floor[t*125], 2]], {t, 1/125, tmax +
1/125,1/125}]^2]]}],
  {{tau3, 3.008*10^(-10)}, 1.9*10^(-10), 3.2*10^(-10), Appearance -> "Labeled"},
  {{d0, 20}, 0.5, 25, Appearance -> "Labeled"},
  {{d1, 1.341510481089744}, 0.5, 5, Appearance -> "Labeled"},
  {{d2, 1.031728540961537}, 0.5, 5, Appearance -> "Labeled"},
  {{d3, 20}, 0.2, 25, Appearance -> "Labeled"},
  {{m, 5.5182*10^-13}, 0.5*10^-13, 1*10^-12, Appearance -> "Labeled"},
  {{amp, 0.258}, 0.1, 0.6, Appearance -> "Labeled"},
  {{phase, 5.0013}, 0, 2*Pi, Appearance -> "Labeled"}]

```

BIBLIOGRAPHY

- Abramoff, M. D., Magalhães, P. J., and Ram, S. J., *Biophoton. Int.* **11**, 36 (2004).
- Annaratone, B. M., Antonova, T., Goldbeck, D. D., Thomas H. M., and Morfill, G. E., *Plasma Phys. Control. Fusion* **46**, B495 (2004).
- Barnes, M. S., Keller, J. H., Forster, J. C., O'Neill, J. A., and Coultas, D. K., *Phys. Rev. Lett.* **68**, 313 (1992).
- Beckers, J., Ockenga, T., Wolter, M., Stoffels, W. W., van Dijk, J., Kersten, H., and Kroesen, J. M. W., *Phys. Rev. Lett.* **106**, 115002 (2011).
- Benedetti, C., *Dynamical and thermodynamical properties of a 2D Coulomb system and applications to beam physics*, (Universita Di Bologna Dipartimento Di Fisica, 2006) p. 115.
- Bohm, D., Guthrie, A., and Wakerling, R. K., *The Characteristics of Electrical Discharges in Magnetic Fields* (McGraw-Hill, New York, 1949), p. 77.
- Bonitz, M., Horing, N., and Ludwig, P., (Springer, 2010) p. 4.
- Bosinger, T., Labelle, J., Opgenoorth, H. J., Pommereau, J., Shiokawa, K., Solomon, S., and Treumann, R. A., *Dynamic Coupling between Earth's Atmospheric and Plasma Environments* (Springer, New York, 2013).
- Brinkmann, R. P., *J. Appl. Phys.* **102**, 093303 (2007)
- Buttenschön, et al. *New Journal of Physics* **13**, 023042 (2011).
- Chen, F. F., *Introduction to Plasma Physics and Controlled Fusion* (Springer Science+Business Media, LLC, New York, 2006) 2nd Ed., p. 292.
- Creel, J. R., *Characteristic Measurements within a GEC rf Reference Cell*, (Baylor University, 2010).
- Douglass, A., Land, V., Matthews, L., and Hyde, T., *Phys. Plasmas* **18**, 083706 (2011).
- D'yachkov, L. G., Khrapak, A. G., Khrapak, S. A., and Morfill, G. E., *Phys. Plasmas* **14**, 042102 (2007).
- Du, C., Thomas, H. M., Ivlev, A. V., Konopka, U., Morfill, G. E., *Phys. Plasmas* **17** (11), 113710 (2010).

- Engblom, W., and Perrell, E., AIAA 2013-0716.
- Forsyth, C., Fazakerley A. N., Walsh, A. P., and Owen, C. J., A&G **54** (6), 6.45 (2013).
- Fortov, V. E., Khrapak, A. G., Khrapak, S. A., Molotkov, V. I., and Petrov, O. F., Phys. Usp. **47**, 447 (2004).
- Franken, P. A., Hill, A. E., Peters, C. W., and Weinreich, G., Phys. Rev. Lett. **7** (4), 118 (1961).
- Fuechsle, M., Miwa, J. A., Mahapatra, S., Ryu, H., Lee, S., Warschkow, O., Hollenberg, L. C. L., Klimeck, G., and Simmons, M. Y., Nature Nanotechnology **7**, 242 (2012).
- Garcia, J., Elhoussieny, E. E., Bautista, M. A., and Kallman, T. R., The Astrophysical Journal **775** (1), 8 (2013).
- Glanz, J., Science **264**, 5155 (1994).
- Goertz, C. K., Reviews of Geophysics **27** (2), 271 (1989).
- Goree, J., Morfill, G. E., Tsyтович, V. N., and Vladimirov, S. V., Phys. Rev. E **59** (6), 7055 (1999).
- Gurnett, D. A., and Bhattacharjee, A., Introduction to Plasma Physics, (Press Syndicate of the University of Cambridge, Cambridge, 2005).
- Gurnett, D. A., Kurth, W. S., Burlaga, L. F., and Ness, N. F., Science **341** (6153), 1489 (2013).
- Hargis, P. J., Greenberg, K. E., Miller, P. A., Gerardo, J. B., Torczynski, J. R., Riley, M. E., Hebner, G. A., Roberts, J. R., Olthoff, J. K., Whetstone, J. R., Van Brunt, R. J., Sobolewski, M. A., Anderson, H. M., Splichal, M. P., Mock, J. L., Bletzinger, P., Garscadden, A., Gottscho, R. A., Selwyn, G., Dalvie, M., Heidenreich, J. E., Butterbaugh, J. W., Brake, M. L., Passow, M. L., Pender, J., Lujan, A., Elta, M. E., Graves, D. B., Sawin, H. H., Kushner, M. J., Verdeyen, J. T., Horwath, R., and Turner, T. R., Rev. Sci. Instrum. **65** (1), (1994).
- Harris, B. J., Matthews, L. S., and Hyde, T. W., Phys. Rev. E **87** (5), 053109 (2013).
- Hartmann, P., Donko, Z., Kalman, G. J., Kyrkos, S., Golden, K. I., and Rosenberg, M., Phys. Rev. Lett. **103**, 245002 (2009).
- Hedlund, C., J. Vac. Sci. Technol. A **12** (4), 1962 (1994).
- Homann, A., Melzer, A., and Piel, A., Phys. Rev. E **59**, R3835 (1999).

- Hyde, T. W., Kong, J., and Matthews, L. S., Phys. Rev. E **87** (5), 053106 (2013).
- Ikezi, Hiroyuki, Physics of Fluids **29** (1986) 1764.
- Ilgner, M., Astron. Astrophys. **538**, A124 (2012).
- Ivlev, A. V., Sutterlin, R., Steinberg, V., Zuzic, M., and Morfill, G., Phys. Rev. Lett. **85**, 4060 (2000).
- Jones, A. C., and Downes, T. P., Mon. Not. R. Astron. Soc. **420** (1), 817 (2012).
- Jusoh, M. T., Lafond, O., Colombel, F., and Himdi, M., Microwave and Optical Technology Letters **55** (12), 2869 (2013).
- Kretschmer, M., Konopka, U., Zhdanov, S. K., Thomas, H. M., Morfill, G. E., Fortov, V. E., Molotkov, V. I., Lipaev, A. M., and Petrov, O. F., IEEE Trans. Plasma Sci. **39** (11), 2758 (2011).
- Land, V., Matthews, L. S., and Hyde, T. W., Phys. Rev. E **81**, 056402 (2010).
- Land, V., Shen, E., Smith, B., Matthews, L., Hyde, T., New J. Phys. **11**, 063024 (2009).
- Lapenta, G., Physica Scripta **64**, 599 (2001).
- Lieberman, M. A., and Lichtenberg, A. J., Principles of Plasma Discharges and Materials Processing, (John Wiley & Sons, New Jersey, 2005) 2nd Ed. p. 80.
- Lipaev, A. M., Khrapak, S. A., Molotkov, V. I., Morfill, G. E., Fortov, V. E., Ivlev, A. V., Thomas, H. M., Khrapak, A. G., Naumkin, V. N., Ivanov, A. I., Tretschnev, S. E., and Padalka, G. I., Phys. Rev. Lett. **98**, 265006 (2007).
- Liu, J., Chen, L., Mao, A., Guanglan, S., and Duan, P., Vac. **88**, 177 (2013).
- Ma, Q., Matthews, L. S., Land, V., Hyde, T. W., The Astrophysical Journal **763** (2), 77 (2013).
- Marion, J. B., and Thornton, S. T., Classical Dynamics of Particles and Systems, (Harcourt Brace Jovanovich College Publishers, 1988) 2nd Ed. p. 467.
- Melandso, F., Phys. Plasmas **3** (11), 3890 (1996).
- Melzer, A. et al., Phys. Lett. A **191**, 301 (1994).
- Merlino, R. L., and Goree, J., Physics Today, **1** (July 2004).
- Mendis, D. A., and Horányi, M., Review of Geophysics **51** (1), 53 (2013).

- Misawa, T., Ohno, N., Asano, K., Sawai, M., Takamura, S., and Kaw, P. K., *Phys. Rev. Lett.* **86** (7), 1219 (2001).
- Morfill, G. E., and Thomas, H. M., *Icarus* **179**, 539 (2005).
- Osman, K. T., Matthaeus, W. H., Kiyani, K. H., Hnat, B., and Chapman, S. C., *Phys. Rev. Lett.* **111** (20), 201101 (2013).
- Paeva, G. V., *Sheath phenomena in dusty plasmas*, (Technische Universiteit Eindhoven, 2005) p. 61.
- Pieper, J. B., and Goree, J. *Phys. Rev. Lett.* **77** (15), 3137 (1996).
- Piel, A., *Phys. Plasmas* **18**, 073704 (2011).
- Pitts, R. A., *ITER-IAEA: ITER Materials and Technologies*, Monaco, 25 (Nov. 2010).
- Popel, S. I., Golub, A. P., Losseva, T. V., Ivlev, A. V., Khrapak, S. A., and Morfill, G., *Phys. Rev. E* **67**, 056402 (2003).
- Potekhin, A. Y., and Chabrier, G., *Contrib. Plasma Phys.* **53** (4–5), 397 (2013).
- Ramasubramanian, M. K., Barham, O. M., and Swaminathan, V., *Bioinsp. Biomim.* **3**, 046001 (2008).
- Reeves, G. D., Spence, H. E., Henderson, M. G., Morley, S. K., Friedel, R. H. W., Funsten, H. O., Baker, D. N., Kanekal, S. G., Blake, J. B., Fennell, J. F., Claudepierre, S. G., Thorne, R. M., Turner, D. L., Kletzing, C. A., Kurth, W. S., Larsen, B. A., and Niehof, J. T., *Science* **341** (6149), 991 (2013).
- Rynn, N., and D'Angelo, N., *Rev. Sci. Instrum.* **31**, 1326 (1960).
- Sacks, R., and Bohnart, E. *Welding Principles and Practices* (McGraw Hill, New York 2005) 3rd Ed. p. 597.
- Samsonov, D., and Goree, J., *Phys. Rev. E* **59** (1), 1047 (1999).
- Samsonov, D., Ivlev, A. V., and Morfill, G. E., *Phys. Rev. E* **63**, 025401 (2001).
- Samaritan, A. A., and James, B. W., *Phys. Lett. A* **287**, 125 (2001).
- Sbalzarini, I. F., and Koumoutsakos, P., *J. Struct. Biol.* **151**, 182 (2005).
- Selwyn, G. S., *Plasma Sources Sci. Technol.* **3**, 340 (1994).
- Sheridan, T. E., and Goree, J., *Phys. Fluids B* **3**, 2796 (1991).

- Shukla, P. K., and Mamun, A. A., Introduction to Dusty Plasma Physics, (Institute of Physics Publishing, Bristol and Philadelphia, 2002) p. 1, 23.
- Shukla, P. K., and Eliasson, B., Phys.-Usp. **53** (1), 51 (2010).
- Smith Jr., B. A. T., An Experimental Study of Phase Transitions in a Complex Plasma, (Baylor University, 2005).
- Spitzer, L., Jr., Astrophysical Journal **93**, 369 (1941).
- Swinkels, G., Kersten, H., Deutsch, H., and Kroesen, G. M. W., J. Appl. Phys. **88** (4), 1747 (2000).
- Thomas, E., Jr., Avinash, K., and Merlino, R. L., Phys. Plasmas **11** (5), 1770 (2004).
- Thomas, E., Jr., Merlino, R. L., and Rosenberg, M., Plasma Phys. Control. Fusion **54**, 124034 (2012).
- Tomme, E. B., Law, D. A., Annaratone, B. M., and Allen, J. E., Phys. Rev. Lett. **85**, 2518 (2000).
- Trottenberg, T., Melzer, A., and Piel, A., Plasma Sources Sci. Tech. **4**, 450 (1995).
- Vitale, S. A., Wyatt, P. W., and Hodson, C. J., J. Vac. Sci. Tech. **30** (1), 01A130 (2012).
- Wörner, L., Räth, C., Nosenko, V., Zhdanov, S. K., Thomas, H. M., Morfill, G. E., Schablinski, J., and Block, D., EPL, **100** (2012) 35001.
- Xu, W., Song, B., Merlino, R. L., and D'Angelo, N., Rev. Sci. Instrum. **63** (11), 5266 (1992).
- Zartman, I. F., Phys. Rev. **37** (4), 383 (1931).
- Zhang, Z., Qiao, K., Kong, J., Matthews, L., and Hyde, T., Phys. Rev. E **82**, 036401 (2010).
- Zhang, Z., Fundamental Particle and Wave Dynamics in Dusty Plasmas, (Baylor University 2012).